

AD-AU92 566

PHILIPS LABS BRIARCLIFF MANOR NY  
OPTIMIZED PYROELECTRIC VIDICON THERMAL IMAGER. VOLUME II. IMPRO--ETC(U)  
SEP 80 W A SMITH, G LOIACONO, A SHAULOV

F/G 17/5

DAAG53-76-C-0053

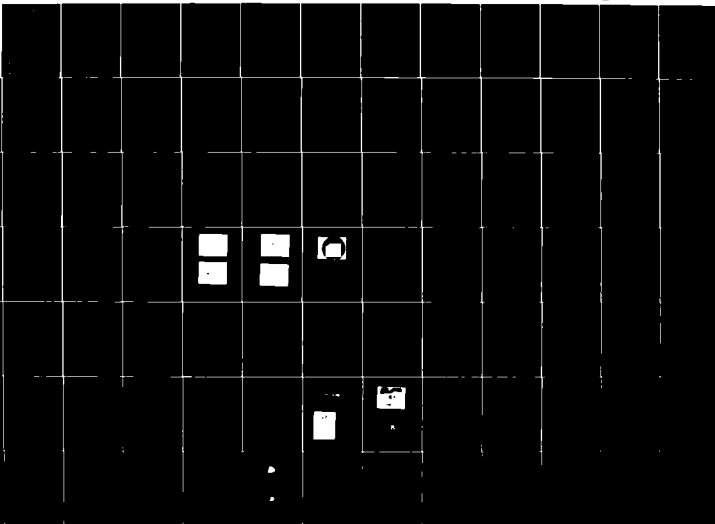
NL

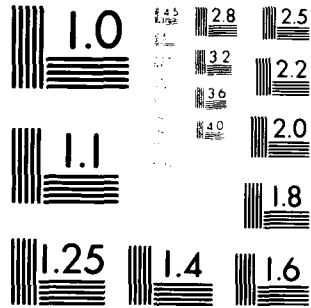
UNCLASSIFIED

1 of 2

AC

20/0000





MICROCOPY RESOLUTION TEST CHART  
 NATIONAL BUREAU OF STANDARDS-1963-A

AD A092566

**LEVEL III**

(12)

SC

A092565

OPTIMIZED PYROELECTRIC VIDICON THERMAL IMAGER

Vol. II: Improper Ferroelectric  
Crystal Growth - Phase II

FINAL TECHNICAL REPORT

August 1978 - November 1979

by

Wallace Arden Smith  
Gabriel Loiacono  
Avner Shaulov

September 1980

DTIC  
ELECTE  
DEC 08 1980  
S D  
E

Prepared for

NIGHT VISION & ELECTRO-OPTICS LABORATORIES  
USAECOM  
Fort Belvoir, Virginia

Contract No. DAAG53-76-C-0053 (Mod. P00007)

\*Original contains color  
plates: All DTIC reproductions  
will be in black and  
white\*

DISTRIBUTION STATEMENT A  
Approved for public release;  
Distribution Unlimited

Prepared by

PHILIPS LABORATORIES  
A Division of North American Philips Corporation  
Briarcliff Manor, New York 10510

DTIC FILE COPY

80 10 31 177

UNCLASSIFIED

SECURITY CLASSIFICATION OF THIS PAGE (When Data Entered)

REPORT DOCUMENTATION PAGE		READ INSTRUCTIONS BEFORE COMPLETING FORM								
1. REPORT NUMBER	2. GOVT ACCESSION NO. <b>AD-A092 566</b>	3. RECIPIENT'S CATALOG NUMBER								
4. TITLE (and Summary) <b>OPTIMIZED PYROELECTRIC VIDICON THERMAL IMAGER.</b>		5. TYPE OF REPORT & PERIOD COVERED <b>Final Technical Report, August 1978—November 1979</b>								
6. AUTHOR(s) <b>Wallace Arden/Smith Gabriel/Loiacono Avner Shaulov</b>		7. PERFORMING ORG. REPORT NUMBER <b>on Phase 2.</b>								
8. PERFORMING ORGANIZATION NAME AND ADDRESS <b>PHILIPS LABORATORIES A Division of North American Philips Corp. Briarcliff Manor, New York 10510</b>		9. CONTRACT OR GRANT NUMBER(s) <b>DAAG53-76-C-0053 (Mod. P00007)</b>								
10. CONTROLLING OFFICE NAME AND ADDRESS <b>Night Vision &amp; Electro-Optics Laboratories USAECOM Ft. Belvoir, Virginia</b>		11. PROGRAM ELEMENT, PROJECT, TASK AREA & WORK UNIT NUMBERS								
12. MONITORING AGENCY NAME & ADDRESS (if different from Controlling Office) <b>(12) 148</b>		12. REPORT DATE <b>September 1980</b>								
		13. NUMBER OF PAGES <b>163</b>								
		14. SECURITY CLASS. (of this report) <b>UNCLASSIFIED</b>								
		15a. DECLASSIFICATION/DOWNGRADING SCHEDULE								
16. DISTRIBUTION STATEMENT (of this Report)										
<div style="border: 1px solid black; padding: 5px; width: fit-content; margin: auto;"> <b>DISTRIBUTION STATEMENT A</b>            Approved for public release;            Distribution Unlimited         </div>										
17. DISTRIBUTION STATEMENT (of the abstract entered in Block 20, if different from Report)										
18. SUPPLEMENTARY NOTES										
19. KEY WORDS (Continue on reverse side if necessary and identify by block number)										
<table style="width: 100%; border: none;"> <tr> <td style="width: 50%;">Boracites</td> <td style="width: 50%;">Crystal growth</td> </tr> <tr> <td>Propionates</td> <td>Improper ferroelectrics</td> </tr> <tr> <td>Pyroelectric</td> <td>Phase transition: ferroelectrics</td> </tr> <tr> <td>Ferroelectric</td> <td></td> </tr> </table>			Boracites	Crystal growth	Propionates	Improper ferroelectrics	Pyroelectric	Phase transition: ferroelectrics	Ferroelectric	
Boracites	Crystal growth									
Propionates	Improper ferroelectrics									
Pyroelectric	Phase transition: ferroelectrics									
Ferroelectric										
20. ABSTRACT (Continue on reverse side if necessary and identify by block number)										
<p>Complete dielectric, pyroelectric, and thermal characterizations of <math>\text{Fe}^{3+}\text{B}^{2+}\text{O}^{2-}\text{I}</math>, <math>\text{Cu}^{2+}\text{B}^{2+}\text{O}^{2-}\text{Cl}</math> and <math>\text{Mn}^{2+}\text{B}^{2+}\text{O}^{2-}\text{I}</math> were performed to confirm the expectation that the boracite family of improper ferroelectrics exhibits high pyroelectric open-circuit voltage response. In each of these materials, the figure of merit, <math>p/r_c</math>, rises as the transition temperature is approached; the peak value attained at the transition varies only slightly in a temperature interval of several degrees below the transition. The peak figures-of-merit of</p> <p style="text-align: right;">Continued</p>										

Volume 6

10

15

20. Abstract (Continued)

$6,000 \text{ sq. cm/C}$   $5,300 \text{ sq cm/C}$   
 these materials are larger than that of TGS and close to that of DTGFB (FeI:  $6 \times 10^3 \text{ cm}^2/\text{C}$ ; CuCl:  $6 \times 10^3 \text{ cm}^2/\text{C}$ ; MnI:  $5.3 \times 10^3 \text{ cm}^2/\text{C}$ ). A vapor-transport growth technique was developed which can produce boracite single crystals of sufficient size for device applications.

$5,000 \text{ sq cm/C}$   $5,700 \text{ sq cm/C}$   
 Complete dielectric, pyroelectric, and thermal characterizations of dicalcium lead propionate (DLP)  $\text{Ca}_2\text{Pb}(\text{C}_2\text{H}_5\text{COO})_6$  and dicalcium strontium propionate (DSP)  $\text{Ca}_2\text{Sr}(\text{C}_2\text{H}_5\text{COO})_6$  were performed to confirm the expectation that the propionate family of pseudo-proper ferroelectrics exhibits a high, broad maximum in their figures of merit. The measured figures-of-merit are larger than that of TGS and close to that of DTGFB (DLP:  $5 \times 10^3 \text{ cm}^2/\text{C}$ ; DSP:  $5.7 \times 10^3 \text{ cm}^2/\text{C}$ ). A solution growth technique was developed which has produced single crystals of size and quality already adequate for device applications. Experimentation on adjusting the properties of the propionates by molecular-engineering techniques exhibited the rich potential in this family of pyroelectrics for designing materials to meet specific device requirements.

Accession For	
NTIS GRA&I	<input checked="" type="checkbox"/>
IDC TAB	<input type="checkbox"/>
Unannounced	<input type="checkbox"/>
Justification	<i>Per Letter on File</i>
By _____	
Distribution/	
Availability Codes	
Dist.	Avail and/or special
<b>A</b>	

1473 B

## SUMMARY

Complete dielectric, pyroelectric, and thermal characterizations of  $\text{Fe}_3\text{B}_7\text{O}_{13}\text{I}$ ,  $\text{Cu}_3\text{B}_7\text{O}_{13}\text{Cl}$  and  $\text{Mn}_3\text{B}_7\text{O}_{13}\text{I}$  were performed to confirm the expectation that the boracite family of improper ferroelectrics exhibits high pyroelectric open-circuit voltage response. In each of these materials, the figure of merit,  $p/\epsilon c$ , rises as the transition temperature is approached; the peak value attained at the transition varies only slightly in a temperature interval of several degrees below the transition. The peak figures-of-merit of these materials are larger than that of TGS and close to that of DTGFB (FeI:  $6 \times 10^3 \text{ cm}^2/\text{C}$ ; CuCl:  $6 \times 10^3 \text{ cm}^2/\text{C}$ ; MnI:  $5.3 \times 10^3 \text{ cm}^2/\text{C}$ ). A vapor-transport growth technique was developed which can produce boracite single crystals of sufficient size for device applications.

Complete dielectric, pyroelectric, and thermal characterizations of dicalcium lead propionate (DLP)  $\text{Ca}_2\text{Pb}(\text{C}_2\text{H}_5\text{COO})_6$  and dicalcium strontium propionate (DSP)  $\text{Ca}_2\text{Sr}(\text{C}_2\text{H}_5\text{COO})_6$  were performed to confirm the expectation that the propionate family of pseudo-proper ferroelectrics exhibits a high, broad maximum in their figures of merit. The measured figures-of-merit are larger than that of TGS and close to that of DTGFB (DLP:  $5 \times 10^3 \text{ cm}^2/\text{C}$ ; DSP:  $5.7 \times 10^3 \text{ cm}^2/\text{C}$ ). A solution growth technique was developed which has produced single crystals of size and quality already adequate for device applications. Experimentation on adjusting the properties of the propionates by molecular-engineering techniques exhibited the rich potential in this family of pyroelectrics for designing materials to meet specific device requirements.

## PREFACE

A program to develop an optimized pyroelectric vidicon thermal imager was issued by the U. S. Army Mobility Equipment Research and Development Center, Fort Belvoir, Virginia, and was initiated under Contract No. DAAG53-76-C-0053. Dr. Lynn Garn was the Contracting Officer's Representative for the Night Vision Laboratory, USAECOM. Modification No. P00007 to the contract added the requirement for improper-ferroelectric materials research.

This work was performed by Philips Laboratories, a Division of North American Philips Corporation, Briarcliff Manor, New York. The materials research task was under the overall supervision of Dr. Ramesh Bhargava, Director, Exploratory Research Group. Dr. Wallace Arden Smith, Theoretical Physicist, was the Program Leader. Mr. Gabriel M. Loiacono, Senior Program Leader for Crystal Growth and Materials Technology, was responsible for crystal growth. Dr. Avner Shaulov, Physicist, was responsible for measurements. Mr. John Jacco, Mr. John Zola, Mr. Larry Perillo, Mr. George Kostecky and Mr. Anthony Pink were involved in the materials crystal growth and preparation efforts. Mr. John Hannes, Mr. Donald Dorman, and Ms. Madeleine Rosar participated in the materials evaluation effort. Dr. Edward Stupp, Senior Program Leader for Solid State Components, was available in a consulting and advisory capacity on device implications.

The work described in this Final Technical Report covers the period from August 1978 to November 1979.

## TABLE OF CONTENTS

<u>Section</u>	<u>Page</u>
SUMMARY.....	3
PREFACE.....	5
LIST OF ILLUSTRATIONS.....	9
LIST OF TABLES.....	12
1. INTRODUCTION, SUMMARY, AND CONCLUSIONS.....	15
1.1 Introduction.....	15
1.2 Summary of Results.....	19
1.3 Conclusions.....	22
1.4 Collaborative Efforts.....	23
2. BORACITE MEASUREMENTS.....	24
2.1 FeI Boracite Measurements.....	24
2.1.1 Poling.....	25
2.1.2 Dielectric and Pyroelectric Measurements.....	25
2.1.3 Figure of Merit.....	27
2.2 CuCl Boracite Measurements.....	27
2.2.1 Specific Heat.....	29
2.2.2 Data on Samples for Electrical Measurements.....	29
2.2.3 Birefringence.....	30
2.2.4 DC Resistivity.....	31
2.2.5 Pyroelectric Coefficient and Ratio p/c..	31
2.2.6 Permittivity and Dissipation Factor.....	33
2.2.7 Figure of Merit.....	36
2.3 MnI Boracite Measurement.....	38
2.3.1 Specific Heat.....	38
2.3.2 Data on Samples for Electrical Measurements.....	38
2.3.3 Birefringence.....	39
2.3.4 DC Resistivity.....	39
2.3.5 Dielectric Constant.....	41
2.3.6 Pyroelectric Coefficient and Ratio p/c..	42
2.3.7 Figure of Merit.....	42
2.4 NiBr Boracite Measurements.....	44
2.4.1 Specific Heat.....	45
2.4.2 Birefringence.....	45
2.4.3 Dielectric Constant.....	46
2.4.4 DC Resistivity.....	47
2.4.5 Poling and Pyroelectric Behavior.....	55
3. PROPIONATE MEASUREMENTS.....	57
3.1 Dicalcium Lead Propionate Measurements: As- Grown and Annealed Samples.....	57
3.1.1 Sample Preparation.....	58

TABLE OF CONTENTS (Cont'd)

<u>Section</u>	<u>Page</u>
3.1.2 Pyroelectric Coefficient.....	58
3.1.3 Dielectric Constant.....	59
3.1.4 Dynamic Measurement of p/c.....	61
3.1.5 Dynamic Measurement of Figure-of-Merit p/εc.....	61
3.1.6 Dielectric Constant from Dynamic Measurements.....	63
3.1.7 Discussion.....	64
3.2 Dielectric, Pyroelectric and Thermal Measure- ments in As-Grown and Annealed Samples of DSP [Ca <sub>2</sub> Sr(C <sub>2</sub> H <sub>5</sub> COO) <sub>6</sub> ].....	65
3.2.1 Dicalcium Strontium Propionate: Specific Heat.....	65
3.2.2 Sample Preparation for Electrical Measurements.....	66
3.2.3 Dielectric Constant.....	66
3.2.4 Spontaneous Polarization and Pyroelec- tric Coefficient, Annealed DSP.....	70
3.2.5 Dynamic Measurements of p/c and p/εc on Annealed DSP.....	72
4. BORACITE CRYSTAL GROWTH.....	75
4.1 Hydrothermal Synthesis of Boracite Powders.....	75
4.2 Hydrothermal Growth of Boracite Crystals.....	77
4.2.1 Apparatus.....	77
4.2.2 Growth from Acidic Media.....	78
4.2.3 Hydrothermal Growth in Basic Media.....	99
4.3 Vapor Transport Growth of Boracite Crystals.....	101
4.3.1 Apparatus.....	101
4.3.2 Transport Reactions.....	103
4.3.3 Experimental.....	103
4.3.4 Results.....	104
5. PROPIONATE CRYSTAL GROWTH.....	120
5.1 Dicalcium Lead Propionate and Dicalcium Strontium Propionate.....	120
5.2 DLP-DSP Mixed Crystals.....	123
5.3 Molecular Engineering of Propionates.....	124
6. REFERENCES.....	128
 <u>Appendices</u>	
A Dielectric Anomalies in Boracites.....	131
B Propionate X-Ray Structures.....	153
C Chemcial Nomenclature.....	159
DISTRIBUTION LIST.....	163

LIST OF ILLUSTRATIONS

	<u>Page</u>
Fig. 1: Temperature dependence of dielectric constant of FeI boracite, measured in a field of 7 V/cm at 8 kHz.....	26
Fig. 2: Pyroelectric coefficient of FeI boracite as measured by Byer-Roundy technique at heating rate of 7.6°C/min.....	26
Fig. 3: Temperature dependence of the ratio p/c in FeI boracite, as measured by dynamic method.....	28
Fig. 4: Figure of merit p/εc of FeI boracite from p/c and ε measurements compared with the directly measured figures of merit of TGS and DTGFB.....	28
Fig. 5: Specific heat of CuCl boracite.....	29
Fig. 6: Birefringence perpendicular to the spontaneous polarization in $\text{Cu}_3\text{B}_7\text{O}_{13}\text{Cl}$ .....	30
Fig. 7: Log resistivity vs. reciprocal temperature for two crystals of CuCl boracite.....	32
Fig. 8: Pyroelectric coefficient vs. temperature in $\text{Cu}_3\text{B}_7\text{O}_{13}\text{Cl}$ . Circles are values obtained in sample SH2 by Byer and Roundy technique. Crosses and triangles are data obtained from dynamic measurement of p/c in samples SH2 and SH3 respectively, combined with our recent results for c.....	32
Fig. 9: Ratio p/c for sample SH2 (crosses) and sample SH3 (triangles) of $\text{Cu}_3\text{B}_7\text{O}_{13}\text{Cl}$ .....	34
Fig. 10: Temperature dependence of the pyroelectric coefficient in CuCl boracite, FeI boracite, terbium molybdate (TMO) and unannealed di-calcium lead propionate (DLP).....	34
Fig. 11: Dielectric constant vs. temperature in $\text{Cu}_3\text{B}_7\text{O}_{13}\text{Cl}$ boracite as measured at 100 kHz.....	35
Fig. 12: Dissipation factor in $\text{Cu}_3\text{B}_7\text{O}_{13}\text{Cl}$ at 100 kHz....	35
Fig. 13: Dielectric constant vs. temperature in $\text{Cu}_3\text{B}_7\text{O}_{13}\text{Cl}$ as measured at 10 kHz in two different methods.....	37
Fig. 14: Figure of merit for sample SH2 (crosses) and sample SH3 (triangles) of $\text{Cu}_3\text{B}_7\text{O}_{13}\text{Cl}$ .....	37

LIST OF ILLUSTRATIONS (Cont'd)

	<u>Page</u>
Fig. 15: Specific heat of MnI boracite.....	39
Fig. 16: Birefringence perpendicular to the spontaneous polarization in $Mn_3B_7O_{13}I$ .....	40
Fig. 17: Log resistivity vs. reciprocal temperature in $Mn_3B_7O_{13}I$ .....	40
Fig. 18: Dielectric constant at 10 kHz as a function of temperature in $Mn_3B_7O_{13}I$ .....	41
Fig. 19: Pyroelectric coefficient vs. temperature in $Mn_3B_7O_{13}I$ .....	43
Fig. 20: Ratio p/c vs. temperature in $Mn_3B_7O_{13}I$ .....	43
Fig. 21: Temperature dependence of the figure of merit in $Mn_3B_7O_{13}I$ .....	44
Fig. 22: Specific heat of NiBr boracite.....	45
Fig. 23: Spontaneous birefringence vs. temperature of $Ni_3B_7O_{13}Br$ .....	46
Fig. 24: Dielectric constant at 8 kHz vs. temperature in $Ni_3B_7O_{13}Br$ .....	47
Fig. 25: Domains structure in $Ni_3B_7O_{13}Br$ sample #SHN1 in various stages of a poling process.....	49
Fig. 26: Log resistivity vs. reciprocal temperature in $Ni_3B_7O_{13}Br$ .....	55
Fig. 27: Temperature dependence of pyroelectric coefficient of annealed (closed circles) and as-grown (open circles) DLP.....	58
Fig. 28: Temperature dependence of dielectric constant of annealed (closed circles) and as-grown (open circles) DLP.....	60
Fig. 29: Fit of dielectric constant of annealed DLP to a modified Curie-Weiss law.....	60
Fig. 30: Temperature dependence p/c in as-grown DLP (open circles) and annealed DLP biased externally by a field of 5 kV/cm (closed circles).....	62

LIST OF ILLUSTRATIONS (Cont'd)

	<u>Page</u>
Fig. 31: Dynamic response measurement of the figure of merit $p/\epsilon c$ , in as-grown DLP (open circles) and annealed DLP biased externally by a field of 5 kV/cm (closed circles).....	62
Fig. 32: Dielectric constant as determined from dynamic response measurements in as-grown DLP (open circles) and annealed DLP biased externally by a field of 5 kV/cm (closed circles).....	63
Fig. 33: Temperature dependence of the ratio $p/\epsilon$ in annealed (circles) and as-grown (crosses) DLP....	64
Fig. 34: Temperature dependence of specific heat of DSP between 230 K and 325 K.....	65
Fig. 35: Temperature dependence of dielectric constant of as-grown DSP.....	67
Fig. 36: Dielectric constant vs. temperature for DSP annealed at 340°C for 64 hours.....	67
Fig. 37: Modified Curie-Weiss law in annealed DSP.....	69
Fig. 38: Temperature dependence of dielectric constant of annealed DSP at 340°C for 64 hours under various biasing fields.....	69
Fig. 39: Spontaneous polarization of DSP annealed at 340°C for 64 hours measured by charge integration (crosses). The solid curve is the theoretical form.....	71
Fig. 40: Pyroelectric coefficient of DSP annealed at 340°C for 64 hours obtained by differentiation of charge integration measurements of the spontaneous polarization.....	71
Fig. 41: Temperature dependence of ratio $p/c$ in annealed DSP as measured by dynamic technique.....	72
Fig. 42: Temperature dependence of the figure of merit, $p/\epsilon c$ , in annealed DSP as measured by dynamic technique.....	74
Fig. 43: Calculated temperature dependence of $p/\epsilon c$ for DSP under biasing fields of 0, 2 and 5 kV/cm...	74

LIST OF ILLUSTRATIONS (Cont'd)

	<u>Page</u>
Fig. 44: Hydrothermal boracite growth.....	83
Fig. 45: Typical NiBr boracite crystals grown hydro- thermally.....	85
Fig. 46: Typical decomposition of NiBr boracite crystals during solubility experiments.....	97
Fig. 47: Temperature gradient in three zone furnace.....	102
Fig. 48: Typical temperature vs. time program for three zone vapor transport furnace.....	102
Fig. 49: Oscillation-method for gradient formation.....	102
Fig. 50: NiBr boracite crystals grown using a three-zone vapor transport technique.....	107
Fig. 51: Other boracite crystals grown by vapor trans- port.....	109
Fig. 52: $Ni_3B_7O_{13}Br$ crystals attached to wall of quartz chamber.....	115
Fig. 53: Multiple nucleation of $Ni_3B_7O_{13}Br$ on film.....	115
Fig. 54: Nucleation sites for boracite on platinum foil.....	117
Fig. 55: Typical cluster of boracite nucleated on platinum foil.....	117
Fig. 56: Propionate crystals during growth.....	121
Fig. 57: DLP crystals after removal from solution.....	123
Fig. 58: Molecular structure of acids.....	125

LIST OF TABLES

	<u>Page</u>
Table 1: Spontaneous Polarization of DSP.....	70
Table 2: P-T Data on NiBr System (72 hour experiments)....	80
Table 3: Effect of Reaction Temperature on Solution (pH)..	87
Table 4: Joubert-Type Experiments.....	88
Table 5: Alternate Synthesis.....	93
Table 6: Direct Dissolution.....	94
Table 7: Solubility of NiBr Boracite in H <sub>2</sub> O.....	99
Table 8: Solubility of Boracite in H <sub>2</sub> O-H <sub>3</sub> BO <sub>3</sub> .....	99
Table 9: Crystal Growth for Ni <sub>3</sub> B <sub>7</sub> O <sub>13</sub> Br.....	105
Table 10: Crystal Growth for Mn <sub>3</sub> B <sub>7</sub> O <sub>13</sub> I.....	106
Table 11: Analysis of Vapor Transport Phases in Growth of Ni <sub>3</sub> B <sub>7</sub> O <sub>13</sub> Br.....	113
Table 12: Propionate Growth Runs.....	122
Table 13: Summary of Molecular Engineering.....	127

## 1. INTRODUCTION, SUMMARY, AND CONCLUSIONS

### 1.1 Introduction

This study reports the second phase (Phase II) of improper ferroelectric materials research under Contract No. DAAG53-76-C-0053. The goal of the entire effort is to identify and produce materials which would enhance the performance of the pyroelectric vidicon (PEV).

#### 1.1.1 Phase I: Motivation, Results and Conclusions

The first phase of this study\* of improper ferroelectrics focused on identification of materials which would enhance the performance of the pyroelectric vidicon. The pyroelectric materials commonly used in this device are in the TGS-DTGF family and are all proper ferroelectrics. The principle limitation with proper ferroelectrics is that the increase in the pyroelectric coefficient obtained by operating closer in temperature to the ferroelectric-paraelectric phase transition is more than overcome by a concomitant increase in the dielectric constant. Thus, the material's figure of merit,  $p/\epsilon c$ , where  $p$  = pyroelectric coefficient,  $\epsilon$  = dielectric constant, and  $c$  = volume specific heat, decreases as the ferroelectric Curie temperature is approached. In the case of improper ferroelectrics, there is no dielectric divergence upon approaching the ferroelectric-paraelectric phase transition, and therefore one obtains a figure of merit that increases dramatically up to the Curie point.

In the initial phase, the investigations at Philips Laboratories, in conjunction with Yeshiva University, began with a comprehensive literature survey and selection of representative materials from a number of known classes of improper ferroelectrics (molybdates, sulfates, propionates and boracites). Samples of

---

\* Philips Laboratories, "Optimized Pyroelectric Vidicon Thermal Imager, Vol. II: Improper Ferroelectric Materials", Final Report: Sept. 1976-Feb. 1978, W.A. Smith, NVEL/USAECOM, Contract No. DAAG53-76-C-0053, Briarcliff Manor, NY, July 1978.

each material were obtained or grown, and a comprehensive set of thermal and electrical measurements was performed.

The results of the Phase I study were:

- \* Confirmation that improper ferroelectrics have the expected potential for greatly improved pyroelectric figure of merit.
- Identification of the boracite and propionate materials as the families of improper ferroelectrics with greatest potential.

#### 1.1.2 Phase II: Plans and Implementation

The second phase of this study\* of improper ferroelectrics focused on the growth and characterization of boracite and propionate materials.

##### (1) Boracites

The program on boracites was three pronged: crystal growth, experimental characterization, and theoretical modeling. The first of these tasks was seen to be particularly demanding in light of the difficulties experienced by earlier workers in the synthesis and growth of boracite crystals. Major effort was focused on this task. A wide ranging survey of materials synthesis and crystal growth techniques was undertaken: direct melt, flux, epitaxial, hydrothermal, vapor transport, gel, etc. Attention focused on two approaches: hydrothermal and vapor transport. Two new crystal growth facilities were established at Philips Laboratories to pursue these two growth avenues simultaneously. As described below, these efforts led to development of novel synthesis and growth methods and culminated in the production of large single crystals of NiBr boracite.

Development of techniques to characterize boracite crystals was pursued in parallel to the crystal growth effort by obtaining crystals from outside sources: Dupont, Plessey, and University

---

\* Philips Laboratories, "Continuation (Phase II) of the Improper Ferroelectric Portion of Contract No. DAAG53-76-C-0053", Tech. Proposal PL-20278 for MERADCOM, Feb. 1978.

of Geneva. The measurements also presented major difficulties due to limitations in size and quality of crystals initially available. Techniques had to be developed to orient, fabricate, and electrode samples. Poling of the samples was known from the onset to be a particularly demanding task, both from the experience of other researchers and from our own preliminary work. A new experimental facility was established at Philips Laboratories, and a new technique was developed to characterize the dielectric and pyroelectric properties of boracites while maintaining the samples under continuous optical control. An additional challenge, not initially envisioned, was presented by the low electrical resistivity of the samples initially available. Again, special experimental techniques were developed to overcome this problem and obtain reliable experimental characterization of boracites. In addition to these special techniques, the full range of standard techniques (charge integration, camlibel pulse, Byer-Roundy dc heating, hysteresis loops, dynamic response, etc.) available at Philips Laboratories was employed to characterize the boracites. As described below, these effects culminated in the complete dielectric, pyroelectric and thermal characterization of three boracites: FeI, CuCl and MnI, and dielectric and thermal characterization of NiBr boracite.

In theoretical modeling, the major task was to decide what form of the thermodynamic potential was appropriate to describe the ferroelectric phase transition. Two models have been proposed: the Dovrak-Petzelt, Gufan-Sakhnenko improper ferroelectric model and the Levanyuk-Sannikov triggered ferroelectric model. Since both models are in reasonable agreement with the available macroscopic data, it was initially planned to address the question with a Raman scattering study of the microscopic behavior in the vicinity of the phase transition. A major adjustment in this plan was necessitated by the discontinuation of the graduate research program at Yeshiva University in the interval between the submission of the proposal and initiation of the program. With the relocation of Professor Michael I.

Bell to the National Bureau of Standards, it was no longer possible to undertake the measurement of Raman spectra and its analysis as part of this program.

The absence of the microscopic information thus thrust the burden of theoretical modeling onto a precision least-squares analysis of the macroscopic data. That effort continues at PL, and it is not yet clear whether the appropriate thermodynamic potential can be determined from the macroscopic data alone.

(2)        Propionates

The program on propionates had two major thrusts: crystal growth and measurement. It was already clear at the end of the first phase that the propionates were well characterized theoretically as having a second-order, pseudo-proper phase transition.

The crystal growth research was directed at three tasks: first, develop a solution-growth technique and grow pure dicalcium lead propionate and pure dicalcium strontium propionate; second, grow mixed crystals of dicalcium lead-strontium propionate; third, grow materials containing other organic acid radicals partially substituting for the propionic acid radicals. Philips Laboratories has a high level of expertise in solution-growth techniques and these tasks were undertaken and accomplished in sequence, as noted in the following section.

The principal measurement task with the propionates, beyond developing the appropriate fabrication and electroding techniques, was to understand and eliminate the internal bias fields present in as-grown samples of these materials. As mentioned in the following section, a thermal annealing procedure was found to eliminate the internal bias field. As expected, the measurements were found to be well modeled as second-order, pseudo-proper ferroelectrics.

## 1.2 Summary of Results

### 1.2.1 Boracite Measurements

Complete pyroelectric, dielectric and thermal characterization was obtained for FeI, CuCl and MnI boracites. Dielectric and thermal characterization of NiBr boracite was also completed; pyroelectric measurements are still in progress. A new experimental technique was developed to control the poling state of the crystals by continuous observation of the optical birefringence during measurement. Novel techniques were employed to extract the pyroelectric coefficient from measurements on samples with large and highly temperature-dependent conductivities and with large thermally stimulated currents of nonpyroelectric origin. These measurements were made principally on small crystals obtained from outside sources while our own growth efforts were developing; measurements on our own crystals will continue as an in-house effort.

In each case the boracites: (i) exhibited the expected increase in the figure-of-merit as the transition temperature was approached, (ii) showed only a small variation in the figure-of-merit in an interval of several degrees near the maximum, (iii) yielded a maximum value for the figure of merit greater than that of TGS and about equal to that of DTGFB (FeI:  $6 \times 10^3 \text{ cm}^2/\text{C}$ ; CuCl:  $6 \times 10^3 \text{ cm}^2/\text{C}$ ; MnI:  $5.3 \times 10^3 \text{ cm}^2/\text{C}$ ).

The theoretical analysis of the macroscopic measurements is still in progress. The absence of conclusive microscopic evidence has compelled us to address this area with a detailed precision analysis of the macroscopic data. We are currently investigating whether such an analysis can distinguish between the thermodynamic potential from the Dvorak-Pelzelt and Gufan-Sakhnenko improper ferroelectric model and the thermodynamic potential from the Levanyuk-Sannikov triggered ferroelectric model. While the proper theoretical model on which to base extrapolation from our measurements is not as yet certain,

preliminary results based on the Dvorak-Petzelt potential indicate that figures of merit many times that of DTGFB are obtainable within the family of boracite materials.

### 1.2.2 Propionate Measurements

The pyroelectric, dielectric and thermal behavior was measured for samples of dicalcium lead propionate (DLP) and dicalcium strontium propionate (DSP) grown at Philips Laboratories. These measurements are in good agreement with the theoretical predictions based on a second-order, pseudo-proper thermodynamic potential. Each material reveals the expected broad maximum for the figure of merit near 52°C (DLP) and 0°C (DSP). The maximum values attained (DLP:  $5 \times 10^3 \text{ cm}^2/\text{C}$ ; DSP:  $5.7 \times 10^3 \text{ cm}^2/\text{C}$ ) are just less than that of DTGFB and would be expected to increase once proper thermal annealing conditions are determined.

A thermal annealing process was developed to remove the internal bias field observed in the as-grown samples. The maximum value of the figure of merit is little affected by the presence or absence of a bias field. Any bias field - internal or external - causes a broadening of the temperature range over which the maximum remains large. Moreover, the presence of a bias field causes a reduction in the dielectric constant near the transition temperature without altering the figure of merit.

On the basis of these measurements, mixed crystals of DLP and DSP could be expected to exhibit a broad maximum at any temperature between 0°C and 50°C; this gives one the freedom to adjust the operating temperature of a device based on the propionate family of materials.

The observation that the dielectric constant can be adjusted by a bias field without affecting the figure of merit also reveals the substantial malleability to device considerations available within the propionate family.

### 1.2.3 Boracite Crystal Growth

A novel technique for the synthesis of boracite powders was developed. This low-temperature, low-pressure hydrothermal synthesis gives the highest yield of boracite material among all known methods.

Extensive experimentation on the hydrothermal growth of boracite single crystals was carried out. Studies included synthesis-growth and dissolution-transport in both acid and basic media. Variations in temperature, pressure, reactants, reactant loading sequence, reactant concentration, and mineralizer concentration were examined to determine the optimum conditions for growth of single crystals. A number of experimental conditions were identified which produce high quality crystals, about 0.5 mm on an edge in high yield.

A novel three-zone vapor transport technique was developed for the growth of boracite. Large single crystals (> 10 mm on edge) of NiBr boracite were produced. Methods were developed to control nucleation and eliminate cracking of crystals during growth. Experimentation was begun on the growth of MnI boracite and mixed crystals of NiBrCl and FeMnI boracite using this technique.

### 1.2.4 Propionate Crystal Growth

A technique was developed for the solution growth of large single crystal of dicalcium lead propionate (DLP)  $\text{Ca}_2\text{Pb}(\text{C}_2\text{H}_5\text{COO})_6$  and dicalcium strontium propionate (DSP)  $\text{Ca}_2\text{Sr}(\text{C}_2\text{H}_5\text{COO})_6$ .

Efforts to grow mixed DLP-DSP crystals by the same technique were impeded by a lack of information on the temperature dependence of the phase diagram for the mixed system.

Exploration of the molecular engineering possibilities in the propionate family was begun by the growth of materials with other organic acid radicals substituted for the propionic acid radical. Several new material were obtained; acrylic acid doped DLP formed the best quality crystals.

Direct confirmation of our working hypothesis that the ferroelectric properties of the propionates can be tuned by partial substitution of other organic acid radicals for the propionic acid radicals was provided by X-ray studies of propionates performed at Oxford University.

### 1.3 Conclusions

The conclusions of this study are:

- The boracite family of ferroelectrics contains members with very high figures-of-merit.

This leads to renewed confidence that boracite compositions can be identified which have even higher figures of merit along with the other known advantages of these materials: low piezoelectric coefficient (low piezoelectric noise), adjustable bulk conductivity (possible PEV conduction pedestal), adjustable transition temperature (adjustable device operating temperature), and chemical-mechanical robustness (ease and versatility in use).

- Large single crystals of boracites can be grown by a vapor transport technique.

This demonstrates a viable method for producing boracite crystals of sufficient size for practical device applications.

- The propionate family of ferroelectrics contains members with very high figures-of-merit, and the properties of these materials can be tailored by molecular engineering techniques.

In addition to the high figures-of-merit available in propionates, there is great potential in this family of pyroelectrics in terms of designing materials to meet device requirements.

- Single crystals of propionates can be grown by a solution growth technique.

The solution growth of large, high-quality propionate crystals yields materials already adequate for device use.

#### 1.4 Collaborative Efforts

An open and fruitful exchange of information on boracite growth and characterization has existed between this program and a parallel effort at the Plessey Company funded by the British Ministry of Defense and monitored by the Royal Signals & Radar Establishment. It is good to acknowledge the cooperation of Frank W. Ainger (Plessey), Roger W. Whatmore (Plessey), Crofton Brierley (Plessey), Gordon Jones (RSRE), and R. Watton (RSRE).

As a consultant to this program, Prof. Hans Schmid, University of Geneva, has been generous in sharing the fruits of his fifteen years experience in growth and characterization of boracites.

Prof. Philip Gentile, Fordham University, had guided the thesis research of Dr. Michael Delfino on the hydrothermal synthesis and characterization of boracites. Prof. Gentile had given freely of his time and experience as a consultant to this program.

Dr. A. M. Glazer, Oxford University, has performed structural studies on the phase transition in the propionates wholly independent of our effort. We are indebted to Dr. Glazer both for communicating his results to us prior to publication and for stimulating discussions of their implications.

In any open scientific exchange it is difficult to identify the originator of an idea. Where possible we have identified in the text the explicit contributions of our collaborators - their implicit contributions permeate the remainder.

## 2. BORACITE MEASUREMENTS

Complete dielectric, pyroelectric and thermal characterizations have been performed on three boracites: FeI, CuCl, and MnI (Par. 2.1, 2.2 and 2.3, respectively). These measurements permit the evaluation of the figure of merit,  $p/\epsilon c$ , for each of these materials.

While detailed behaviors vary among these three, in each case the temperature dependence of the figure of merit shows the expected rise as the transition temperature is approached. The large maximum value for the figure of merit varies only slightly in a temperature interval of several degrees near the peak. In each case the maximum figure of merit is greater than that of TGS and close to that of DTGFB (FeI:  $6 \times 10^3 \text{ cm}^2/\text{C}$ ; CuCl:  $6 \times 10^3 \text{ cm}^2/\text{C}$ ; MnI:  $5.3 \times 10^3 \text{ cm}^2/\text{C}$ ).

Dielectric and thermal characterization of NiBr boracite have also been completed (Par. 2.4). As yet, a reliable measurement of the pyroelectric behavior of this materials is not in hand, so no evaluation of its figure of merit is attempted.

Appendix A contains a unified discussion of the temperature dependence of the dielectric constant of all four materials as well as some insights which can be gained from a theoretical analysis of these data alone.

### 2.1 FeI Boracite Measurements

Efforts were made to pole and measure the dielectric and pyroelectric properties of FeI boracite crystals obtained from Dupont and the Plessey Company. One sample of FeI boracite from Dupont gave evidence of being poled to a high degree (Par. 2.1.1). Measurements of the dielectric permittivity and pyroelectric coefficient are reported (Par. 2.1.2). These measurements permit an evaluation of the figure of merit for FeI boracite. The temperature dependence of the figure of merit reveals the expected rise as the transition temperature ( $72^\circ\text{C}$ )

is approached. The maximum value of this figure of merit about  $6 \times 10^3 \text{ cm}^2/\text{C}$  exceeds the figure of merit for TGS and is about equal to that of DTGFB. Moreover, this large value for the figure of merit changes only slightly in a temperature interval of several degrees near the peak (Par. 2.1.3).

#### 2.1.1 Poling

FeI boracite was studied before the development of the apparatus to control the poling state of the crystal by continuous observation of the optical birefringence during electrical measurements. Reliance was placed on analysis of the electric measurements themselves to assess the poling state of the FeI crystals.

The samples of FeI boracite obtained from Dupont and Plessey were poled by cooling the sample through the phase transition while applying a dc electric field as large as 10 kV/cm. Subsequently, dielectric and pyroelectric measurements were performed, both to measure these properties and to assess the state of poling.

Poling of some samples in the opposite direction resulted in pyroelectric current whose magnitude differed from the initial measurement. This indicated a partial poling of these samples.

A single sample of FeI boracite obtained from Dupont was found to reverse its polarization readily under the application of a dc field of 10 kV/cm. Such behavior is indicative of a properly poled sample, however, it does not preclude the possibility that a multidomain structure exists which cannot be removed by application of an electric field as large as 10 kV/cm

#### 2.1.2 Dielectric and Pyroelectric Measurements

Using the FeI boracite sample, whose poling was described above, measurements were made of the dielectric constant  $\epsilon$  at 8 kHz (see Fig. 1), the pyroelectric coefficient  $p$ , using the Byer-Roundy dc heating technique (see Fig. 2), and the ratio  $p/c$  of

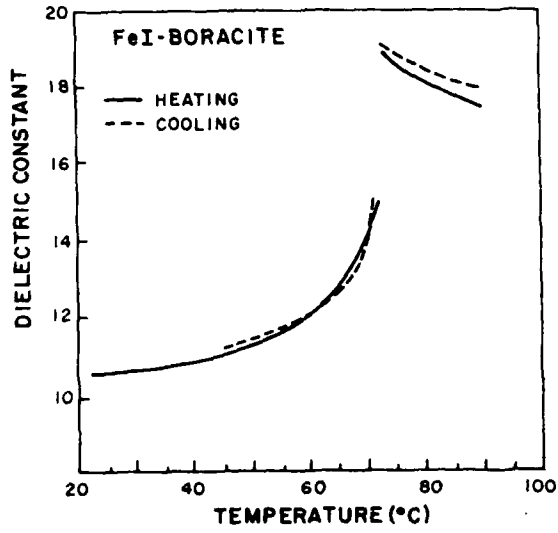


Figure 1. Temperature dependence of dielectric constant of FeI boracite, measured in a field of 7 V/cm at 8 kHz.

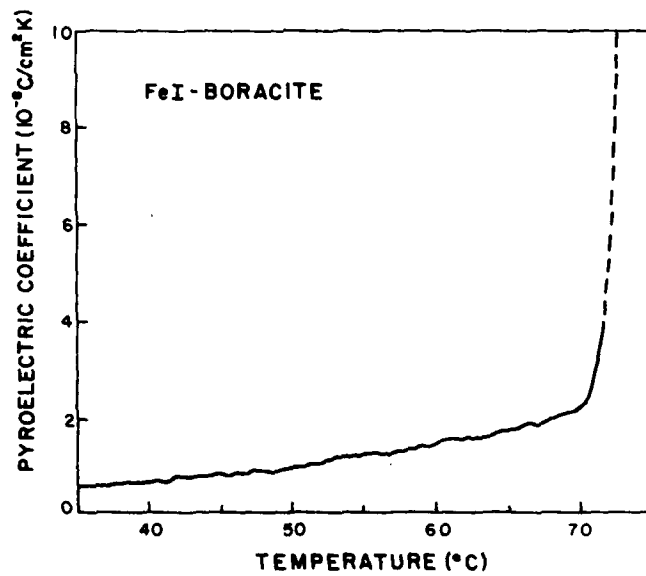


Figure 2. Pyroelectric coefficient of FeI boracite as measured by Byer-Roundy technique at heating rate of 7.6°C/min.

the pyroelectric coefficient to the specific heat using a Chynoweth dynamic response technique (see Fig. 3).

The small size of the sample (area  $0.016 \text{ cm}^2$ , thickness  $150 \text{ }\mu\text{m}$ , resulting in a capacitance of only  $1 \text{ pF}$ ) precluded the direct measurement of the figure of merit  $p/\epsilon c$ .

The temperature dependence of the dielectric constant is in excellent agreement with the measurements of Schmid et al. (Ref. 1). Combining the Byer-Roundy measurement of the pyroelectric coefficient (Fig. 2) with our previously reported measurements of the specific heat (Ref. 2) gives a value for  $p/c$  which agrees well with the value measured by the dynamic response method (Fig. 3).

### 2.1.3 Figure of Merit

Using the measured values of  $p/c$  and  $\epsilon$ , we have evaluated the figure of merit  $p/\epsilon c$  for FeI boracite. This result is shown in Figure 4, along with our measurements of the figure of merit of TGS and DTGFB. The temperature dependence of the figure of merit shows the rise expected for improper ferroelectrics. The peak value of the figure of merit is larger than that of TGS and about equal to that of DTGFB. Moreover, this large value for the figure of merit changes only slightly in a temperature interval of several degrees near the peak.

### 2.2 CuCl Boracite Measurements

The temperature dependence of the dielectric constant, pyroelectric coefficient, and specific heat of CuCl boracite supplied by H. Schmid was measured. These samples exhibited a large and highly temperature dependent conductivity, and large background currents which are not pyroelectric in origin. Nevertheless it was possible to determine the pyroelectric coefficient and verify that it is larger in CuCl boracite than in any other known improper ferroelectric. The dielectric constant of these

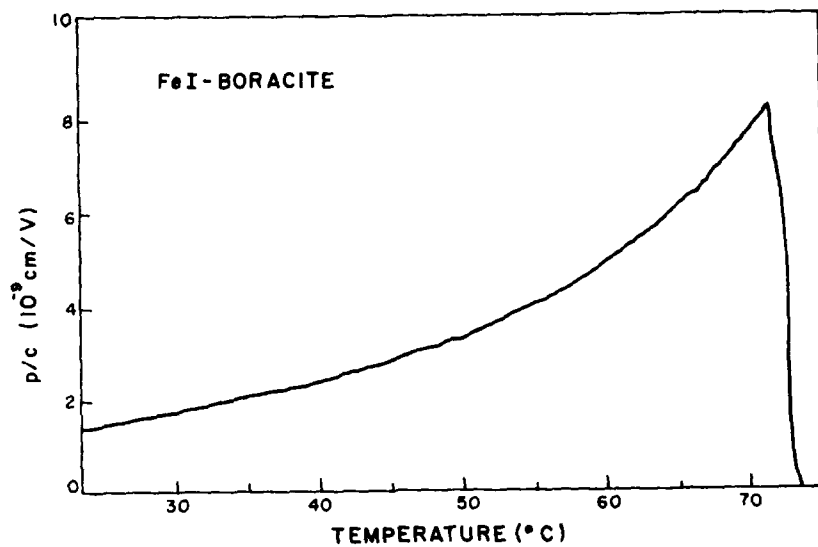


Figure 3. Temperature dependence of the ratio  $p/c$  in FeI boracite, as measured by dynamic method.

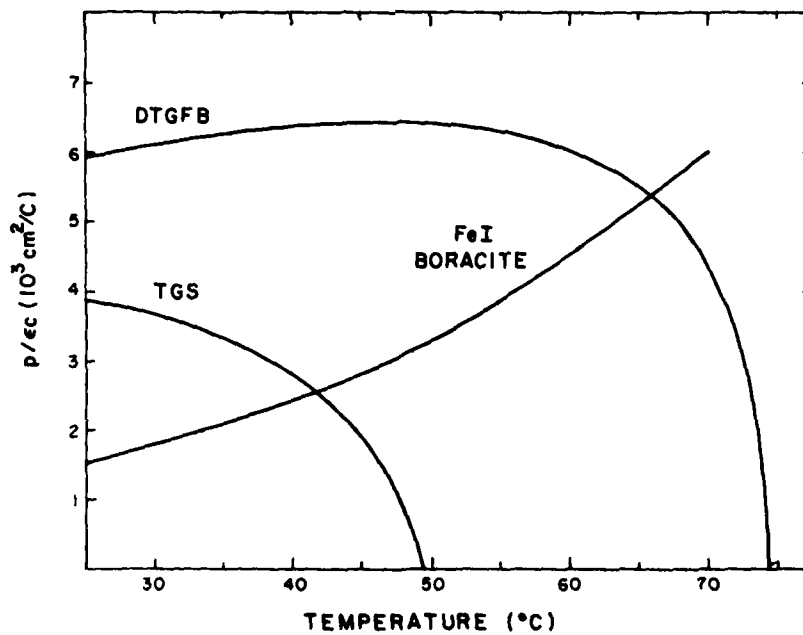


Figure 4. Figure of merit  $p/\epsilon c$  of FeI boracite from  $p/c$  and  $c$  measurements compared with the directly measured figures of merit of TGS and DTGFB.

samples is also quite large and the figure of merit,  $p/\epsilon c$ , reaches a peak at  $T_c$  of about  $6 \times 10^3 \text{ cm}^2/\text{C}$ . This value is greater than the figure of merit of TGS and about equal to the figure of merit of DTGFB.

### 2.2.1 Specific Heat

The 32.88 mg sample of CuCl boracite measured was that received from H. Schmid, University of Geneva. The results of measurements from 250°K to 450°K are shown in Figure 5. These data show the characteristic multiple peaks near the phase transition associated with inhomogeneous strains in the crystal (Ref 3). The transition temperature and magnitude of the specific heat are in reasonable agreement with measurements performed by H. Schmid (private communication), although our values are somewhat lower.

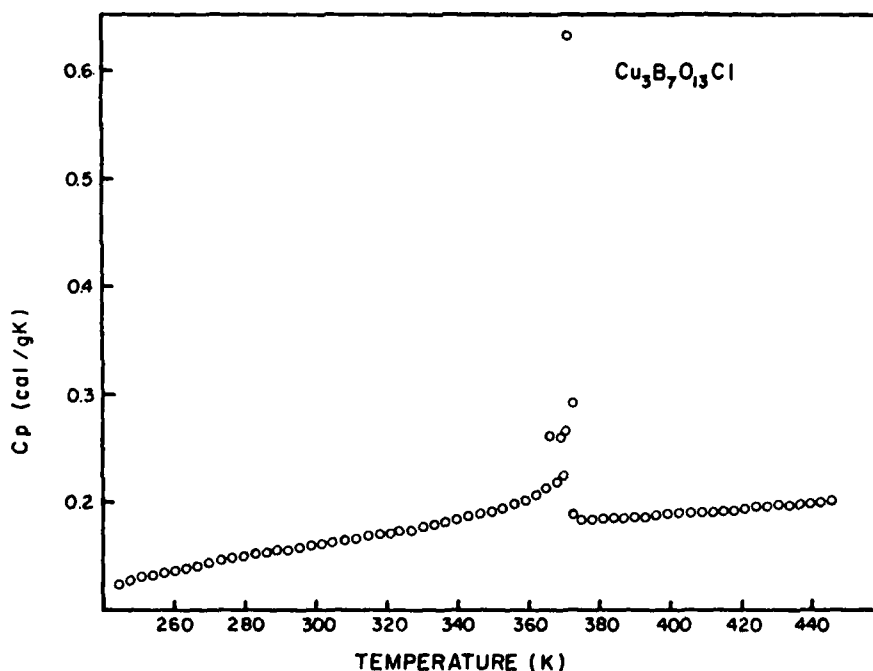


Figure 5. Specific heat of CuCl boracite.

### 2.2.2 Data on Samples for Electrical Measurements

Electrical measurements were performed on two samples of  $\text{Cu}_3\text{B}_7\text{O}_{13}\text{Cl}$  supplied by H. Schmid from Geneva University. The samples were

(100)<sub>cub</sub> cut wafers electroded on both faces with evaporated gold on chromium. Sample #SH2 (thickness 63.5  $\mu\text{m}$ ) was provided with a guarded circular electrode of area 0.014  $\text{cm}^2$ . A rectangular electrode of area 0.04  $\text{cm}^2$  was evaporated on sample #SH3 (thickness 60.5  $\mu\text{m}$ ). The electrodes on both samples were transparent so that the domain structure of the samples was visible between crossed polarizers. The samples were mounted in a heating stage of a Leitz polarizing microscope to permit visual control of the domain state of the samples throughout the entire temperature range of the measurement. Before each measurement the samples were poled with a steady field up to 20 kV/cm applied during slow cooling through the Curie point and down to room temperature. After poling both samples remained poled on heating up to the Curie point in absence of a bias field.

### 2.2.3 Birefringence

The magnitude of the spontaneous birefringence  $\Delta n_s$  was used to check the orientation of the spontaneous polarization within the sample during the measurements. Birefringence was measured with white light by means of a tilting compensator (Leitz 1350 M). Results of birefringence versus temperature measurements are presented in Figure 6. These results agree within  $\sim 10\%$  of the data of Schmid and Tippman (Ref. 4) for  $\Delta n_s$  perpendicular to  $P_s$  in  $\text{Cu}_3\text{B}_7\text{O}_{13}\text{Cl}$ .

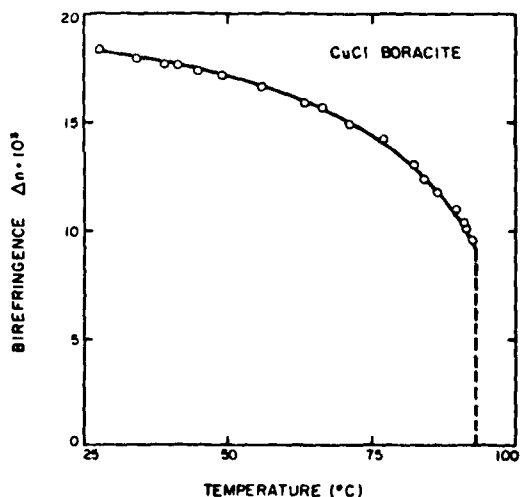


Figure 6. Birefringence perpendicular to the spontaneous polarization in  $\text{Cu}_3\text{B}_7\text{O}_{13}\text{Cl}$ .

As was pointed out by Schmid and Tippman (Ref. 4), the temperature dependence of  $\Delta n_s$  in  $\text{Cu}_3\text{B}_7\text{O}_{13}\text{Cl}$  is relatively strong among boracites. On the basis of this observation, a strong temperature dependence of  $P_s$  and hence a high pyroelectric coefficient was expected for  $\text{Cu}_3\text{B}_7\text{O}_{13}\text{Cl}$ .

#### 2.2.4 DC Resistivity

The temperature dependence of the bulk dc resistivity  $\rho$  was measured in sample #SH2 at 10 V using a guard ring method. In Figure 7 the logarithm of  $\rho$  is plotted versus the reciprocal temperature. It is seen that the dc resistivity is relatively low (about 3 orders of magnitude less than  $\rho$  in FeI-boracite) and decreases exponentially as the temperature is increased. Activation energies of 0.64 eV and 0.50 eV were obtained below and above  $T_c$  respectively. DC resistivity measurements on sample #SH3 yielded similar results with slightly higher values of  $\rho$  (see Fig. 7). The activation energies obtained in this sample were 0.68 eV below  $T_c$  and 0.47 eV above  $T_c$ .

#### 2.2.5 Pyroelectric Coefficient and Ratio p/c

In measurements of the pyroelectric coefficient,  $p$ , using the Byer and Roundy technique, difficulties were encountered with large nonpyroelectric background currents (currents which did not reverse sign on cooling). These currents are probably due to the thermal release of trapped charge carriers which are injected into the sample during the poling process. A great part of the background currents could be eliminated by heating the sample to about 85°C and cooling it down to room temperature while its electrodes were shorted. After repeating this process several times, appreciable background currents were still generally observed above ~ 70°C. In determining the pyroelectric coefficient from the measured currents the contribution of the residual background currents was eliminated by subtracting the current obtained on cooling from the current obtained on heating. The values of the pyroelectric coefficient obtained are presented in Figure 8 by circles.

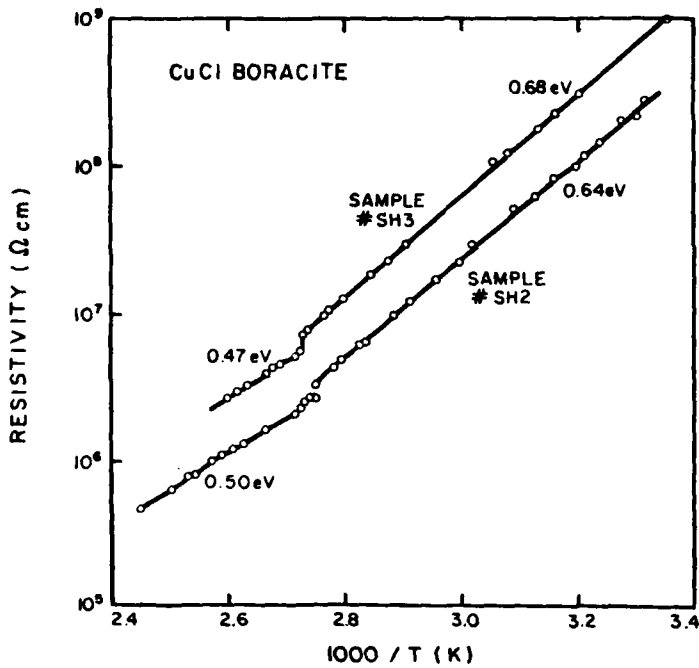


Figure 7. Log resistivity vs. reciprocal temperature for two crystals of CuCl boracite.

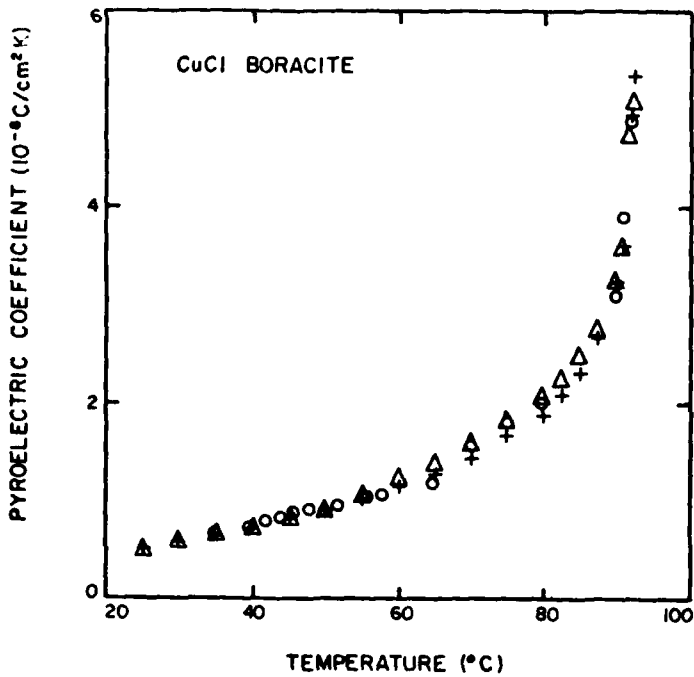


Figure 8. Pyroelectric coefficient vs. temperature in  $\text{Cu}_3\text{B}_7\text{O}_{13}\text{Cl}$ . Circles are values obtained in sample SH2 by Byer and Roundy technique. Crosses and triangles are data obtained from dynamic measurement of p/c in samples SH2 and SH3 respectively, combined with our recent results for c.

Dynamic measurement of the ratio  $p/c$  were performed by chopping the microscope light at 30 Hz. The ac voltage developed across a load resistor of 100 k- $\Omega$  was measured with a lock-in amplifier (Ortholoc - SC 9505). The results obtained in the two samples are presented in Figure 9. The calibration of these measurements was obtained by setting  $p = 9.0 \times 10^{-9}$  C/cm<sup>2</sup>K, and  $c = 2.83$  J/cm<sup>3</sup> at 50°C. This calibration is based on the specific heat data obtained in our lab for another sample of CuCl boracite supplied by Schmid (Par. 2.2.1), and several Byer and Roundy measurements of  $p$  on the samples used in these dynamic measurements (Fig. 8). The value of  $p$  at 50°C was further confirmed by measuring the pyroelectric current response to a step light signal. The temperature change was determined by measuring the change in the resistance of the sample, and the charge released was obtained by integrating the pyroelectric current.

The dynamic measurements of  $p/c$  combined with our data for  $c$  yielded, for the pyroelectric coefficient, the results shown in Figure 8. These results agree well with the data obtained from the Byer and Roundy measurements.

It should be noted that the values of the pyroelectric coefficient in  $\text{Cu}_3\text{B}_7\text{O}_{13}\text{Cl}$  are the highest observed among all improper ferroelectrics that we have studied so far. In Figure 10 the pyroelectric coefficient of  $\text{Cu}_3\text{B}_7\text{O}_{13}\text{Cl}$  is compared with that of TMO, DLP and  $\text{Fe}_3\text{B}_7\text{O}_{13}\text{I}$ .

#### 2.2.6 Permittivity and Dissipation Factor

Measurements of permittivity,  $\epsilon$ , and dissipation factor as a function of temperature were made in a field of 2.5 V/cm at 100 kHz, using a Hewlett-Packard 4274A LCR meter. The results are shown in Figures 11 and 12. Upon heating, the permittivity increased from a value of 11.5 at room temperature to a peak value of 23 at  $T_c$ . In the transition from the ferroelectric phase to paraelectric phase,  $\epsilon$  jumped abruptly downward to a value of 14.5 and remained constant up to 130°C. As was already

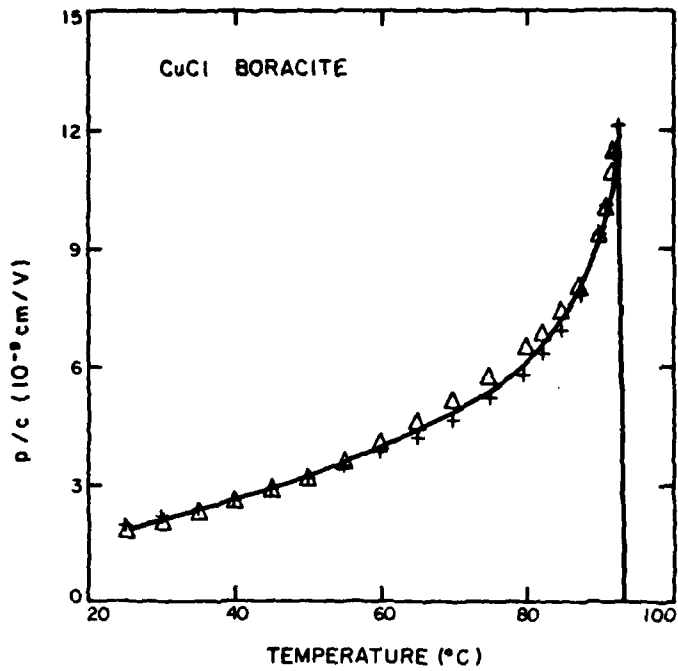


Figure 9. Ratio p/c for sample SH2 (crosses) and sample SH3 (triangles) of  $\text{Cu}_3\text{B}_7\text{O}_{13}\text{Cl}$ .

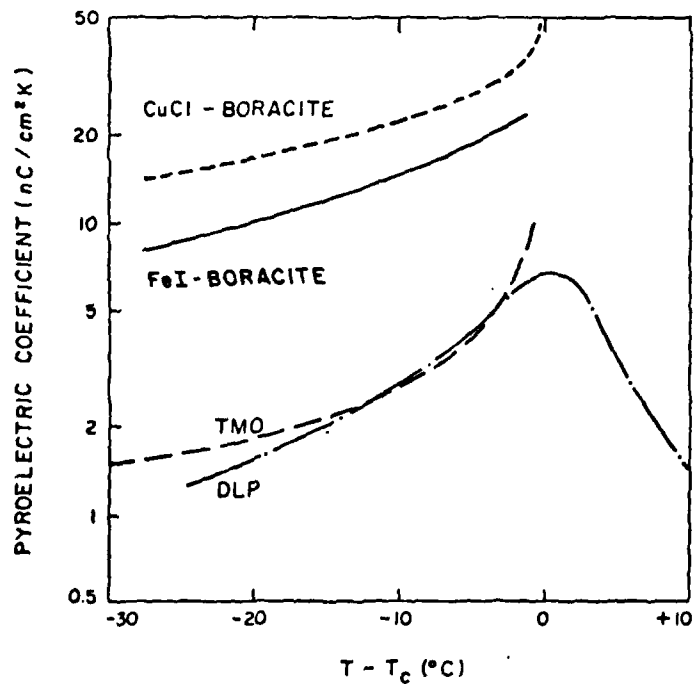


Figure 10. Temperature dependence of the pyroelectric coefficient in CuCl boracite, FeI boracite, terbium molybdate (TMO) and unannealed dicalcium lead propionate (DLP).

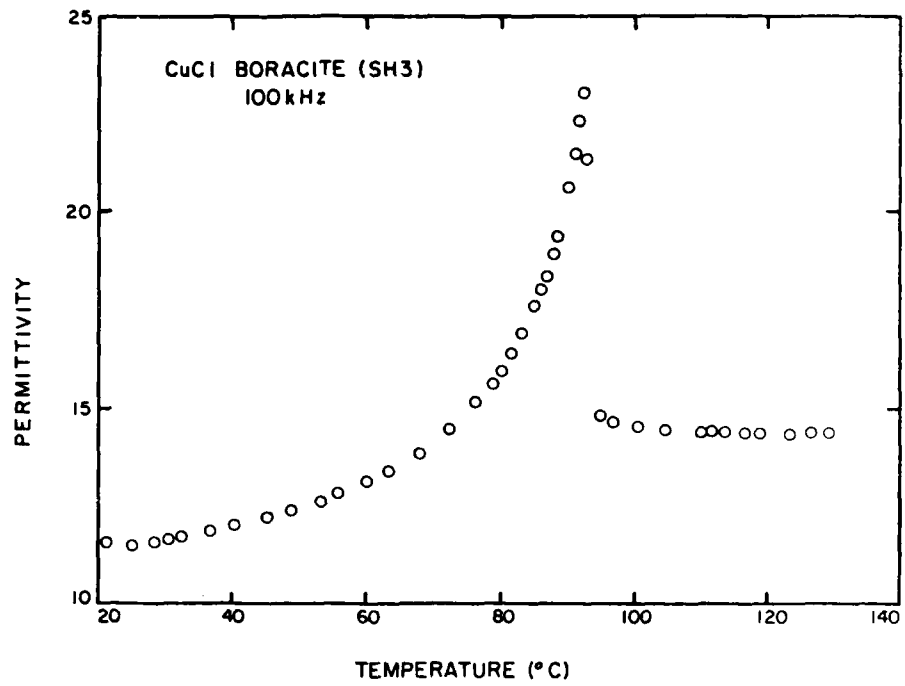


Figure 11. Dielectric constant vs. temperature in  $\text{Cu}_3\text{B}_7\text{O}_{13}\text{Cl}$  boracite as measured at 100 kHz.

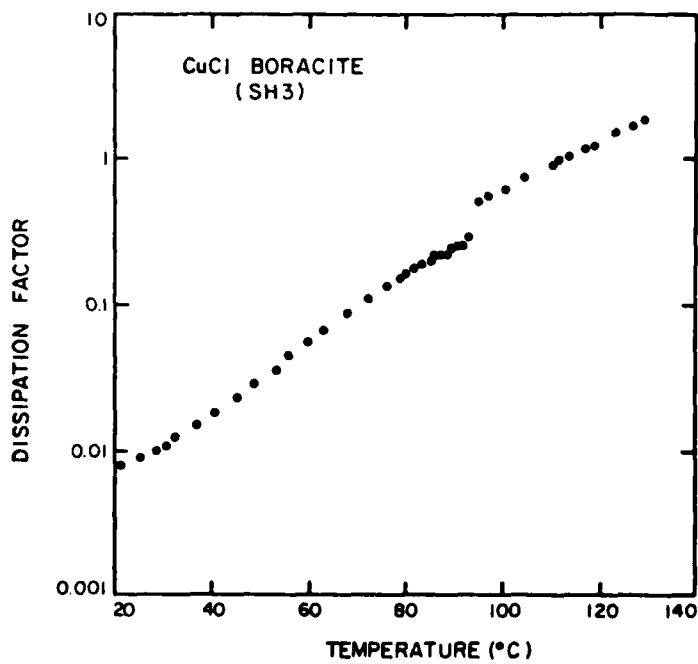


Figure 12. Dissipation factor in  $\text{Cu}_3\text{B}_7\text{O}_{13}\text{Cl}$  at 100 kHz.

pointed out (Ref. 5), the behavior of the permittivity in  $\text{Cu}_3\text{B}_7\text{O}_{13}\text{Cl}$  is unusual. In most other boracites (including  $\text{Cu}_3\text{B}_7\text{O}_{13}\text{Br}$ )  $\epsilon$  exhibited a discontinuous jump upward at  $T_c$  upon heating.

Measurements of  $\epsilon$  were also performed at 10 kHz by determining the ratio of the capacitance of the sample to that of a reference capacitor placed in series with it. An ac signal of 100 mV was applied to the sample and reference (10 nF) and a Lock-in Amplifier (Ortholoc - SC 9505) was used to measure the in-phase voltage appearing across the reference capacitor. The results (Fig. 13) showed a slightly higher peak of  $\epsilon$  at  $T_c$  and a temperature dependence of  $\epsilon$  above  $T_c$ . These differences are probably artifacts connected with the high dielectric loss of the material at elevated temperatures. Measurement of  $\epsilon$  at 10 kHz using the HP meter yielded similar results (circles in Fig. 13).

#### 2.2.7 Figure of Merit

The high values of the pyroelectric coefficient are compensated by relatively high values of the permittivity so that the figure of merit,  $M = p/\epsilon c$ , is not as high as expected. Figure 14 shows the temperature dependence of  $M$  as obtained from the dynamic measurement of  $p/c$  and the data of  $\epsilon$  at 100 kHz. The figure of merit rises from value of  $\sim 2 \times 10^3 \text{ cm}^2/\text{C}$  at room temperature to a maximum value of  $\sim 6 \times 10^3 \text{ cm}^2/\text{C}$  at  $T_c$ , this is about equal to the figure of merit of DTGFB.

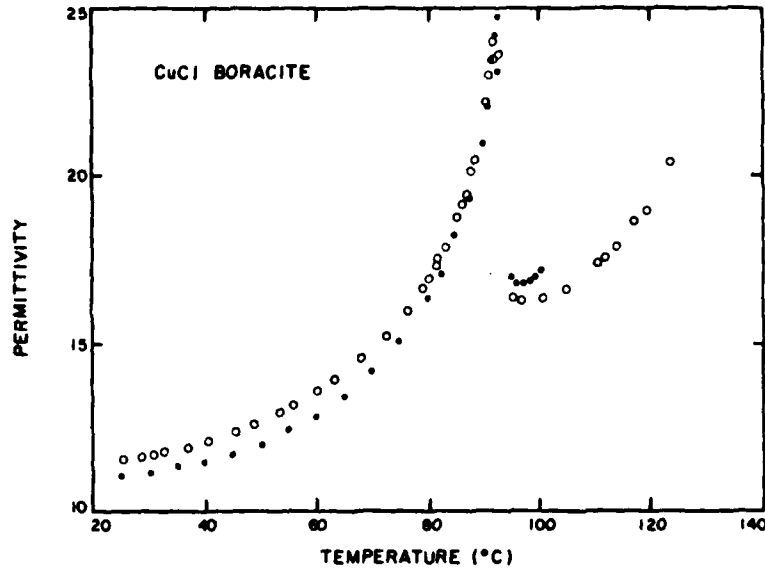


Figure 13. Dielectric constant vs. temperature in  $\text{Cu}_3\text{B}_7\text{O}_{13}\text{Cl}$  as measured at 10 kHz in two different methods.

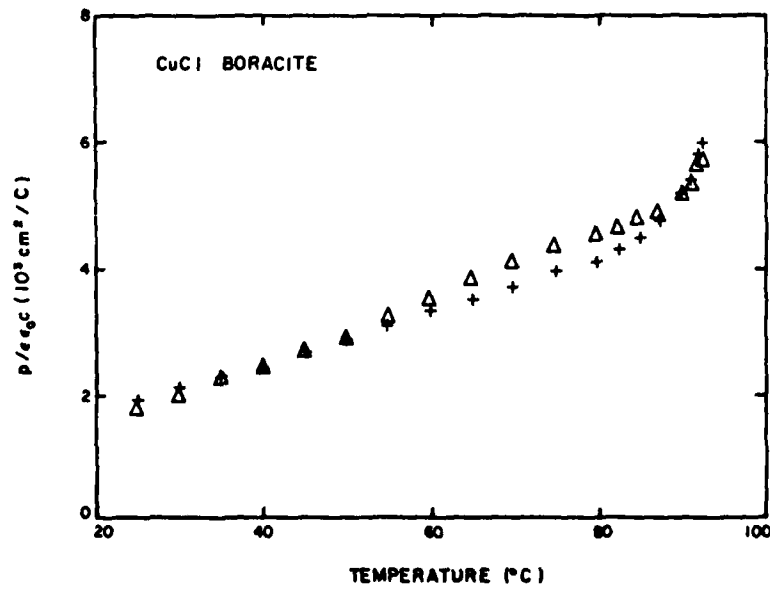


Figure 14. Figure of merit for sample SH2 (crosses) and sample SH3 (triangles) of  $\text{Cu}_3\text{B}_7\text{O}_{13}\text{Cl}$ .

### 2.3 MnI Boracite Measurements

The temperature dependence of the dielectric constant and pyroelectric coefficient was measured on a sample of MnI boracite supplied by H. Schmid; the temperature dependence of the specific heat was measured on samples grown at Philips Laboratories. While the birefringence of MnI boracite shows little temperature dependence, the spontaneous polarization does vary substantially with temperature giving rise to an appreciable pyroelectric coefficients. The figure of merit,  $p/\epsilon c$ , of MnI boracite rises to a peak value at the transition temperature of about  $5.3 \times 10^3 \text{ cm}^2/\text{C}$ . This value is somewhat less than the maximum figure of merit for DTGFB.

#### 2.3.1 Specific Heat

While electrical measurements on MnI boracite were performed on a sample received from H. Schmid, University of Geneva, the specific heat measurements, however, were performed on a 14.64 mg sample grown at Philips Laboratories. The sample came from growth run LP 04; the lattice constant was measured to be  $12.31 \pm 0.06 \text{ \AA}$ . The results in Figure 15 show a single peak which begins at about  $390^\circ\text{K}$  with a specific heat of approximately  $0.165 \text{ cal/gK}$ , and rises to a maximum at  $413.6^\circ\text{K}$ . The specific heat then drops back down to continue its nearly linear rise with temperature.

#### 2.3.2 Data on Samples for Electrical Measurements

Measurements were performed on a sample of  $\text{Mn}_3\text{B}_7\text{O}_{13}\text{I}$  supplied by H. Schmid. The sample was a  $(100)_{\text{cub}}$  cut wafer with area  $0.022 \text{ cm}^2$  and thickness  $55 \text{ \mu m}$ . Both faces of the sample were fully electroded with evaporated gold on chromium. The sample was mounted in a heating stage of a polarizing microscope to permit visual control of the domain state throughout the entire temperature range of the measurements. A complete poling of the sample was accomplished with a relatively small dc field of  $2\text{-}4 \text{ kV/cm}$  applied during slow cooling through the Curie point

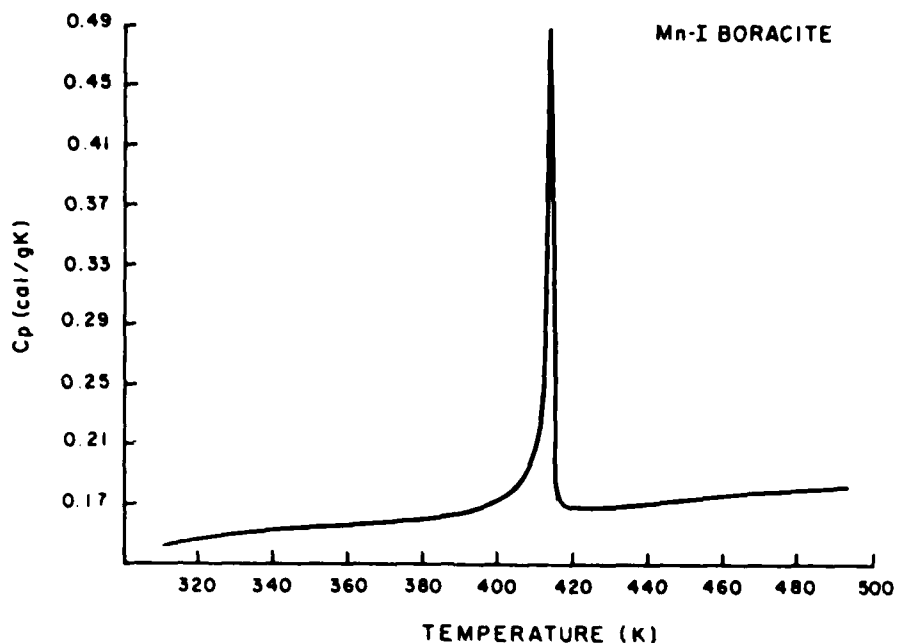


Figure 15. Specific heat of MnI boracite.

(134°C) to room temperature. After poling, the sample remained poled on heating up to the transition point in absence of a biasing field.

### 2.3.3 Birefringence

The spontaneous birefringence,  $n_s$ , perpendicular to the direction of the spontaneous polarization was measured with white light by means of a tilting compensator (Leitz 1350M). Figure 16 shows the results of the birefringence vs. temperature measurement. The shape of this curve is similar to that reported by Schmid and Tippman (Ref. 4), however, the magnitude of  $n_s$  in our measurement is smaller by a factor of  $\sim 3$ . As was pointed out by Schmid and Tippman, the behavior of  $n_s$  in MnI boracite is unusual and does not seem to reflect the temperature dependence of the order parameter in this material.

### 2.3.4 DC Resistivity

The temperature dependence of the bulk dc resistivity  $\rho$  was measured at 10 V using a Keithley 610 electrometer. Figure 17

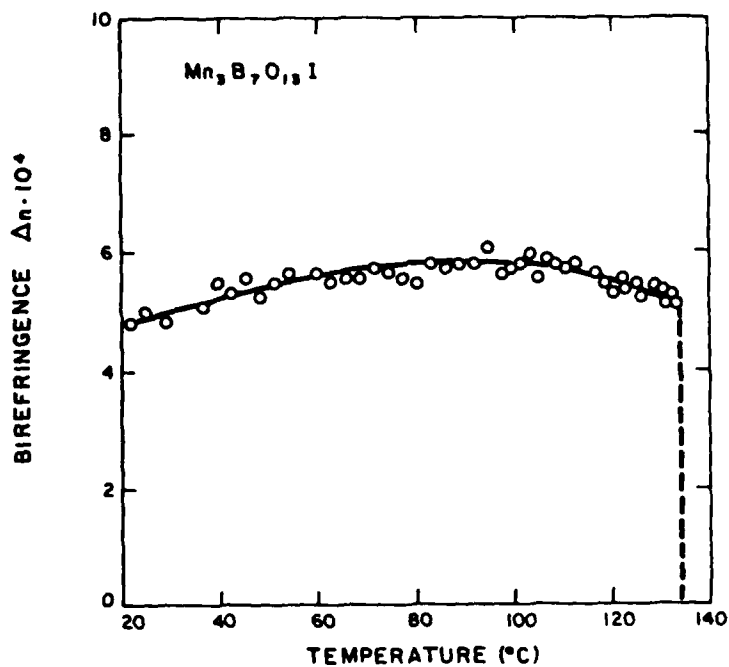


Figure 16. Birefringence perpendicular to the spontaneous polarization in  $Mn_3B_7O_{13}I$ .

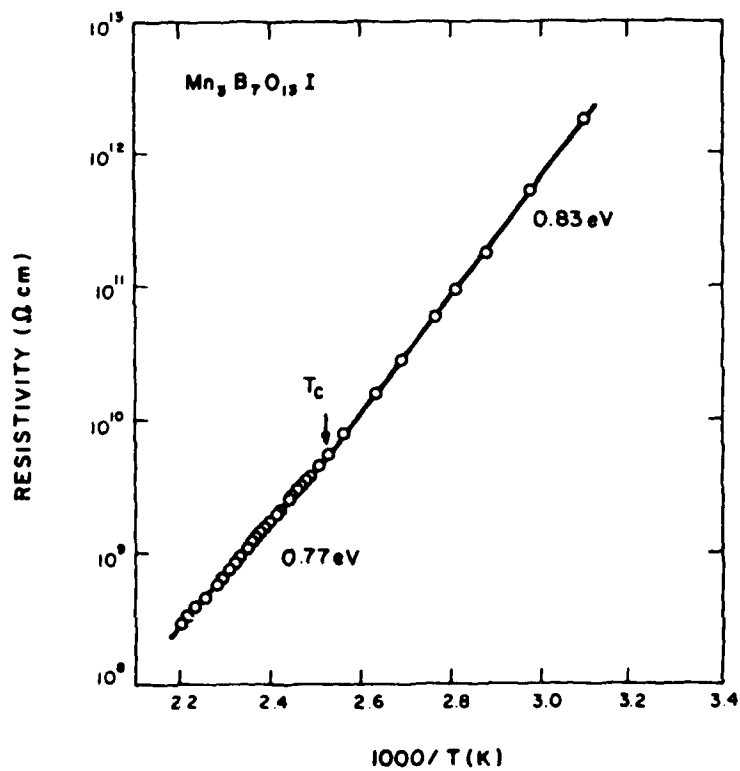


Figure 17. Log resistivity vs. reciprocal temperature in  $Mn_3B_7O_{13}I$ .

shows the logarithm of  $\rho$  vs. the reciprocal temperature. The dc resistivity in this sample was relatively high and decreased exponentially with temperature. Activation energies of 0.83 eV and 0.77 eV were obtained below and above  $T_c$  respectively.

### 2.3.5 Dielectric Constant

Measurement of the dielectric constant as a function of temperature was made in a field of 27 V/cm at 10 kHz, using a Hewlett Packard 4274A LCR meter. Our results (Fig. 18) showed that, in contrast to  $\text{Fe}_3\text{B}_7\text{O}_{13}\text{I}$  and similarly to  $\text{Cu}_3\text{B}_7\text{O}_{13}\text{Cl}$ , the dielectric constant of  $\text{Mn}_3\text{B}_7\text{O}_{13}\text{I}$  exhibits a sharp jump downward at  $T_c$  upon heating. This unusual behavior was observed so far only in  $\text{Cu}_3\text{B}_7\text{O}_{13}\text{Cl}$ . Upon heating the dielectric constant rose from a value of 11 at room temperature to a peak value of 27 at 134°C. It then jumped sharply to 19 and continued to decrease slowly thereafter. The dissipation factor was less than 1.2% over the entire temperature range of the measurement.

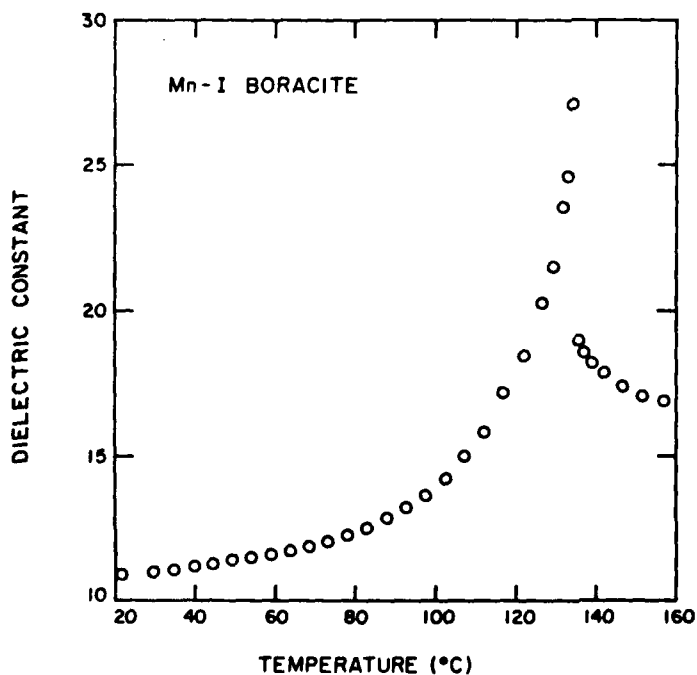


Figure 18. Dielectric constant at 10 kHz as a function of temperature in  $\text{Mn}_3\text{B}_7\text{O}_{13}\text{I}$ .

### 2.3.6 Pyroelectric Coefficient and Ratio p/c

Measurement of the pyroelectric coefficient,  $p$ , was performed using the Byer and Roundy and the charge integration techniques. The results are shown in Figure 19. Upon heating the pyroelectric coefficient rose from a value of  $2.4 \text{ nC/cm}^2\text{K}$  at  $30^\circ\text{C}$  to a value of  $17.5 \text{ nC/cm}^2\text{K}$  at  $110^\circ\text{C}$ . The measurement above  $110^\circ\text{C}$  was impeded by nonpyroelectric background currents.

Using the dynamic technique we were able to extend the measurement of the ratio  $p/c$  up to the Curie point. The results obtained are shown in Figure 20. This measurement was calibrated by setting  $p = 6.5 \text{ nC/cm}^2\text{K}$  and  $c = 2.66 \text{ J/cm}^3\text{K}$  at  $80^\circ\text{C}$ . This calibration is based on specific heat data obtained from a different sample of MnI boracite grown in our lab, (Par. 2.3.1) and the direct measurement of  $p$  on the same sample used in these dynamic measurements.

The behavior of  $p/c$  in  $\text{Mn}_3\text{B}_7\text{O}_{13}\text{I}$  indicates a strong temperature dependence of the spontaneous polarization, which was not expected on the basis of the weak temperature dependence of the birefringence in this material.

### 2.3.7 Figure of Merit

Figure 21 shows the temperature dependence of the figure of merit,  $M = p/\epsilon c$ , as obtained from the dynamic measurement of  $p/c$  and our direct measurement of  $\epsilon$  at 10 kHz. This data indicate that despite the different dielectric and pyroelectric behaviors of  $\text{Mn}_3\text{B}_7\text{O}_{13}\text{I}$  and  $\text{Fe}_3\text{B}_7\text{O}_{13}\text{I}$ , the behavior of the figure of merit in these materials is similar. The figure of merit of  $\text{Mn}_3\text{B}_7\text{O}_{13}\text{I}$  is  $\sim 10^3 \text{ cm}^2/\text{C}$  at room temperature and it rises to a peak value of  $5.3 \times 10^3 \text{ cm}^2/\text{C}$  at  $\sim 130^\circ\text{C}$ . For the figure of merit in  $\text{Fe}_3\text{B}_7\text{O}_{13}\text{I}$  we found a room temperature value of  $1.4 \times 10^3 \text{ cm}^2/\text{C}$  and a peak value of  $6.3 \text{ cm}^2/\text{C}$  at  $\sim 71^\circ\text{C}$ .

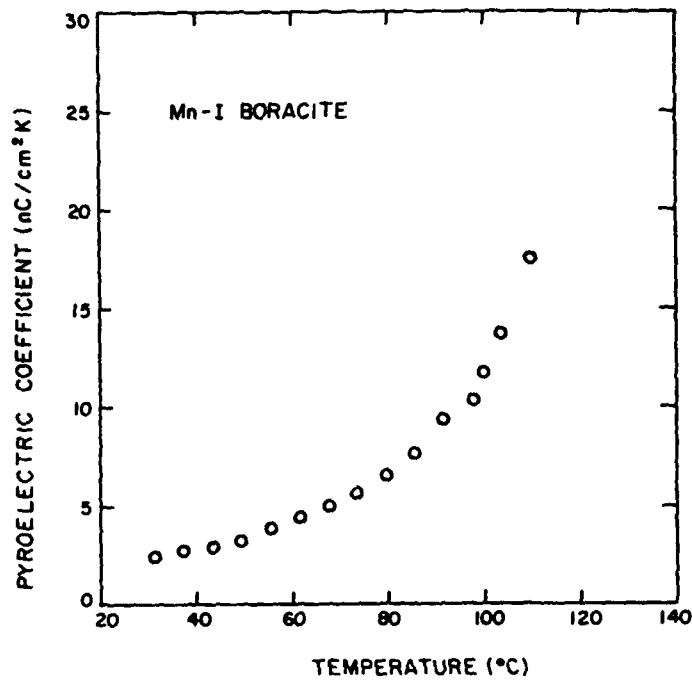


Figure 19. Pyroelectric coefficient vs. temperature in  $Mn_3B_7O_{13}I$ .

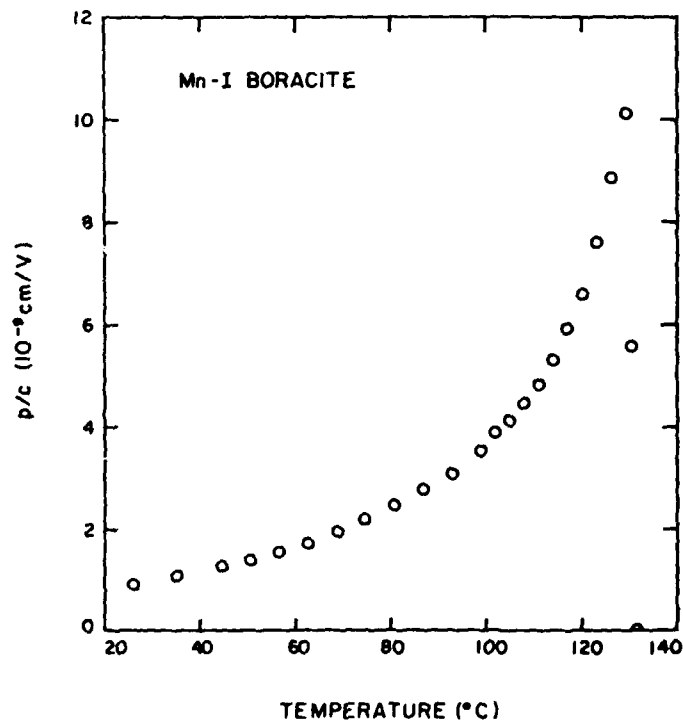


Figure 20. Ratio p/c vs. temperature in  $Mn_3B_7O_{13}I$ .

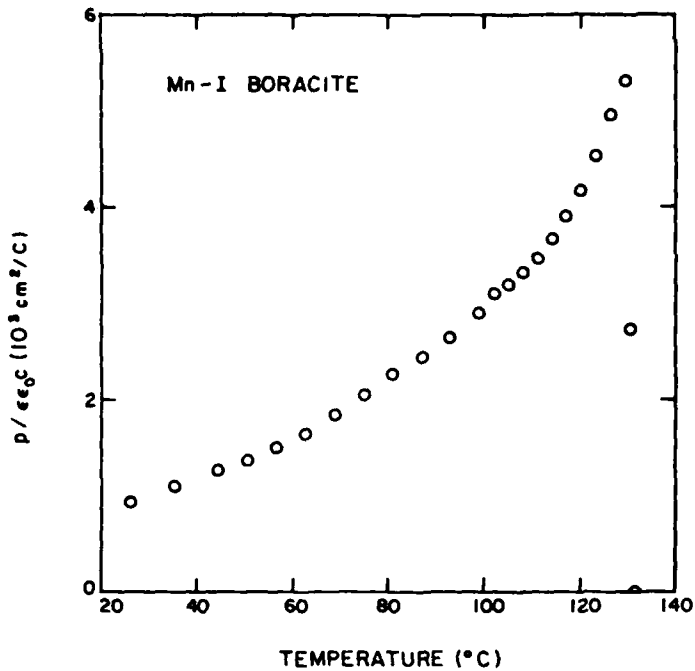


Figure 21. Temperature dependence of the figure of merit in  $Mn_3B_7O_{13}I$ .

#### 2.4 NiBr Boracite Measurements

Measurements of the dielectric and thermal behavior of NiBr boracite were completed. Pyroelectric measurements were attempted but no results are available due to difficulties encountered in poling highly conductive samples and in eliminating the effects of large background currents which are not pyroelectric in origin. No evaluation of the figure of merit is thus available.

### 2.4.1 Specific Heat

The specific heat measurements for NiBr boracite were performed on a 42.02 mg sample received from H. Schmid (Fig. 22). In this sample, multiple peaks during the transition are clearly visible. The rapid rise in the specific heat begins at about 388.5 K where it has a value of about 0.2 cal/g K. The specific heat above the transition is about 0.18 cal/gK this is less than the value just below the transition.

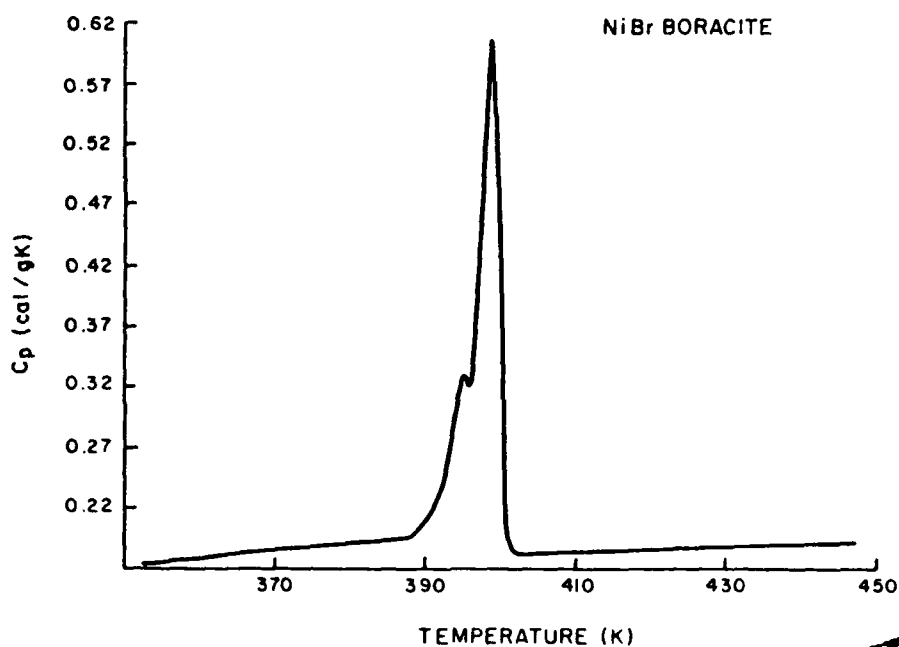


Figure 22. Specific heat of NiBr boracite.

### 2.4.2 Birefringence

Measurements of the temperature dependence of the spontaneous birefringence  $\Delta n_s \perp P_s$  were performed on a sample of  $Ni_3B_7O_{13}Br$  (#SHN1) supplied by H. Schmid. The results (shown in Fig. 23) are in good agreement with the data reported by Schmid and Tippmann (Ref. 4). In contrast to  $Cu_3B_7O_{13}Cl$ , the  $\Delta n_s$  versus T data in  $Ni_3B_7O_{13}Br$  indicate a strongly first order phase transition.

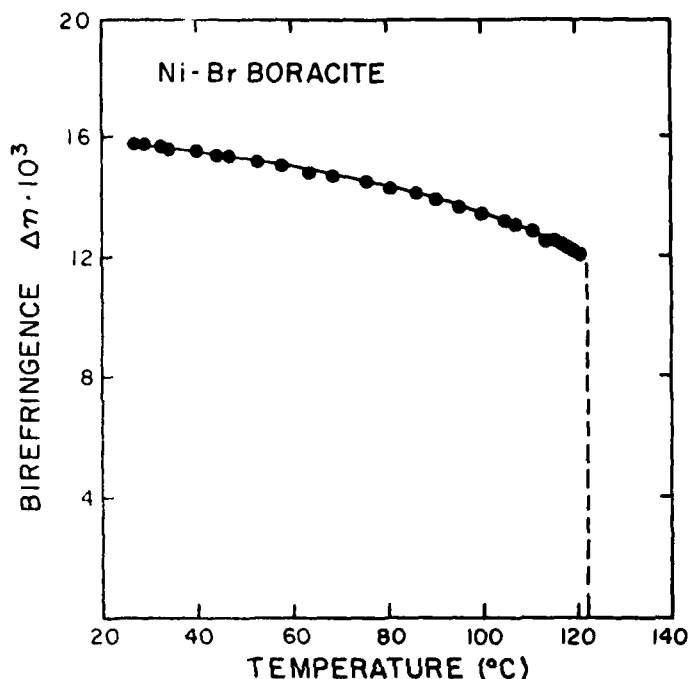


Figure 23. Spontaneous birefringence vs. temperature of  $\text{Ni}_3\text{B}_7\text{O}_{13}\text{Br}$ .

#### 2.4.3 Dielectric Constant

Measurements of dielectric constant were made on a sample (#20/B) supplied by Plessey. The poling state of this sample was unknown. Attempts were made to pole the sample by cooling it through the transition while applying a dc electric field of 10 kV/cm. However, pyroelectric measurements revealed that this procedure could yield only a partial reversal in the polarization of this sample.

Figure 24 shows the temperature dependence of  $\epsilon$  as measured in a field of 6 V/cm at 8 kHz. According to these data,  $\text{Ni}_3\text{B}_7\text{O}_{13}\text{Br}$  shows the normal behavior of boracites, i.e., the dielectric constant jumps upwards in the transition to the paraelectric phase. The jump of  $\epsilon$  in  $\text{Ni}_3\text{B}_7\text{O}_{13}\text{Br}$  is much greater than the corresponding jump in  $\text{Fe}_3\text{B}_7\text{O}_{13}\text{I}$ . The two reports in the literature on dielectric behavior of  $\text{Ni}_3\text{B}_7\text{O}_{13}\text{Br}$  (Refs. 6 and 7), do not call attention to this large jump of  $\epsilon$  at the transition.

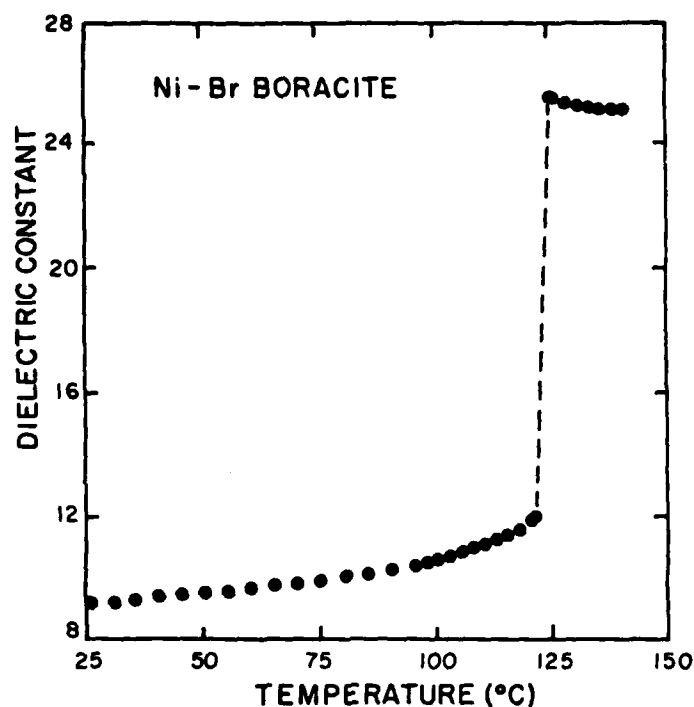


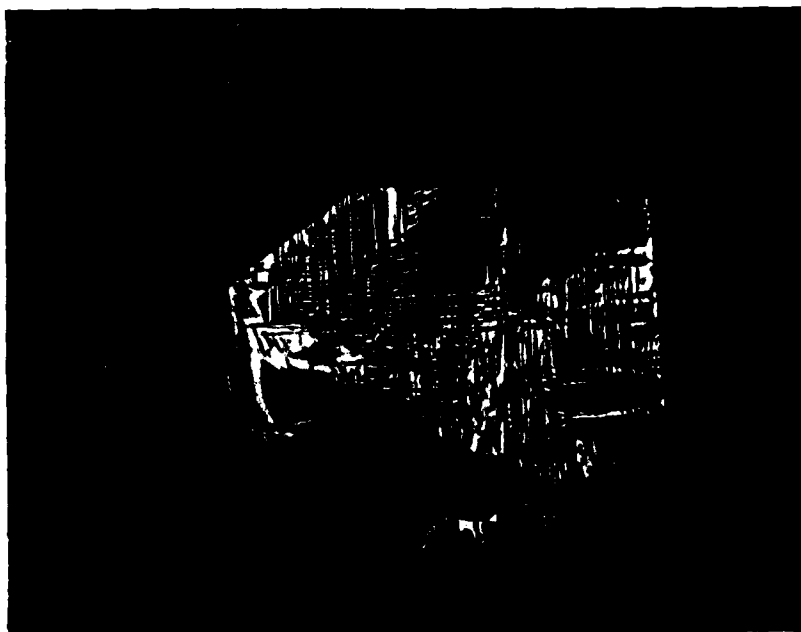
Figure 24. Dielectric constant at 8 kHz vs. temperature in  $\text{Ni}_3\text{B}_7\text{O}_{13}\text{Br}$ .

#### 2.4.4 DC Resistivity

Measurements of the dc resistivity,  $\rho$ , were performed on the sample #SHN1 (thickness 103  $\mu\text{m}$ , area 0.019  $\text{cm}^2$ ). This sample was fully electroded with evaporated transparent gold electrodes. The dc resistivity was determined by applying a dc voltage of 10 V to the sample and measuring the resultant current with a Keithley 610 electrometer. The poling state of this sample was as shown in Figure 25c. Figure 26 shows the logarithm of  $\rho$  versus the reciprocal temperature. These results show the same type of thermally activated behavior that we found in other boracites. The activation energies are 0.79 eV below  $T_c$  and 0.69 eV above  $T_c$ .



(a) Virgin sample.



(b) Sample cooled through the transition point in absence of a poling field.

Figure 25. Domains structure in  $\text{Ni}_3\text{B}_7\text{O}_{13}\text{Br}$  sample #SHN1 in various stages of a poling process.

(Sheet 1 of 3)

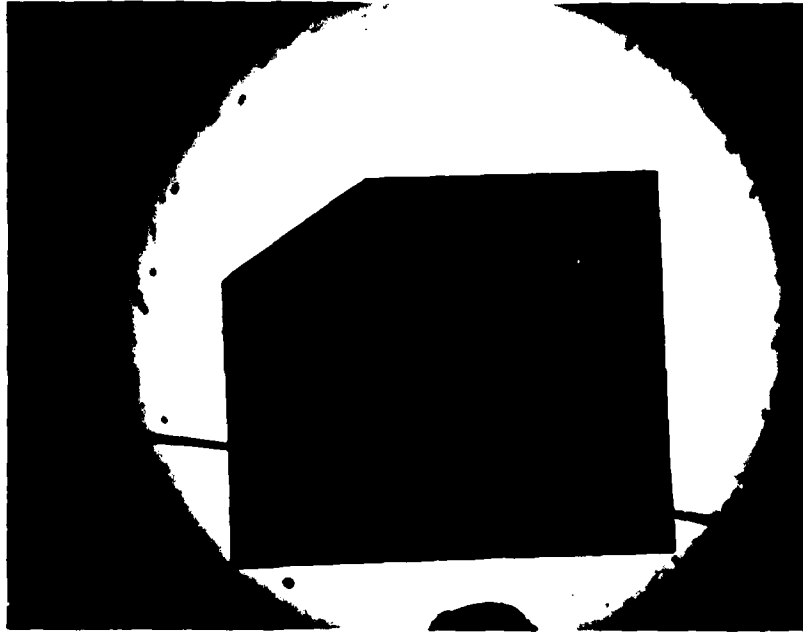


(c) Same as (b) with a poling field of 10 kV/cm applied to the sample during cooling.



(d) Same as (c) with a poling field of 16 kV/cm.

Figure 25. Domains structure in  $\text{Ni}_3\text{B}_7\text{O}_{13}\text{Br}$  sample #SHN1 in various stages of a poling process. (Cont'd)



(e) The crack in the sample as it is seen with unpolarized light.

Figure 25. Domains structure in  $\text{Ni}_3\text{B}_7\text{O}_{13}\text{Br}$  sample #SHN1 in various stages of a poling process. (cont'd)

(Sheet 3 of 3)

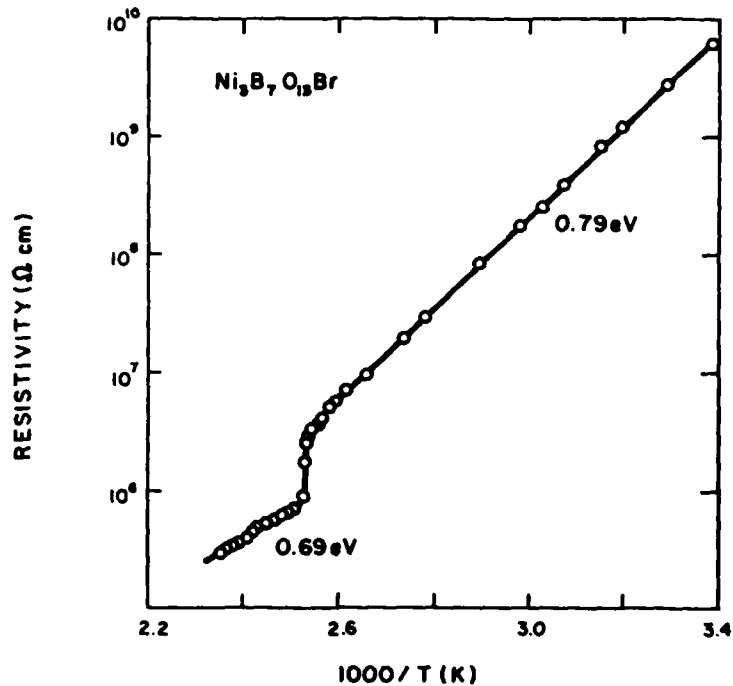


Figure 26. Log resistivity vs. reciprocal temperature in  $\text{Ni}_3\text{B}_7\text{O}_{13}\text{Br}$ .

#### 2.4.5 Poling and Pyroelectric Behavior

At present we do not have a reliable measurement of the pyroelectric coefficient in  $\text{Ni}_3\text{B}_7\text{O}_{13}\text{Br}$ . This is mainly due to experimental difficulties associated with the poling of this material. Various stages in the poling process of the sample #SHN1 are illustrated in Figure 25a-d. This sample was provided with transparent gold electrodes and mounted in a heating stage of a polarizing microscope to permit visual control of its domain state. Figure 25a shows the domain state of the virgin sample. The dark region is poled perpendicular to the surface of the sample. After heating the sample to above  $T_c$  and cooling it through the transition in absence of the poling field, a very complicated domain structure was formed (Fig. 25b). Repeating the same process with a poling field of 10 kV/cm yielded a partial poling (Fig. 25c). By increasing the poling field to 16 kV/cm the poling state was not improved and a crack was

developed across the sample (Fig. 25d). This crack is shown more clearly in Figure 25e which was taken without the polarizers. In other samples we noticed cracks after cooling them through  $T_c$  even in the absence of a poling field.

Several attempts were made to measure the pyroelectric current in the state shown in Figure 25c. Unfortunately in all these trials the pyroelectric current was buried in a large nonpyroelectric background current which could not be eliminated. The order of magnitude of the pyroelectric coefficient was estimated by measuring the pyroelectric response to a step light signal. The temperature change was determined by measuring the change in the resistance of the sample and the charge released was obtained by integrating the pyroelectric current. The values of the pyroelectric coefficient obtained in this way seem to be low compared to those that we have measured in other boracites. This is only a preliminary qualitative assessment on poor quality samples.

### 3. PROPIONATE MEASUREMENTS

The pyroelectric, dielectric and thermal behavior was measured for samples of dicalcium lead propionate (DLP) and dicalcium strontium propionate (DSP) grown at Philips Laboratories. These measurements are in good agreement with the theoretical predictions based on a second-order pseudo-proper thermodynamic potential. Each material reveals the expected broad maximum for the figure of merit near 52°C (DLP) and 0°C (DSP). The maximum values attained are (DLP:  $5 \times 10^3 \text{ cm}^2/\text{C}$ ; DSP  $5.7 \times 10^3 \text{ cm}^2/\text{C}$ ) just less than that of DTGFB and would be expected to increase once proper thermal annealing conditions are determined.

A thermal annealing process was developed to remove the internal bias field observed in the as-grown samples. The maximum value of the figure of merit is little affected by the presence or absence of a bias field. Any bias field - internal or external - causes a broadening of the temperature range over which the maximum remains large. Moreover, the presence of a bias field causes a reduction in the dielectric constant near the transition temperature without altering the figure of merit.

#### 3.1 Dicalcium Lead Propionate Measurements: As-Grown and Annealed Samples

Measurements of the dielectric constant,  $\epsilon$ , pyroelectric coefficient,  $p$ , and the ratios  $p/c$  and  $p/\epsilon c$  (where  $c$  is the volume specific heat) were made on as-grown samples of dicalcium lead propionate. The figure of merit shows a broad maximum of about  $5 \times 10^3 \text{ cm}^2/\text{C}$  near 52°C, thus confirming the estimate of large figures of merit for materials in the propionate family.

The as-grown samples contain a large internal bias field which can be eliminated by thermal annealing. Pyroelectric coefficient and dielectric constant measurements made on annealed samples show that the ratio  $p/\epsilon$  rises to the same high value as in the as-grown samples.

### 3.1.1 Sample Preparation

The tetragonal c-axis in dicalcium lead propionate single crystals was identified by x-ray precession photography and confirmed by optical observation under a polarizing microscope. Slices cut perpendicular to the c-axis were polished to a thickness of 50  $\mu\text{m}$  and electroded on both faces with evaporated antimony.

Samples of DLP were annealed in an evacuated ampoule for 21.5 hours at 270°C. After annealing, the samples retained their initial appearance indicating the absence of thermal decomposition.

### 3.1.2 Pyroelectric Coefficient

Figure 27 shows the temperature dependence of the pyroelectric coefficient  $p$  as measured by the Byer-Roundy technique. In the as-grown sample the pyroelectric coefficient increases from a value of  $1.2 \times 10^{-9} \text{ C/cm}^2 \text{ K}$  at 30°C to a peak value of  $7.0 \times 10^{-9} \text{ C/cm}^2 \text{ K}$  at 55°C, and decreases slowly thereafter. The absence of any anomaly in the behavior of  $p$  is associated with

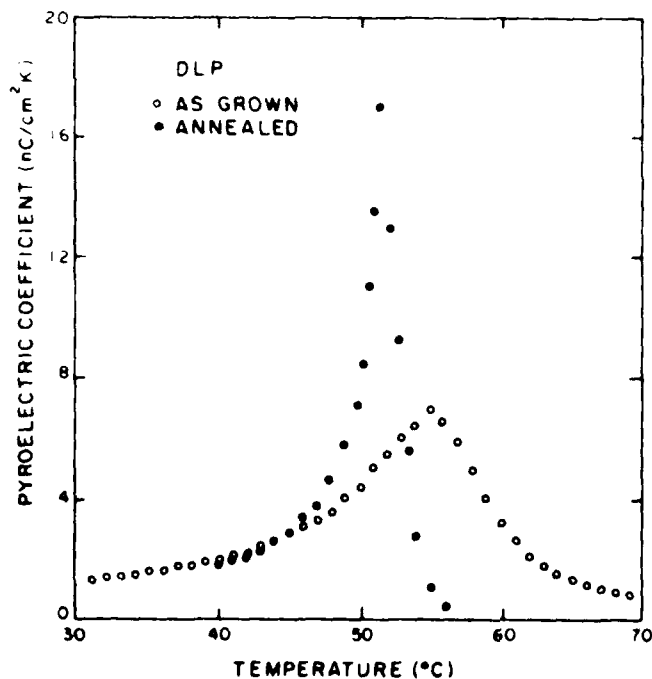


Figure 27. Temperature dependence of pyroelectric coefficient of annealed (closed circles) and as-grown (open circles) DLP.

an internal biasing field which normally exists in as-grown DLP crystals (Refs. 8,9). Comparing this result with our previously reported data of DLP (Ref. 9), we find good agreement up to 50°C. In the present measurement,  $p$  rises to a lower peak value, probably due to the presence of a higher internal biasing field.

In the annealed sample the peak of the pyroelectric coefficient became sharper and shifted toward lower temperatures. The tail of the pyroelectric coefficient above the peak is possibly due to a residual internal bias field, or to depoling of the sample before the transition point is reached.

### 3.1.3 Dielectric Constant

The dielectric constant was measured in a field of 10 V/cm at 8 kHz during slow heating. The results for both as-grown and annealed samples are shown in Figure 28. In the as-grown sample,  $\epsilon$  increases from a value of 4.3 at 25°C to a maximum value of 8.2 at about 56°C. The dielectric constant of the annealed sample rises sharply to a much higher peak which is shifted to the low temperature side. As noted by Takashige et al. (Ref. 8), the dielectric constant of annealed DLP follows a modified Curie-Weiss law,

$$\epsilon = \epsilon_c + C/|T_0 - T|.$$

Figure 29 shows  $1/(\epsilon - \epsilon_c)$  as a function of  $T$  taking  $\epsilon_c = 4$ . The values obtained for the Curie constants below and above the transition are about 17 and 24, respectively. These values differ appreciably from the values 32 and 69 reported by Takashige et al. (Ref. 8).

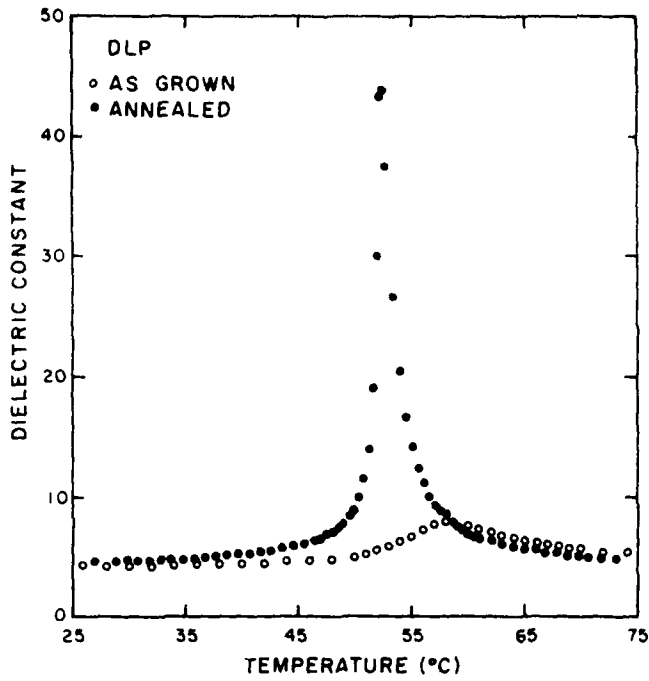


Figure 28. Temperature dependence of dielectric constant of annealed (closed circles) and as-grown (open circles) DLP.

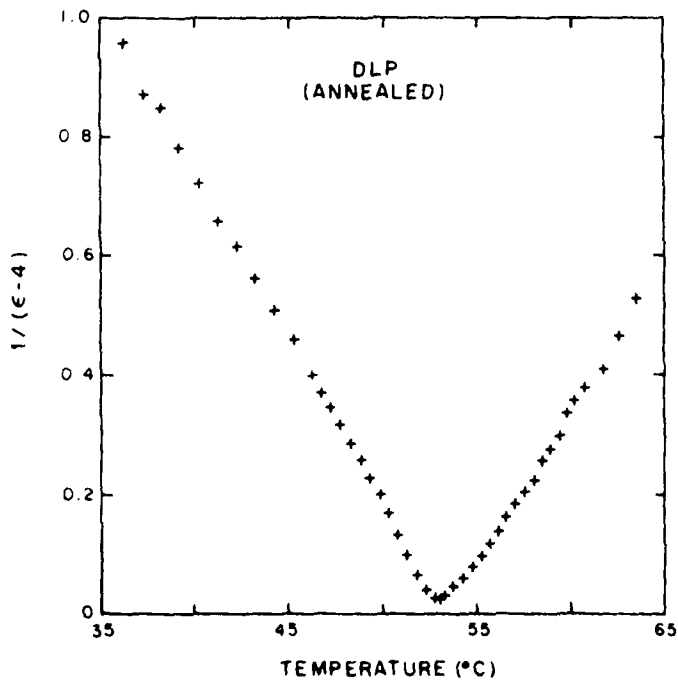


Figure 29. Fit of dielectric constant of annealed DLP to a modified Curie-Weiss law.

#### 3.1.4 Dynamic Measurement of p/c

Figure 30 shows the temperature dependence of the ratio  $p/c$  of the pyroelectric coefficient,  $p$ , to the specific heat,  $c$ , as measured in the as-grown and annealed samples by the dynamic response technique. Since the annealed sample tended to depole near the transition temperature, its measurements were made using an external bias field of 5 kV/cm. The temperature dependence of  $p/c$  follows closely the measurements of  $p$  reported in Figure 27 up to  $\sim 55^\circ\text{C}$ , confirming that the specific heat is constant to within a few percent, as expected. The scale on the  $p/c$  measurements is calibrated at  $40^\circ\text{C}$  by taking the values  $p = 2 \times 10^{-9} \text{ C/cm}^2 \text{ K}$  from our measurements and  $c = 1.8 \text{ J/cm}^3$  from the literature (Ref. 10).

#### 3.1.5 Dynamic Measurement of Figure of Merit $p/\epsilon c$

The direct measurement of  $p/\epsilon c$  in as-grown and annealed DLP by the dynamic response technique gives the result shown in Figure 31. To prevent depoling near the transition temperature, the measurements on the annealed samples were made with an external bias field of 5 kV/cm. The temperature dependence of the figure of merit shows a maximum value of about  $5 \times 10^3 \text{ cm}^2/\text{C}$  near  $52^\circ\text{C}$ . This value is larger than the figure of merit for TGS and about 80% of that of DTGFB. This result confirms our estimate of a large figure of merit for DLP.

It should be also noted that this maximum value would be higher and about equal to that of DTGFB if the dielectric constant at 8 kHz rather than at 250 Hz were used in evaluating  $p/\epsilon c$  (see below).

These measurements show that the peak value of  $p/\epsilon c$  is essentially unchanged by the presence of an internal or external bias field. However, the temperature width of this maximum is broader when the bias field is larger.

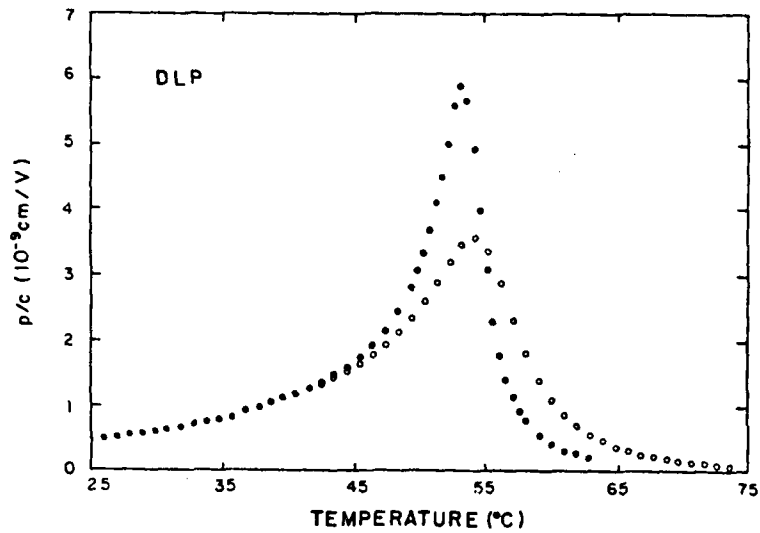


Figure 30. Temperature dependence  $p/c$  in as-grown DLP (open circles) and annealed DLP biased externally by a field of 5 kV/cm (closed circles).

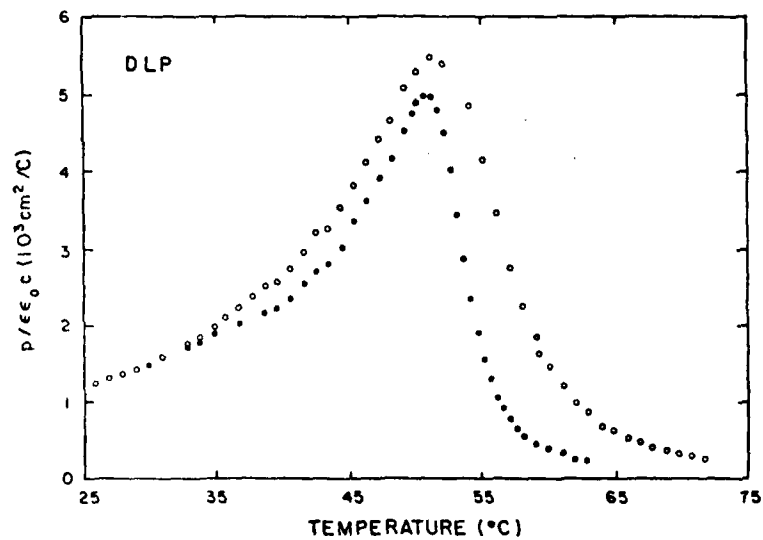


Figure 31. Dynamic response measurement of the figure of merit  $p/\epsilon\epsilon_0$ , in as-grown DLP (open circles) and annealed DLP biased externally by a field of 5 kV/cm (closed circles).

### 3.1.6 Dielectric Constant from Dynamic Measurements

Figure 32 shows the temperature dependence of  $\epsilon$  in as-grown and annealed DLP calculated from the dynamic measurements of  $p/\epsilon c$  and  $p/c$ . This determination of the dielectric constant is independent of the calibration of the dynamic response measurement. The result is in good qualitative agreement with the direct measurement of  $\epsilon$  reported above.

Quantitatively, the dynamic measurement yields a large dielectric constant (about 7% at room temperature). A possible explanation is the difference in the measuring frequency in these two measurements: 8 kHz in the direct measurement and 250 Hz in the dynamic measurement. This explanation is supported by the observation of Nakamura et al. (Ref. 10) who measured the frequency dependence of the dielectric constant of DLP in the region 300 Hz - 10 kHz. They found that at higher frequencies the entire  $\epsilon$  versus T curve is lower.

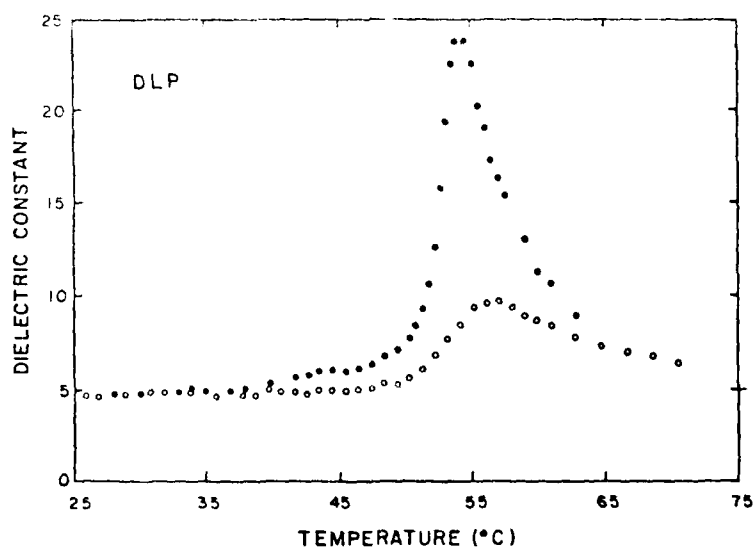


Figure 32. Dielectric constant as determined from dynamic response measurements in as-grown DLP (open circles) and annealed DLP biased externally by a field of 5 kV/cm (closed circles).

### 3.1.7 Discussion

Results of dielectric and pyroelectric measurements on an annealed sample show that the annealing process removes the internal bias field as reported in the literature.

Using the measured values of  $p$  and  $\epsilon$ , the calculated ratio  $p/\epsilon$  as a function of temperature is shown in Figure 33 for annealed and as-grown samples of DLP. It is seen that although the peak in the annealed sample is sharper, in both samples  $p/\epsilon$  rises to the same maximum value.

The dynamic measurements of  $p/c$  and  $\epsilon$  are in good agreement with the direct measurements of  $p$  and  $\epsilon$ . These measurements show that the bias field causes the peaks in both  $p/c$  and  $\epsilon$  to decrease while leaving essentially unchanged the ratio  $p/\epsilon c$ . Thus, by adjusting the bias field it is possible to tune the peak dielectric constant over a reasonable range from 10 to 25 without changing the figure of merit.

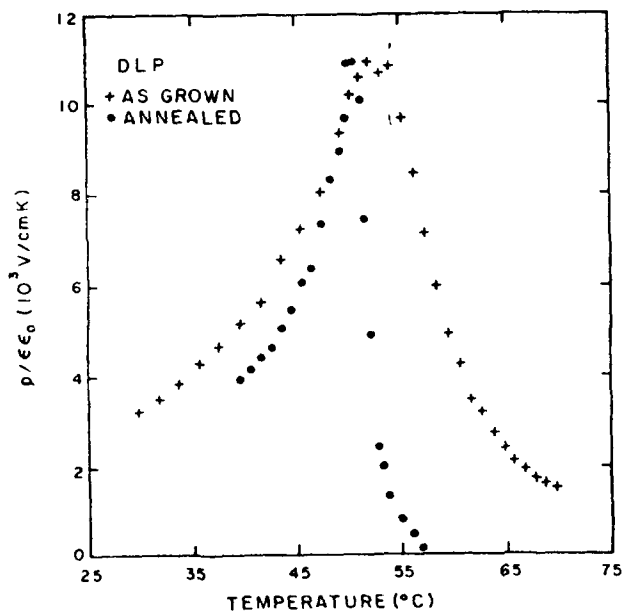


Figure 33. Temperature dependence of the ratio  $p/\epsilon$  in annealed (circles) and as-grown (crosses) DLP.

### 3.2 Dielectric, Pyroelectric and Thermal Measurements in As-Grown and Annealed Samples of DSP [ $\text{Ca}_2\text{Sr}(\text{C}_2\text{H}_5\text{COO})_6$ ]

Pyroelectric, dielectric and thermal measurements on as-grown and thermally annealed sample of dicalcium strontium propionate reveal a figure of merit with a broad maximum of about  $5.7 \times 10^3 \text{ cm}^2/\text{C}$  at about  $0^\circ\text{C}$  in the annealed material. This value is within 10% of DTGFB; moreover one would expect a larger value once optimum annealing conditions are determined.

The as-grown samples of DSP exhibit internal bias fields an order of magnitude less than those found in DLP.

#### 3.2.1 Dicalcium Strontium Propionate: Specific Heat

The specific heat of a 3.05 mg sample of dicalcium strontium propionate [ $\text{Ca}_2\text{Sr}(\text{C}_2\text{H}_5\text{COO})_6$ ] (DSP) was measured on the Perkin-Elmer Differential Scanning Calorimeter. The data was calibrated against the NBS standard for sapphire. The temperature dependence of the specific heat between 230 K and 325 K is shown in Figure 34.

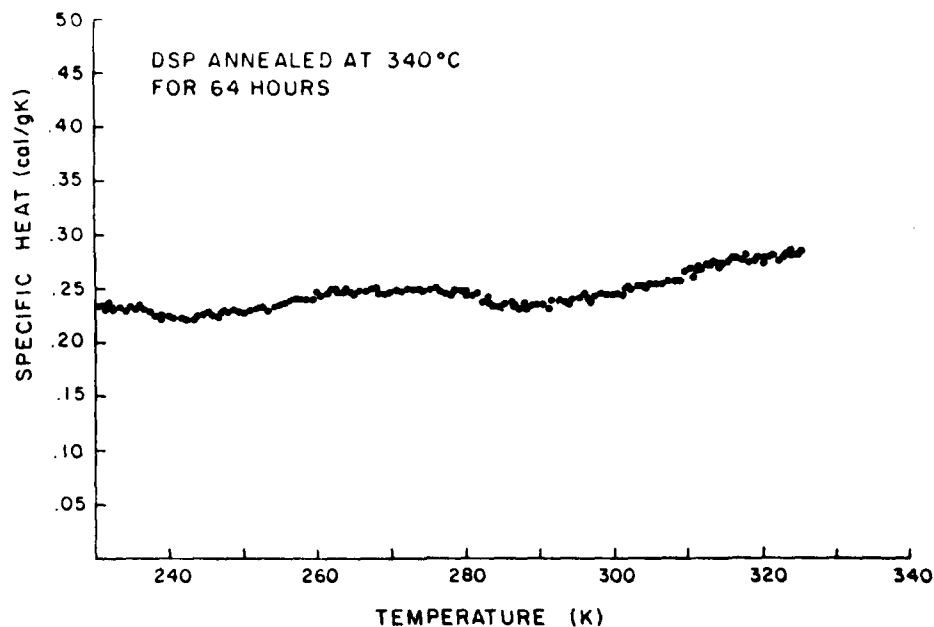


Figure 34. Temperature dependence of specific heat of DSP between 230 K and 325 K.

As expected (Ref. 11) no anomaly occurs in the vicinity of the phase transition at 279 K within the experimental accuracy of  $\pm 5\%$ .

Using an X-ray density of  $1.508 \text{ g/cm}^3$ , the volume specific heat was determined to be about  $1.58 \text{ J/cm}^3 \text{ K}$  at 280 K. This low value confirms the reported value by Nakamura et al. (Ref. 10) and has been used in our calibration of the dynamic pyroelectric measurements of DSP.

### 3.2.2 Sample Preparation for Electrical Measurements

Slices of dicalcium strontium propionate (DSP) with faces perpendicular to the tetragonal c-axis were cut from a single crystal and polished to a thickness of  $110 \text{ }\mu\text{m}$ . Thermal annealing of samples was performed in evacuated, sealed quartz ampoules in two experiments: (a)  $270^\circ\text{C}$  for 16 hours and (b)  $340^\circ\text{C}$  for 64 hours. Samples were electroded on both faces with evaporated antimony.

### 3.2.3 Dielectric Constant

#### (1) As Grown Samples

The dielectric constant  $\epsilon$  was measured in a field of  $9 \text{ V/cm}$  at  $8 \text{ kHz}$  during slow heating and cooling. The results obtained in as-grown samples are shown in Figure 35. On heating,  $\epsilon$  rises from a value of  $\sim 7$  at  $-10^\circ\text{C}$  to a maximum value of 83 at  $\sim 8^\circ\text{C}$ . In a similar manner to that obtained in DLP, the cooling curve shows a higher peak which is shifted toward lower temperatures.

#### (2) Annealed Samples

The dielectric constant,  $\epsilon$  was measured in a field of  $8.3 \text{ V/cm}$  at  $8 \text{ kHz}$  during slow heating. The results for a sample annealed at  $340^\circ\text{C}$  for 64 hours are shown in Figure 36. The dielectric constant rises from a value of  $\sim 7$  at  $-10^\circ\text{C}$  to a maximum value of  $\sim 160$  at  $5.2^\circ\text{C}$ . The peak of  $\epsilon$  is about twice that obtained in the as-grown sample, and is slightly shifted to the low

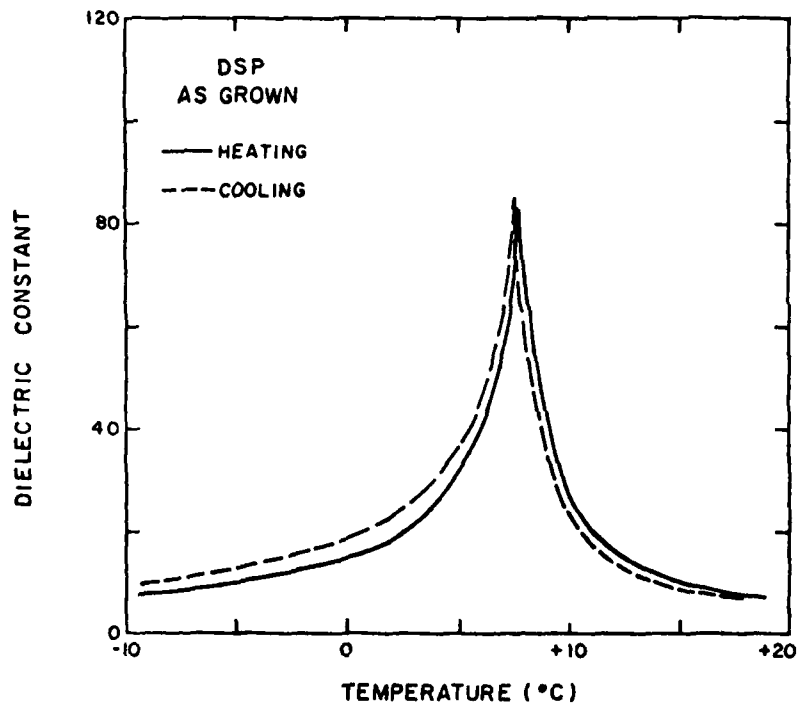


Figure 35. Temperature dependence of dielectric constant of as-grown DSP.

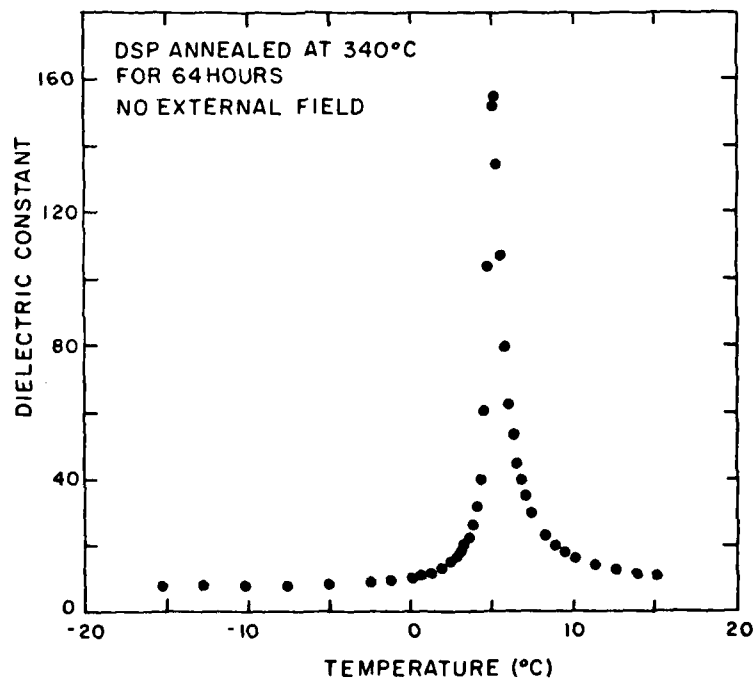


Figure 36. Dielectric constant vs. temperature for DSP annealed at 340°C for 64 hours.

temperature side. Samples annealed at 270°C for 16 hours showed dielectric behavior intermediate between the as-grown and 340°C annealed samples.

From the theoretical analysis (Ref. 12), the detailed temperature dependence of the dielectric constant of the annealed DSP is expected to follow a modified Curie-Weiss law:

$$\epsilon(T) = \epsilon_p + C^{\pm} / |T - T_0|$$

with different Curie constants  $C^{\pm}$  above and below the transition temperature  $T_0$ . As expected in the annealed samples, as the transition point is approached, the dielectric constant rises more steeply in the ferroelectric phase than in the paraelectric phase. The opposite behavior was found in as-grown samples and samples annealed at 270°C. Figure 37 shows a Curie-Weiss plot of a 340°C annealed sample close to the transition temperature using  $\epsilon_p = 4$ . The Curie constant,  $C^+$ , above the transition is 62 K, and,  $C^-$ , below the transition is 28 K. Another sample, annealed under the same conditions, yielded  $C^+ = 73$  K and  $C^- = 33$  K. These values are consistent with the data in the literature (Refs. 13, 14).

With regard to the internal bias fields observed in DSP, comparing the dielectric behavior of the annealed and as-grown samples shows that unlike DLP, as-grown DSP samples do not exhibit large internal biasing effects. The internal biasing field in the as-grown samples of DSP was estimated from hysteresis loops to be less than 0.5 kV/cm. In as-grown samples of DLP, we found internal biasing fields of the order of 10 kV/cm.

The effects of an external biasing field on the dielectric behavior of an annealed sample of DSP is shown in Figure 38. As the applied field was increased from 0 to 4.5 kV/cm, the peak of  $\epsilon$  became broader and shifted to the higher temperature side. This behavior is in accordance with the theoretical prediction for the field dependence of  $\epsilon$  in pseudoproper ferroelectrics.

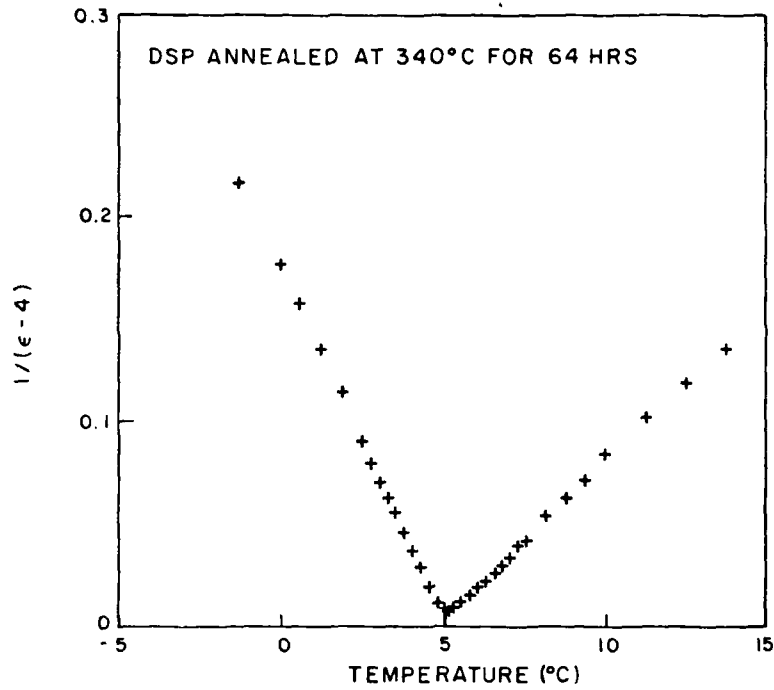


Figure 37. Modified Curie-Weiss law in annealed DSP.

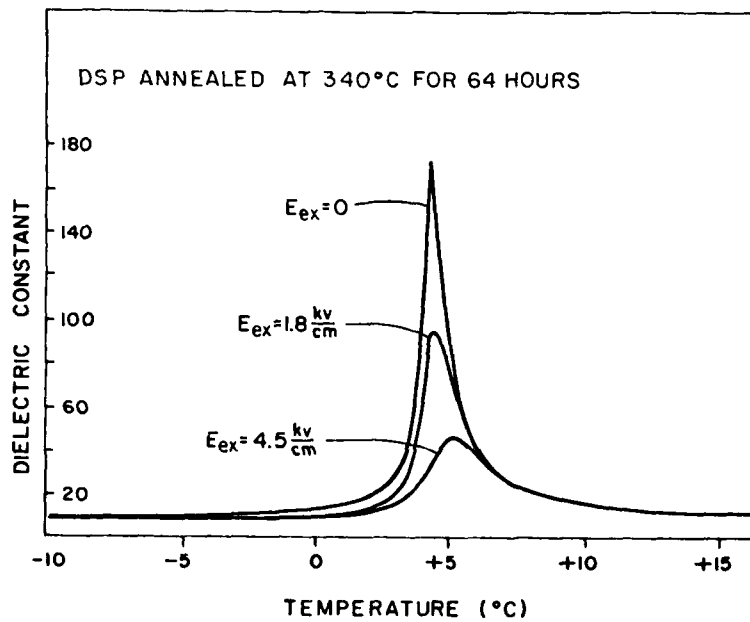


Figure 38. Temperature dependence of dielectric constant of annealed DSP at 340°C for 64 hours under various biasing fields.

### 3.2.4 Spontaneous Polarization and Pyroelectric Coefficient, Annealed DSP

Measurements of the temperature dependence of the spontaneous polarization,  $P_s$ , for annealed DSP were attempted using both hysteresis loops and the charge-integration technique. DSP annealed at 340°C did not exhibit well defined, saturated hysteresis loops, while it did exhibit a charge integration curve yielding  $P_s$  values which are consistent with data in the literature. Figure 39 shows the temperature dependence of  $P_s$  in DSP found through the charge-integration technique. The curve through the experimental points in Figure 39 was obtained by a linear least-squares fitting of the theoretically expected behavior of  $P_s(T)$ :

$$P_s = K (T_0 - T)^{1/2}$$

to the data up to 0°C. For  $K$  and  $T_0$  we found the values of  $K = 4.26 \times 10^{-8} \text{C/cm}^2 \text{K}^{1/2}$  and  $T_0 = 6.86^\circ\text{C}$ . The deviation of the experimental points from the theoretical curve in the close vicinity of  $T_c$  is in accordance with the observation of Deguchi et al. (Ref. 13).

The temperature dependence of the pyroelectric coefficient,  $p$ , was obtained by differentiating the  $P_s$  versus  $T$  curve. The values of  $p$  obtained in this way are shown in Figure 40.

Table 1 compares the spontaneous polarization values in annealed DSP to those reported in the literature. It is seen that our  $P_s$  data for DSP agree well with the data reported by Matthias et al. (Ref. 15). However, they are lower than those reported by Takashige et al. (Ref. 8).

Table 1. Spontaneous Polarization of DSP ( $\mu\text{C/cm}^2$ ).

T(°C)	DSP annealed at 340°C	Matthias et al.	Takashige et al.
-10	0.18	0.17	0.23
-30	0.25	0.25	0.32
-45	0.30	0.30	0.37

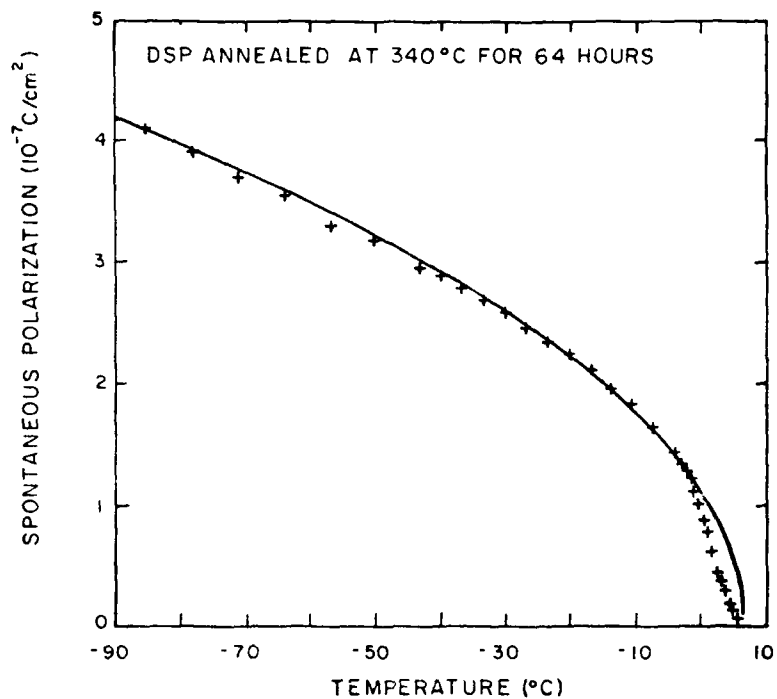


Figure 39. Spontaneous polarization of DSP annealed at 340°C for 64 hours measured by charge integration (crosses). The solid curve is the theoretical form.

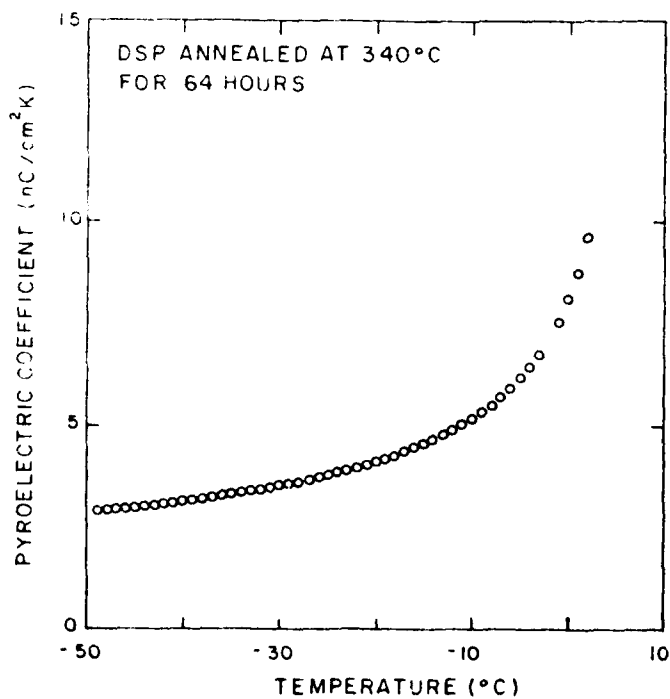


Figure 40. Pyroelectric coefficient of DSP annealed at 340°C for 64 hours obtained by differentiation of charge integration measurement of the spontaneous polarization.

Hysteresis loop measurements of the spontaneous polarization of DSP annealed at 270°C for 16 hours gave values for the spontaneous polarization  $P_s$  and the pyroelectric coefficient  $p$  somewhat lower than those measured in samples annealed at 340°C. This fact, and the larger values of  $P_s$  reported by Takashige et al. would suggest that even larger values than reported here for the pyroelectric coefficient would be obtained when final annealing conditions are determined.

### 3.2.5 Dynamic Measurements of $p/c$ and $p/\epsilon c$ on Annealed DSP

Figure 41 shows the temperature dependence of the ratio  $p/c$  as measured in a sample of DSP annealed at 340°C for 64 hours by the dynamic technique. Since the sample tended to depole near the transition temperature, the measurements were made using a small external bias field of 0.36 kV/cm. The  $p/c$  scale in this measurement was calibrated at -30°C by taking the values  $p = 3.5 \times 10^{-9} \text{ C/cm}^2\text{K}$  from our charge integration measurement, and  $c = 1.65 \text{ J/cm}^3\text{K}$  from the literature (Ref. 10) and our own measurements. Combining our data on  $p$  (Fig. 40) and  $c$  gives values for  $p/c$  which agree well with the values of  $p/c$  measured by the dynamic technique up to 0°C.

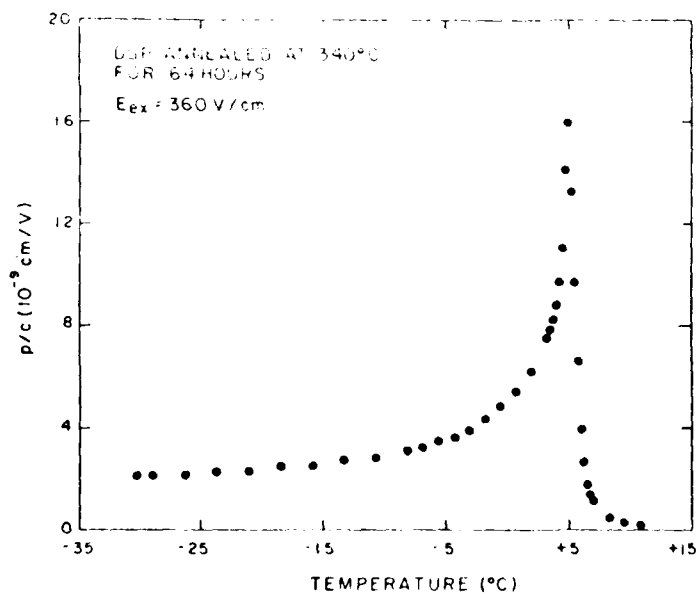


Figure 41. Temperature dependence of ratio  $p/c$  in annealed DSP as measured by dynamic technique.

A direct measurement of the figure of merit,  $p/\epsilon c$ , in the same sample gives the result shown in Figure 42. The figure of merit increases slowly from a value of  $4 \times 10^3 \text{ cm}^2/\text{C}$  at  $-30^\circ\text{C}$  to a peak value of  $5.7 \times 10^3 \text{ cm}^2/\text{C}$  at  $\sim -1.4^\circ\text{C}$ , and decreases rapidly thereafter. This behavior is different from that of improper ferroelectrics like TMO and proper ferroelectrics like TGS (Ref. 16) and demonstrate the pseudo-proper character of DSP.

Figure 43 shows calculated curves of  $p/\epsilon c$  for various biasing fields, based on the free-energy model for a pseudo-proper ferroelectric, using  $K = 4.26 \times 10^{-8} \text{ C/cm}^2 \text{ K}^{1/2}$ ,  $C = 70 \text{ K}$ , and  $T_0 = 5 \text{ K}$ . A comparison of Figures 42 and 43 show that the shape of the temperature dependence of the figure of merit is in good agreement with the theoretical prediction.

In summary, these measurements yield a peak value for the figure of merit of annealed DSP of about  $5.7 \times 10^3 \text{ cm}^2/\text{C}$ ; this value is larger than the figure of merit of TGS and close to that of DTGFB. Moreover, a somewhat larger value is to be expected once the optimum annealing conditions are determined.

Another important observation is that this large figure of merit is attained over a very wide temperature interval.

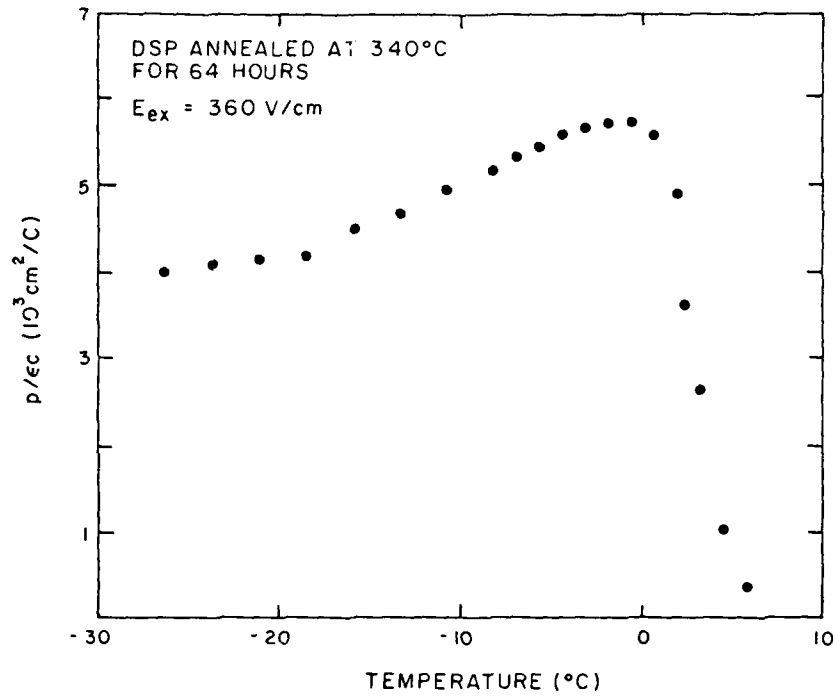


Figure 42. Temperature dependence of the figure of merit,  $p/\epsilon c$ , in annealed DSP as measured by dynamic technique.

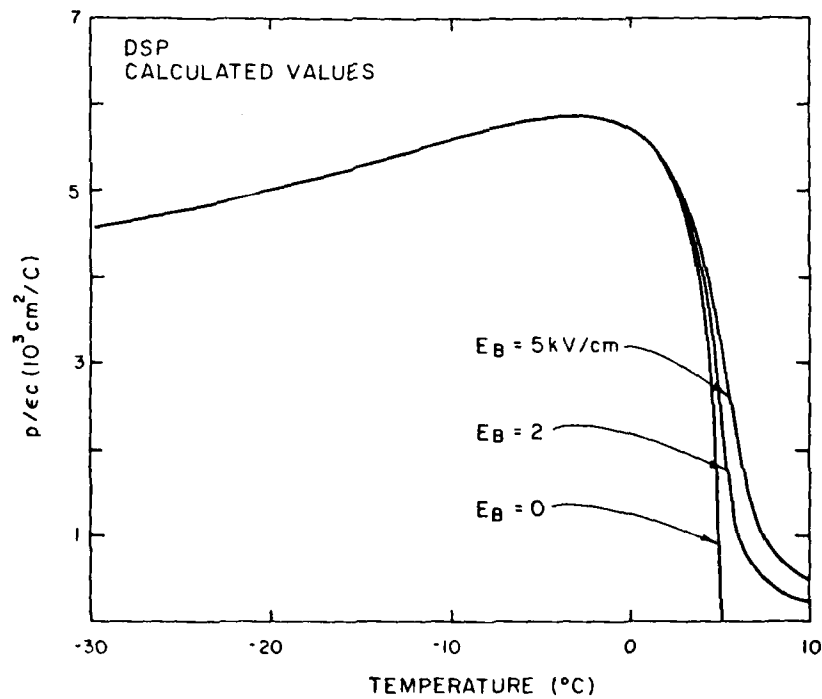


Figure 43. Calculated temperature dependence of  $p/\epsilon c$  for DSP under biasing fields of 0, 2, and 5 kV/cm.

#### 4. BORACITE CRYSTAL GROWTH

A novel technique for the synthesis of boracite powders was developed. This low-temperature, low-pressure hydrothermal synthesis gives the highest yield of boracite material among all known methods.

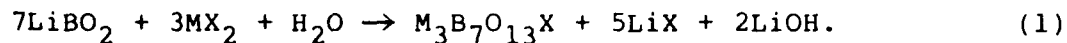
Extensive experimentation on the hydrothermal growth of boracite single crystals was carried out. Studies included synthesis-growth and dissolution-transport in both acid and basic media. Variations in temperature, pressure, reactants, reactant loading sequence, reactant concentration, and mineralizer concentration were examined to determine the optimum conditions for growth of single crystals. A number of experimental conditions were identified which produce high quality crystals, about 0.5 mm on an edge in high yield.

A novel three-zone vapor transport technique was developed for the growth of boracite. Large single crystals (> 10 mm on edge) of NiBr boracite were produced. Methods were developed to control nucleation and eliminate cracking of crystals during growth. Experimentation was begun on the growth of MnI boracite and mixed crystals of NiBrCl and FeMnI boracite using this technique.

##### 4.1 Hydrothermal Synthesis of Boracite Powders

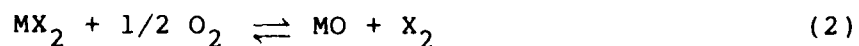
A novel method of boracite synthesis was developed. The most general method of synthesizing boracites has been the vapor transport method of Schmid (Ref. 17) and its various modifications (Refs. 18-20). From a synthetic point of view, this method of preparation has the following disadvantages. A sophisticated experimental arrangement (susceptible to explosion) is required, a relatively low yield of boracite is obtained, high reaction temperatures are required, and the metal borates are produced which are often difficult to separate from the boracite. The new synthesis of boracites is accomplished by a low-temperature low-pressure hydrothermal method which eliminates all of these

problems. The boracite syntheses can be described by the following stoichiometric reaction:



Additional water has been found to be a suitable solvent system which increases the kinetics and the completeness of the reaction. Consequently, the metal halide and the lithium metaborate may be used in hydrated forms with little or no effect upon the reaction. This is of considerable convenience since drying the metal halide and lithium metaborate to the anhydrous state imposes some difficulty. The reaction is carried out in a 250 cm<sup>3</sup> Paar pressure reaction vessel constructed of the alloy hastelloy C. The vessel is equipped with a thermocouple well and a pressure gauge. The temperature of the reaction vessel is recorded by a chromel-alumel thermocouple and read with a digital voltmeter. A temperature stability of  $\pm 3^\circ\text{C}$  is maintained by a Paar temperature controller.

In a typical synthesis applied to  $\text{Ni}_3\text{B}_7\text{O}_{13}\text{Br}$ , 34.8 g of  $\text{LiBO}_2$  (99% Apache Chemicals), 65.6 g of  $\text{NiBr}_2$  (99.99% Apache Chemicals) and 21.8 g of deionized-deoxygenated  $\text{H}_2\text{O}$  were placed in the reaction vessel under an argon atmosphere at atmospheric pressure. The inert atmosphere prevents the competing reaction,

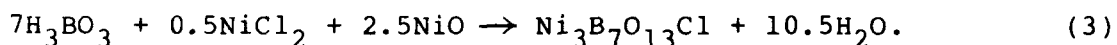


from occurring which leads to the formation of unwanted metal borates. The contents were heated to a temperature of  $270^\circ\text{C}$  and a pressure of 26 atm in about 3 hours. After 60 hours, the vessel was rapidly cooled ( $\sim 1$  hour) down to room temperature. The product which consists of fine boracite crystal ( $\sim 0.01$  mm) was treated with a hot 10% HCl and then boiled in excess water for several hours to dissolve unreacted material as well as water soluble by-products. A repeated water rinsing followed by filtration and air drying resulted in 51.4 g of  $\text{Ni}_3\text{B}_7\text{O}_{13}\text{Br}$  (a yield of  $> 95\%$ ). The chemical integrity of the boracite was verified by wet chemical analysis, X-ray powder diffraction and

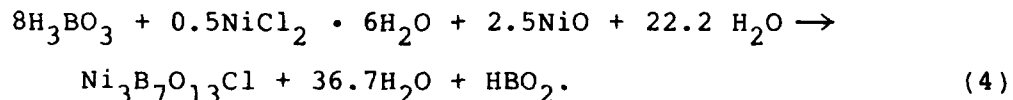
infrared absorption spectra. Under similar conditions, the boracites  $\text{Ni}_3\text{B}_7\text{O}_{13}\text{I}$ ,  $\text{Zn}_3\text{B}_7\text{O}_{13}\text{Br}$  and  $\text{Mg}_3\text{B}_7\text{O}_{13}\text{Cl}$  were synthesized in yields exceeding 95%. These results represent the highest yields of boracites reported to date by any method. This work shows also that boracites can form at temperatures under 300°C and under pressures of 30 atm.

#### 4.2 Hydrothermal Growth of Boracite Crystals

The only systematic study of the growth of boracite using the hydrothermal method was reported by Joubert and co-workers in 1972 (Ref. 21). The general reaction is of the form:



However, our analysis of Joubert's data from which they claimed the "best crystals" were grown, indicates the reaction fits the equations,



Further analysis of their data reveals an operating pressure of 650 atm at 450°C. It is interesting to note that Reaction (4) shows  $\text{HBO}_2$  is formed; we have found  $\text{HBO}_2$  to be essential for the formation of boracite. Moreover, examination of the P-T phase diagram of the  $\text{H}_2\text{O} - \text{B}_2\text{O}_3$  system also shows that  $\text{HBO}_2$  is formed as a stable phase (Ref. 22). Our hydrothermal work involved expanding the initial study of Joubert with the goal of producing crystals of millimeter size.

##### 4.2.1 Apparatus

The hydrothermal growth was performed in a standard four station Tem-Pres Model HR-1B-4 hydrothermal unit using standard Tuttle-type reactors. Operating temperatures were measured using thermocouples externally mounted in the reactor wall. Internal

capsule pressures were estimated from Kennedy's P-T curves for pure water at constant volume (Ref. 23). Pressure balancing, to prevent the quartz ampoules from rupturing, was accomplished using a pressure intensifier capable of delivering up to 45 Kpsi. The quartz ampoules were 8 mm in diameter and 150 mm long with a wall thickness of 1 mm. These ampoules were only used in studying growth under acidic and neutral conditions. To study growth under basic conditions, gold tubing 6 mm in diameter and 60 mm long was used.

#### 4.2.2 Growth from Acidic Media

The boracite  $\text{Ni}_3\text{B}_7\text{O}_{13}\text{Br}$  was selected for growth studies. We will designate this composition in the shortened notation Ni-Br. Three distinct methods of experimentation were investigated. First, a Joubert-type hydrothermal synthesis was used with variations of temperature, pressure, loading sequence reactant, reactant concentration, and mineralizers. A second set of experiments were designed to investigate the effects of different starting components on the size of the boracite crystals produced. Finally, the classical direct dissolution/ deposition method of hydrothermal growth was examined using both acidic and basic solvents.

##### (1) Standard Composition

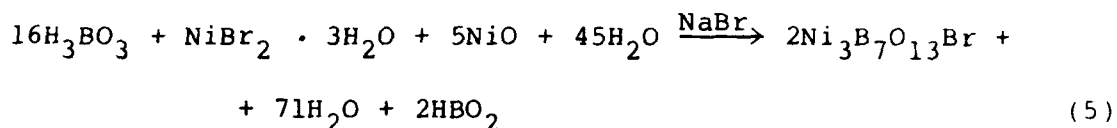
Our standard composition was derived from the work of Joubert, et al. (Ref. 21) and consisted of:

$\text{H}_3\text{BO}_3$	=	2.5 g
$\text{NiBr}_2$	=	0.546 g
$\text{NiO}$	=	0.934 g
$\text{NaBr}$	=	0.257 g
$\text{H}_2\text{O}$	=	2.0 g

The quantities shown above were always used in the same proportions and the exact quantity defined by the pressure and temperature desired. The components used in these experiments were contained in sealed quartz ampoules. The ampoules were placed

in the standard Tuttle reactors used for hydrothermal growth. In order to prevent rupture of the quartz ampoules an over-pressure of ~ 50 atm above the calculated internal ampoule pressure was applied to the reactor via a pressure intensifier. A temperature gradient of about 100°C was maintained between the top and bottom of the ampoules.

The overall chemical reaction can be represented by:



The reaction is written in this form to emphasize that HBO<sub>2</sub> is an essential component for the successful formation of boracite.

In Reaction (5) the use of NaBr was based on the catalytic activity of alkali halides in the formation of boracite. The use of NaBr as a mineralizer was found to increase the size of the boracite formed from a microscopic powder to single crystals approaching 0.25 mm (on edge). This confirms the data reported by Joubert et. al. on the effect of NaCl on the growth of NiCl boracite (Ref. 21). Table 2 lists the P-T data determined for the NiBr system. An analysis of this data clearly indicate the following trends:

- Operating temperatures above 300°C are detrimental to crystal growth. At 350°C, regardless of pressure, the boracite crystals formed exhibit rounded edges which is indicative of severe dissolution.
- Transport of boracite occurs at 50 atm, and the size of the crystals formed increase as the temperature is increased.
- The temperature range 250-300°C yields well formed, flawless, crack-free crystals at 50 atm and 1000 atm.
- There appears to be two pressure regions of interest, 50 - 100 atm and 1000 - 2000 atm.

We also discovered the presence of a gelatinous phase; the occurrence of boracite and this gel appears to be connected. The gel may not be present during growth but may form as a

Table 2. P-T Data on Ni-Br System (72 hour experiments).

Calculated Pressure (atm)	150°	200°	250°	300°	350°
5-10	No reaction.				
50	Single phase green gel formed.	Two phase green and white gel formed	Boracite crystallized by gel, 0.1 mm maximum transport evident.	> 95% yield well formed crystals. No green gel (white medium) some transport evident.	> 95% yield slightly rounded crystals. No gel retention, small amount transport evident.
100		Borate formed out of green gel - no boracite.	Boracite crystallized in bottom of ampoule ~100% yield 0.08 mm maximum.	< 20% yield of boracite in borate medium. No gel 0.05 mm maximum.	Boracite crystallized under two phase gel - no borate.
300-700			A few boracite crystals found in solid borate medium under gel < 5% yield 0.06 mm maximum.	High yield boracite crystallized in bottom region 0.06 mm maximum (shell of boracite formed).	
1000		Borate formed out of two phase gel - no boracite.	~40% yield boracite crystals under gel in borate medium 0.08 mm maximum.	Particles of boracite crystallized in upper yellow gel, larger particles as bottom clumps of crystals are approached 0.15 mm max.	Gel region more dense (white) suspended in water. Poor quality crystals.
1500				Small particles of boracite found in thin bubbly gel 1" above crystal/gel separation > 85% yield, 0.4 mm max., imperfect crystals.	
2000			Boracite crystals dispersed in upper green gel, get larger and darker as bottom clumps approached 0.2 mm max., Good crystals.		

result of the cooling process. There are indications that this phase is an essential part of the overall synthesis and crystal growth reaction mechanisms. Examination of growth runs which produced boracite show the gel region is located at different positions in the growth ampoule; the exact location appears to depend on pressure.

Figure 44a illustrates the typical appearance of a section of the boracite growth ampoule. The quartz rod in the center was used as a nucleation site for boracite. The dark spots on the rod are boracite crystals. In Figure 44b the typical layer formation common in all growth runs is observed. The larger crystals, formed at the bottom of the ampoule, are ~ 0.1 mm in size. The bulk of the matrix is a gel. Single crystals of Ni-Br boracite formed at all temperatures over 200°C. In addition to the boracite, two additional phases are observed, viz., nickel borate and the gel-like substance. The gel was identified by wet chemical analysis and found to consist of  $H_3BO_3$  suspended in a solution of  $NiBr_2$ . It was found that the largest, well formed crystals were produced at 300°C. Figure 45a shows a 25X enlargement of the quartz rod encrusted with gel, crystalline  $H_3BO_3$  and Ni-Br boracite crystals. Figure 45b illustrates a one of the largest Ni-Br boracite crystals grown ~ 0.5 mm on edge. The cube morphology is the only form typical of all boracites grown hydrothermally. Large amounts of boracite was always formed in these experiments and attempts to control the nucleation and thus the crystal size are described elsewhere in this report.

## (2) Analysis of Standard Hydrothermal Solution

The chemistry of boracite formation from hydrothermal solutions containing five components is of course extremely complex. However, an analysis of the solution pH did indicate a general trend for the reaction. The initial solution was prepared by adding 2.5 g of  $H_3BO_3$  to 40 ml of de-ionized  $H_2O$  (pH 4.1). This addition caused the pH of the  $H_2O$  to drop to 3.8 pH, solid  $H_3BO_3$  still being present (25°C). Then 0.546 g of  $NiBr_2$



(a) Typical section of quartz ampoule after growth.



(b) Typical layer formation with gel and Ni-Br boracite crystals (large crystals at bottom of layer -0.1 mm).

Figure 44. Hydrothermal boracite growth.



(a) Formation on quartz rod.



(b) Largest Ni-Br grown  $\approx 0.5$  mm.

Figure 45. Typical NiBr boracite crystals grown hydrothermally.

was slowly added and the solution color went from pale yellow to dark green. This indicates that hydrolysis of  $\text{Ni}^{+2}$  to  $\text{Ni}^{+}$  occurs. The pH was now 3.5. The addition of NaBr (0.257 g) resulted in no change of pH which indicates a buffered state. Both the NaBr and  $\text{NiBr}_2$  were completely in solution. Finally, 0.934 g of NiO was added and a pH 3.8 measured. Obviously some NiO is soluble in this solution via a Ni hydroxide formation. Using this pH value as a base, the results of reacting the solution at various temperatures are given in Table 3.

Table 3: Effect of Reaction Temperature on Solution pH.

<u>Reaction Temperature (72 hrs)</u>	<u>pH (25°C) <math>\pm</math> 0.1</u>
25°C	3.8
195°C	5.7
400°C	6.2

The increase in pH towards the basic side indicates that reaction products are formed during boracite synthesis which lead to an alkaline solution. Moreover, the boracite crystals formed at temperatures around 400°C appear to dissolve and exhibit poor crystal quality. The indication that boracite dissolved under alkaline conditions resulted in further experiments designed to grow boracite by the classical hydrothermal method (see 4.2.2(7)).

(3) Effects of Temperature/Pressure Variation and Component Loading sequence

Using the standard composition described above, the optimum temperature for growth of boracite was determined. Crystal growth runs were performed over the temperature range 200° to 500°C. Table 4 lists the experimental data. Crystallization of Ni-Br boracite appeared to be most favorable at 300°C. This agrees with the data described in Section 4.2.2(1). The effect of component loading sequence was examined and no difference in either the quantity of nucleation nor quality of boracite was

Table 4. Joubert-Type Experiments.

Run No.	T (°C)	P (psi)	Reactants	Reaction Time (days)	Fill (%)	Results
HJJ01-2	194	300	Standard	3	60	No boracite formed. Green "gel" plus light green borate present.
HJJ01-3	292	1,500	Standard	3	60	Boracite formed. Gel plus borate still present. Well formed crystals (cubes) - 0.05 - 0.10 mm on edge.
HJJ01-4	391	9,000	Standard	3	60	Boracite formed. Smaller amount of borate noted. Crystals seem flawed.
HJJ02-3	377	9,000	Standard	3	60	Loading sequence change produced no difference in boracite formed. Same size, same amount.
HJJ02-4	402	9,000	Standard	3	60	Change in loading sequence. No change in product. Crystals small-rounded-heavy inclusions. Appear to have grown rapidly.
HJJ03-2	501	19,500	Standard	3	60	Boracite formed. Poor quality crystals. Borate present.
HJJ03-4	409	9,000	Standard	3	60	Loading sequence change. No difference in crystal quality.
HJJ04-4	299	10,290	NiO Std. NiBr <sub>2</sub> = NaBr = H <sub>2</sub> O = H <sub>3</sub> BO <sub>3</sub> = 4X	3	80	Total amt. of boracite seems smaller. Well formed cubic crystals. No increase in size.
HJJ05-2	311	1,470	NaBr = 3X Remainder = Standard	3	70	Increase in mass transport.
HJJ05-3	295	10,290	NaBr = 10X Remainder = Standard	3	80	Large increase in mass transport. Boracite well formed. Increase in size to - 0.25 mm on edge.
HJJ05-4	288	1,470	NiBr <sub>2</sub> = 0X Remainder = Standard	3	60	Very little boracite formed. Small, well formed crystals.
HJJ06-3	288	1,470	NaBr = 20X Remainder = Standard	3	40	Large amount of boracite. Fine well formed crystals. No increase in size.
HJJ06-4	287	1,470	NiBr <sub>2</sub> = 5X Remainder = Standard	3	60	Increase in NiBr <sub>2</sub> seems to retard growth.
HJJ07-2	300	10,290	NiBr <sub>2</sub> = 0X NaBr = 3X Remainder = Standard	3	80	Decrease in yield of boracite.

Table 4. Joubert-Type Experiments. (Cont'd)

Run No.	T (°C)	P (psi)	Reactants	Reaction Time (days)	Fill (%)	Results
HJJ07-3	309	10,290	NiBr <sub>2</sub> = 0X NaBr = 10X Remainder = Standard	3	80	No boracite.
HJJ07-4	303	1,470	NiO = 0X Remainder = Standard	3	60	No boracite.
HJJ08-2	299	10,290	NiO = 3X Remainder = Standard	3	80	Boracite formed. No noticeable change in size or amount.
HJJ08-3	302	1,470	NiO = 2X NiBr <sub>2</sub> = 0X NaBr = 4X Remainder = Standard	3	70	Well formed crystals. No increase in transport. No increase in size. Final pH 8.0.
HJJ08-4	299	1,470	H <sub>2</sub> O = 2X Remainder = Standard	3	40	Boracite formed. No change.
HJJ09-2	315	30,000	H <sub>2</sub> O = 5X Remainder = Standard	3	90	Boracite formed with no noticeable change.
HJJ09-3	295	1,323	NiSO <sub>4</sub> ·6H <sub>2</sub> O subt. for NaBr Remainder = Standard	3	70	Boracite formed. Poor quality crystals.
HJJ10-2	301	10,584	K <sub>2</sub> CO <sub>3</sub> Subt. for NaBr Remainder = Standard	3	80	No boracite. Borate formation only.
HJJ10-3	298	10,584	Na <sub>2</sub> SO <sub>4</sub> Subt. for NaBr Remainder = Standard	3	80	Boracite formed. Crystals not well defined. Poor quality.
HJJ10-4	298	1,323	NH <sub>4</sub> Br Subt. for NaBr Remainder = Standard	3	70	Boracite formed. Fairly good mass transport. Poor quality crystals. Con- glomerate-wide range of sizes.
HJJ11-3	308	10,584	Ni(OH) <sub>2</sub> Subt. for NiO Remainder = Standard	3	80	Boracite formed. No change in quality or size.
HJJ12-2	304	1,323	HBr Subt. for H <sub>2</sub> O Remainder = Standard	3	70	Quality of boracite un- changed.
HJJ19-1	290	1,323	Standard	Slow Cool 24	60	No change in size or quality of boracite.

observed. In all cases, nickel borate and gel were formed along with the Ni-Br boracite crystals. The crystals grown in these experiments were essentially all the same size and shape (0.05 to 0.1 mm on edge). High temperature runs ( $> 400^{\circ}\text{C}$ ) produced crystals with rounded edges and were, generally, internally flawed. This result, coupled with the pH data (see 4.2.2(2)) clearly establishes an upper temperature limit for the growth of Ni-Br boracite.

#### (4) Variation of Stoichiometry

Attempts were made to increase the size of the boracite crystals by varying the amounts of selected components. When the concentration of  $\text{H}_3\text{BO}_3$  was increased there appeared to be a reduction in the total amount of boracite formed. The crystals were still well formed, but there was no increase in size. The complete removal of  $\text{NiBr}_2$  from the reaction did yield boracite, however the quantity was quite small. In addition, the increase in the amount of  $\text{NiBr}_2$  reduced the quantity and quality of the boracite crystals. When  $\text{NiBr}_2$  is removed from the reaction along with a simultaneous increase in NaBr concentration (to make up for the loss of Br), there is a decrease in boracite yield [compared to the standard run] and, ultimately, no yield at all (Table 4, run's HJJ07-2 and HJJ07-3). Similarly, if  $\text{NiBr}_2$  is removed and the NaBr and NiO concentrations are increased, an increase in mass transport is observed, but no change in crystal size. Complete elimination of NiO from the reaction yields no boracite, while an increase in NiO concentration produces no noticeable change from the standard runs. Increases in the concentration of NaBr were notable in that increases in mass transport and size were observed. The increase in transport was expected since NaBr acts as a mineralizer. The size increase was not dramatic (only  $\sim 0.25$  mm on an edge) but did indicate a possible increase in the solubility of a boracite intermediate or of boracite itself in the reaction medium. Finally, increases in water concentration were unable to produce any improvement in the previous results.

(5) Mineralizer Substitutions

Substitutes for the NaBr mineralizer were explored in hope of finding a more effective one. Four compounds were examined:  $\text{NiSO}_4$ ,  $\text{K}_2\text{CO}_3$ ,  $\text{Na}_2\text{SO}_4$  and  $\text{NH}_4\text{Br}$ . Boracite was formed in all but the  $\text{K}_2\text{CO}_3$  experiments. Rounded edges and flaws were characteristic of the crystals produced. No increases in size or yield were observed.

(6) Alternate Synthesis Methods

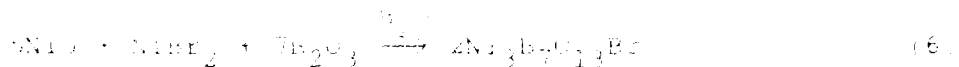
In an effort to produce large, high-quality crystals, several avenues were explored which constitute major modifications to the Joubert synthesis.

First, the effect of the rate of temperature change during cooling was explored. In every boracite producing experiment, all of the crystals are about the same in size - 0.10 to 0.25 mm on edge. This consistently small size indicates that crystallization occurs rapidly. It was not known whether the crystals formed immediately upon reaction or during the cooling of the bombs, a process which usually takes about 90 minutes. Experiments were conducted using a programmable temperature slope controller placed in series with the thermocouple circuit of the furnace. After 3 days at constant temperature ( $300^\circ\text{C}$ ) the furnace was programmed down to room temperature during a period of 21 days. The resulting crystals were the same size as before. This leads to the conclusion that the rapid crystallization is due to the extreme insolubility of boracite in the reaction medium during the formation stage.

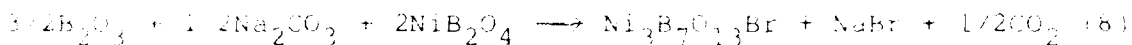
Second,  $\text{Ni}(\text{OH})_2$  was substituted for NiO in the reaction; The net result was boracite but no change from the standard. Third, HBr was used instead of  $\text{H}_2\text{O}$  as a solvent medium HBr; again, there was no noticeable improvement.

Finally, another series of experiments entailed the use of three new synthetic routes to the formation of the desired

compound. This method employed the use of different boron sources (as borates) which would hopefully produce a more stable environment for the formation of boracite crystals. The equations are as follows:



$2NiBr_2 + 7Na_2B_4O_7 + 20B_2O_3 \xrightarrow{1100^\circ C} 4Ni_3B_7O_{13}Br + 14NaBr + 20B_2O_3$   
and



The first two reactants in equation (8) actually react to form an intermediate, 1 mole of  $NaB_3O_5$ , which then reacts with the remaining components. The reaction conditions and results of these experiments are listed in Table 5. No observable improvement in the size or quality of the boracite produced was noted.

#### (7) Direct Dissolution (Classical Method)

The method for producing crystals appears to be limited by the fact that boracite crystallizes rapidly upon formation of the limited solution on the reactant medium. Therefore, the only way to produce a large, high quality crystal is to dissolve the reactants in a solvent, dilute the solution with an appropriate solvent and subsequent recrystallization in a cold zone via concentration and transport. The experimental conditions and results of these runs are given in Table 6. The solvents used can be divided into two groups: acidic and alkaline. As can be seen in Table 6, there was not noticeable difference in the results with either solvent group. In most cases the results were better than that of the classical method. Figure 4 illustrates the typical appearance of a high quality crystal before the final recrystallization experiment.

Table 5. Alternate Syntheses.

Run No.	T (°C)	P (psi)	Reactants	Reaction Time (days)	Yield (%)	Remarks
$\text{Reaction 1: } 3\text{Ni} + \text{Na}_2\text{B}_4\text{O}_{10} + \text{H}_2\text{O} \rightarrow 2\text{Ni}_3\text{B}_7\text{O}_{13}\text{Br}$						
HJ11-2	324	1,325	Ni = 0.47 g NiBr <sub>2</sub> = 2.11 g Na <sub>2</sub> B <sub>4</sub> O <sub>10</sub> = 1.22 g H <sub>2</sub> O = 2 cc	3	70	Boracite formed. Same size and quality as in standard runs.
$\text{Reaction 2: } 12\text{NiBr}_2 + \text{Na}_2\text{B}_4\text{O}_{10} + 3\text{H}_2\text{O} \rightarrow 4\text{Ni}_3\text{B}_7\text{O}_{13}\text{Br} + 14\text{NiBr} + 6\text{Ni}$						
HJ11-4	310	10,584	Na <sub>2</sub> B <sub>4</sub> O <sub>10</sub> = 1.9 g NiBr <sub>2</sub> = 2.2 g H <sub>2</sub> O = 3.0 g	3	80	Very little boracite formed. Mostly borax. Crystal small - 0.1 mm.
HJ11-4	343	1,171	Na <sub>2</sub> B <sub>4</sub> O <sub>10</sub> = 1.9 g NiBr <sub>2</sub> + 3H <sub>2</sub> O = 2.6 g H <sub>2</sub> O = 1 g	3	60	More boracite than HJ11-4. Increase in mass transport. No increase in size or quality.
$\text{Reaction 3: } \frac{3}{2}\text{H}_2 + \frac{1}{2}\text{Na}_2\text{B}_4\text{O}_{10} + 2\text{NiB}_2\text{O}_4 + \text{NiBr}_2 \rightarrow \text{Ni}_3\text{B}_7\text{O}_{13}\text{Br} + \text{NaBr} + \frac{1}{2}\text{H}_2$						
HJ13-2	160	147	NiBr <sub>2</sub> = 0.438 g NiB <sub>2</sub> O <sub>4</sub> = 0.589 g H <sub>2</sub> = 0.210 g Na <sub>2</sub> B <sub>4</sub> O <sub>10</sub> = 0.106 g H <sub>2</sub> O = 2 cc	3	40	No boracite.
HJ13-3	246	735	Same	3	40	No boracite.
HJ13-4	423	1,470	Same	3	47	Boracite formed. No trace in the small crystals - 0.1 mm.
HJ14-1	464	6,376	Same	3	40	Less boracite produced than HJ13-4.
HJ14-4	723	21,721	Same	3	40	Very small amount of boracite formed (same as HJ14-1). Poorly formed crystals.
HJ15-1	152	117	NiBr <sub>2</sub> = 1.409 g NiB <sub>2</sub> O <sub>4</sub> = 1.110 g H <sub>2</sub> = 0.410 g Na <sub>2</sub> B <sub>4</sub> O <sub>10</sub> = 0.106 g 49% HF <sub>2</sub> = 2 cc	3	40	No boracite.
HJ15-2	250	735	Same	3	40	No boracite.
HJ15-3	423	1,470	Same	3	40	No boracite.
HJ17-4	501	6,376	Same	3	40	No boracite.

Table 6. Direct Dissolution.

Run No.	T (°C)	P (psi)	Solvent	Reaction Time (days)	Fill (%)	Results
HJJ18-1	190	147	49% HBr	2	20	pH = 0. Total decomposition.
HJJ19-2	202	147	B <sub>2</sub> O <sub>3</sub> Wt% = 79 H <sub>2</sub> O Wt% = 21	3	40	No reaction.
HJJ19-3	202	147	NaOH + HBr = pH 4	3	50	Partial decomposition.
HJJ19-4	218	147	NiBr <sub>2</sub> Wt% = 49 KBr Wt% = 27 H <sub>2</sub> O Wt% = 24	3	25	No reaction.
HJJ21-2	200	147	H <sub>2</sub> O saturated with NiBr <sub>2</sub> at 25°C pH = 0.5	3	50	No reaction.
HJJ21-3	202	147	H <sub>2</sub> O saturated with Na <sub>2</sub> SO <sub>4</sub> at 25°C + 4 50% HBr pH = 2	3	50	Total decomposition.
HJJ21-4	204	147	1 m NaOH + 50% H <sub>2</sub> SO <sub>4</sub> pH = 2	3	50	Total decomposition.
HJJ22-1	200	147	1 m NiBr <sub>2</sub> in H <sub>2</sub> O <sub>2</sub> (30%)	5	50	Partial decomposition.
HJJ22-3	200	147	1 m Na <sub>2</sub> SO <sub>4</sub> in H <sub>2</sub> O <sub>2</sub> (30%)	5	50	No reaction.
HJJ22-4	198	147	H <sub>2</sub> O <sub>2</sub> (30%)	5	50	No reaction.
HJJ23-1	203	147	H <sub>2</sub> BO <sub>3</sub> Wt% = 12 Na <sub>2</sub> SO <sub>4</sub> Wt% = 28 H <sub>2</sub> O Wt% = 60	2	50	Total decomposition.
HJJ23-2	200	147	Same	2	50	Total decomposition.
HJJ23-3	202	147	H <sub>2</sub> BO <sub>3</sub> Wt% = 56 HBr Wt% = 44	2	50	Total decomposition.
HJJ24-1	200	147	5 m NH <sub>4</sub> Br in H <sub>2</sub> O	2	50	Total decomposition.

Table 6. Direct Dissolution. (Cont'd)

Run No.	T (°C)	P (psi)	Solvent	Reaction Time (days)	Fill (%)	Results
HJJ24-2	192	147	5 m NaBr	2	50	Partial decomposition.
HJJ24-3	201	147	Dimethyl- sulfoxide	2	50	Total decomposition.
HJJ25-1	192	147	6 m NaOH	3	50	pH $\approx$ 8 Partial decomposition.
HJJ25-2	186	147	6 m NH <sub>4</sub> OH	3	50	pH $\approx$ 9 Total decomposition.
HJJ26-2	292	1,323	1 m Borax in H <sub>2</sub> O	3	50	pH $\approx$ 9 Partial decomposition.
HJJ26-4	485	13,230	1 m Borax in H <sub>2</sub> O	3	50	pH $\approx$ 9 Total decomposition.
HJJ27-1	383	5,733	1 m Borax in H <sub>2</sub> O with 4 Wt% NaBr	2	50	pH $\approx$ 8 Total decomposition.
HJJ27-3	400	29,400	3 m Borax in H <sub>2</sub> O with 4 Wt% NaBr	2	90	pH $\approx$ 8 Partial decomposition.

In addition to the solvents investigated and described above, pure H<sub>2</sub>O and solutions of H<sub>3</sub>BO<sub>3</sub> were also examined as solvents. Tables 7 and 8 list the experimental data. For both solvent systems the results were the same: the original Ni-Br boracite crystal retained its external morphology but decomposition (green color see Fig. 46) was evident. Chemical analysis of the solvent after reaction indicated the presence of Br. This coupled with the low pH observed indicates that the boracite decomposes by giving up Br and that the resultant green color is due to the formation of nickel borate. Within the range of solvents investigated, no suitable media for boracite dissolution was found.

Table 7. Solubility of Ni-Br Boracite in H<sub>2</sub>O

Temperature	% Fill	Pressure (atm)	pH (25°C)	
			Initial	Final
350°C	60	200	5.8	2.7
450°C	60	1000	5.8	2.4

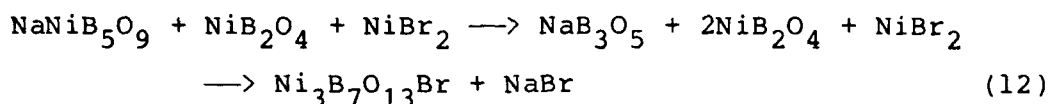
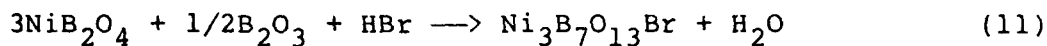
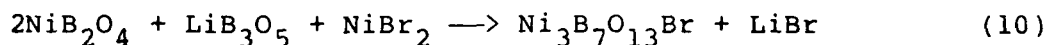
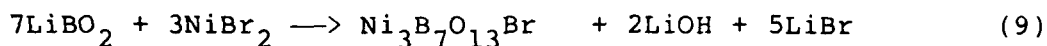
Table 8. Solubility of Boracite in H<sub>2</sub>O-H<sub>3</sub>BO<sub>3</sub>

Temperature	% Fill	Molality	Pressure (atm)	pH (25°C)	
				Initial	Final
340°C	75	0.01	1000	5.4	2.5
340°C	57	0.1	150	4.6	3.0
320°C	77	0.4	800	4.0	2.5
320°C	68	0.8	300	3.2	2.3

#### 4.2.3 Hydrothermal Growth in Basic Media

An alternative method of hydrothermal boracite crystal growth investigated was growth from aqueous solutions mineralized with alkali halides. This approach was motivated by the observation that the natural minerals MgCl, MnCl and FeCl boracite were formed during the evaporation of alkali-rich sea basins. Results showed that the higher the concentration of alkali

halide the greater the yield of boracite powder. These experiments were run using gold ampoules, since the alkali ions severely attack quartz under the pressure and temperature conditions utilized. The following equations summarize the components and reactions used in these experiments.



All of the above reactions were run in high purity  $\text{H}_2\text{O}$  (> 7 megohm). The reactions were performed over a wide range of pressures (1 Kpsi - 45 Kpsi), temperatures (300-750°C) and times (1-10 days). In all cases, very high yields of boracite powder were formed (> 95%); however, no appreciable crystallization was observed.

It is evident that the kinetics of these reactions is extremely rapid. In order to obtain useable single crystals, a method of reducing and controlling the reaction rates is required. Experiments were carried out on Reaction (12) in an effort to slow the reaction rate and thus make possible the growth of large crystals. However, only boracite powder was obtained in addition to a number of other unidentified phases.



(a) Before (10X).



(b) After (8X)

Figure 46. Typical decomposition of Ni-Rr boracite crystals during solubility experiment.

### 4.3 Vapor Transport Growth of Boracite Crystals

A novel three-zone vapor transport technique was developed for the growth of boracite. Large single crystals (> 10 mm on edge) of NiBr boracite were produced. Methods were developed to control nucleation and eliminate cracking of crystals during growth. Experimentation was begun on the growth of MnI boracite and mixed crystals of NiBrCl and FeMnI boracite using this technique.

#### 4.3.1 Apparatus

While preliminary experimentation was done using a horizontal two-zone furnace, our preliminary growth system was a three-zone furnace. This three-zone vapor transport technique is a modification of the boracite growth method described by Bugakov et al. (Ref. 24). The growth system consists of a horizontal 116 cm three zone furnace. Each zone is independently heated by a Eurotherm digital temperature controller with phase angle SCR. The controllers are remotely programmed by a three channel Honeywell DCP-7700 digital control programmer. This system is capable of generating and executing complex temperature/time programs with ramp rates over the range 1°/hr to 1000°C/hr. Thus, heat-up, equilibration, establishment of temperature gradients, and cool down are controlled automatically. The temperature stability of each zone is better than  $\pm 1^\circ\text{C}$ . The crystal growth furnace and a typical temperature gradient across the three zones are shown schematically in Figure 47. The overall temperature program for a typical crystal growth run is shown in Figure 48. The establishment of the final  $\Delta T$  was varied from a few minutes to about 20 hours, with an equilibration time of approximately 30 minutes being ideal. In order to reduce the large amount of nucleation observed in the growth of the boracites, a temperature gradient was established as shown in Figure 49. Theoretically, the oscillation in temperature will permit selective growth of only a few nucleation centers (i.e., those larger than critical radius). However, the use of this technique was not completely successful.

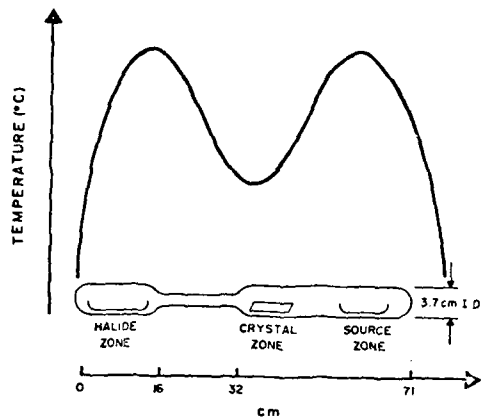


Figure 47. Temperature gradient in three zone furnace.

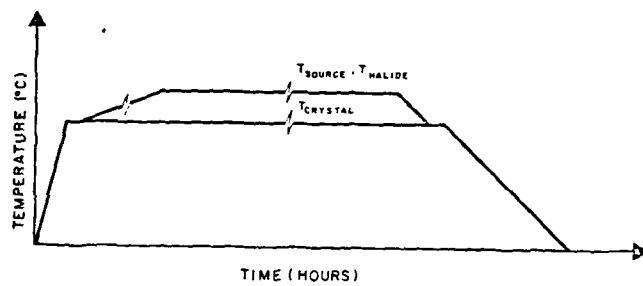


Figure 48. Typical temperature vs. time program for three zone vapor transport furnace.

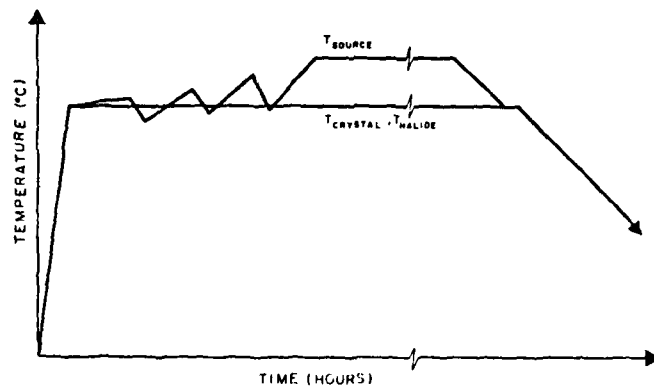
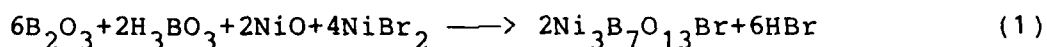


Figure 49. Oscillation method for gradient formation.

The main growth chamber consisted of a quartz reaction tube (50 mm O.D.) which contained two quartz boats. One boat contained the metal halide, while the second contained the B<sub>2</sub>O<sub>3</sub>, NiO and H<sub>3</sub>BO<sub>3</sub> sources. The tube was sealed under vacuum prior to placement in the furnace. Typical reaction tube volumes ranged from 500 to 1000 cm<sup>3</sup>.

#### 4.3.2 Transport Reactions

The basic transport reaction used for boracite growth is:



An analysis of previous data on the vapor transport growth of boracite indicates the active specie for transport was HBO<sub>2</sub> (Refs. 25,26) This compound is formed by the reaction of H<sub>2</sub>O and B<sub>2</sub>O<sub>3</sub>:



The source for water in the growth system is supplied via the thermal decomposition of boric acid as follows:



The concentration of water was typically fixed at 0.8 mg/cm<sup>3</sup>, which corresponded to a maximum in the transport rate of boracite (Ref. 24).

#### 4.3.3 Experimental

The high purity (>99.9%) starting components, B<sub>2</sub>O<sub>3</sub>, NiO, NiBr<sub>2</sub> and H<sub>3</sub>BO<sub>3</sub> were pre-dried under vacuum at temperatures between 100° to 400°C. The components were weighed and loaded into the growth chamber in a dry box enclosure under an argon atmosphere. The growth chamber was then sealed under vacuum. Typical component weights used were:

B <sub>2</sub> O <sub>3</sub>	8.3 g	NiO	2.5 g
NiBr <sub>2</sub>	14.9 g	H <sub>3</sub> BO <sub>3</sub>	1.7 g

The source zone contained  $B_2O_3$ , NiO and  $H_3BO_3$  in one quartz boat. The halide zone contained the  $NiBr_2$  in another quartz boat.

The sealed growth tube was then inserted into the cold three-zone furnace which was then heated to  $800^\circ C$  at  $20^\circ \text{ min.}^{-1}$  and allowed to reach thermal equilibrium ( $\sim 20$  minutes). Typically, the source and halide zones were then heated at  $10^\circ \text{ min.}^{-1}$  to  $900^\circ C$ , which established a  $\Delta T = 100^\circ C$ . The total growth time ranged from 76 to 140 hours. At the conclusion of the run, the zones were cooled simultaneously at an average rate of  $2^\circ \text{ min.}^{-1}$  to room temperature. A number of modified heating and cooling rates were examined in order to evaluate vapor supersaturation and thermal effects on crystal cracking. However, the conditions outlined above are those which were experimentally determined to yield large ( $> 10$  mm) crystals of  $Ni_3B_7O_{13}Br$ .

#### 4.3.4 Results

Tables 9 and 10 contain the crystal growth data for growth runs of  $Ni_3B_7O_{13}Br$  and  $Mn_3B_7O_{13}I$ . In addition small crystals of  $Mn_{1.5}Fe_{1.5}B_7O_{13}I$  and  $Ni_3B_7O_{13}Br_{0.5}Cl_{0.5}$  were grown under similar conditions. The placement of the boron and halide sources, as shown in Figure 47 were critical for the growth of large boracite crystals. In initially experiments with a two-zone furnace, the two sources were placed together in one section of the tube and all growth occurred at the cool end of the chamber. This resulted in an enormous amount of spontaneous nucleation. Using the three-zone furnace in the configuration shown in Figure 47, reduced nucleation substantially; however, the level of supersaturation required to grow only a few large crystals has been difficult to achieve. Figure 50 illustrates the  $Ni_3B_7O_{13}Br$  crystals typically obtained with the three zone furnace system and Figure 51 shows a number of other boracites grown with the same system.

Table 9. Crystal Growth Data for  $\text{Ni}_3\text{B}_7\text{O}_{13}\cdot\text{Br}$

Run No.	Tube Volume $\text{cm}^3$	Component Concentrate (g)				$\text{H}_2\text{O}$ $\text{mg}/\text{cm}^3$	Temperature ( $^{\circ}\text{C}$ ) Zone, Source	Crystal	Time Hr.	Transport Rate $\text{mg}/\text{hr.}$	REMARKS
		$\text{B}_2\text{O}_3$	$\text{NiBr}_2$	$\text{NiO}$	$\text{H}_3\text{BO}_3$						
GL-2	1000	24.35	43.7	7.45	0	0	803	699	48	0	No boracite.
GL-3	1150	8.3	14.8	2.5	2.1	-	798	675	76	-	Small crystals, boracite.
GL-6	840	8.3	14.9	2.5	1.5	0.8	926	842	144	50	Boracite, 2 forms.
GL-7	1104	8.3	14.9	2.5	2.02	0.8	899	792	144	30	Pyramids, cracked, poly.
GL-8	1107	8.3	14.9	2.5	2.03	0.8	899	484	72	0	No boracite.
GL-9	1107	8.3	14.9	2.5	2.03	0.8	899	791	119	11	Small crystals (many).
GL-10	1040	7.5	13.5	2.3	2.4	0.8	899	795	114	4	Few, large crystals.
GL-11	880	8.3	14.9	2.5	1.63	0.8	897	797	140	-	Few, small crystals.
GL-12	730	8.3	14.9	2.5	1.34	0.8	897	797	137	33	Four large crystals.
GL-13	790	$\text{Li}_2\text{B}_4\text{O}_7$ (5.83)	9.8	1.1	$\text{H}_2\text{O}$ (0.7)	0.9	899	796	135	-	Tube exploded.
GL-14	570	8.3	14.9	2.5	1.75	0.8	897	796	118	-	Seeded; many crystals.
JJ-01	564	8.3	14.9	2.5	1.03	0.8	897	786	144	-	Many small crystals.
JJ-02	601	8.15	14.9	2.5	1.10	0.8	897	796	192	15	Many small crystals.
JJ-03	647	8.15	14.9	2.5	1.19	0.8	897	796	120	22	Large crystals (many).

- Not measured.

Table 10. Crystal Growth Data for  $Mn_3B_7O_{13}$ .I

Condition	Run Number									
	LP-03	LP-04	LP-05	LP-06	LP-07	LP-08	LP-09	LP-10		
$MnI_2 \cdot 4H_2O$ (g)	3.8	3.8	3.8	-	-	-	-	-	3.8	
Anhydrous $MnI_2$ (g)	-	-	-	21.0	21.0	21.0	21.0	21.0	-	-
$I_2$ (g)	18.0	18.0	2.0	-	8.0	-	-	-	18.0	
Metallic Mn (g)	1.8	1.8	-	-	-	-	-	-	1.8	
MnO (g)	-	-	2.34	2.34	2.34	2.34	2.34	2.34	-	
$B_2O_3$ (g)	8.3	8.3	24.0	8.3	24.0	24.0	24.0	24.0	24.0	
$H_3BO_3$ (g)	-	-	-	1.10	1.05	1.0	1.2	1.2	-	
AT (°C)	100	150	150	150	100	100	100	100	150	
T Limits (°C)	850,750	800,650	800,650	800,650	700,600	800,700	900,800	800,650	800,650	
Total Time at AT (Hr.)	95	100	100	80	-	-	60	280		
Substrate	none	Pt	Pt	Pt	Pt	none	none	Pt		
Results:	Small boracite on surface of tube.	1 mm size boracites nucleated on Pt.	Many small needle-like crystals nucleated on Pt.	No boracite.	No boracite. Tube exploded upon heating.	No boracite. program interrupted.	No boracite.	No boracite. intergrown crystals on Pt.	Small intergrown crystals on Pt.	

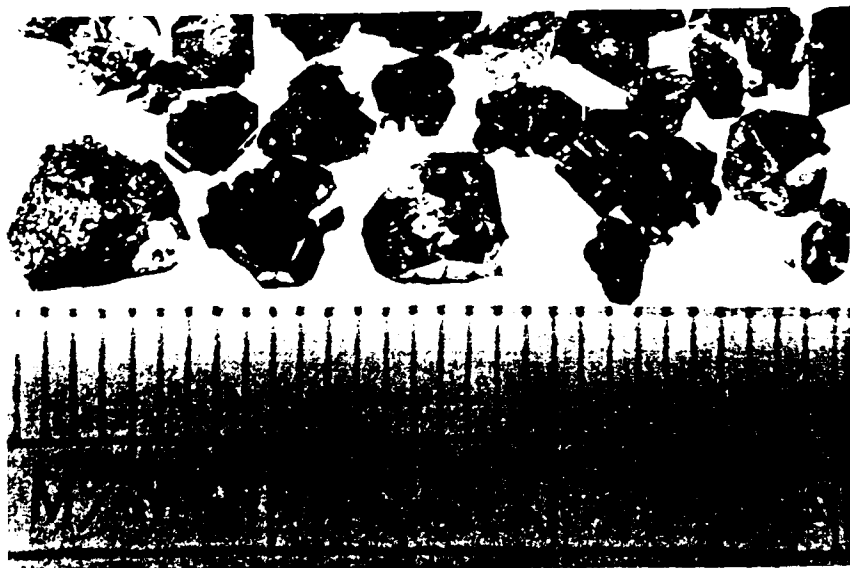
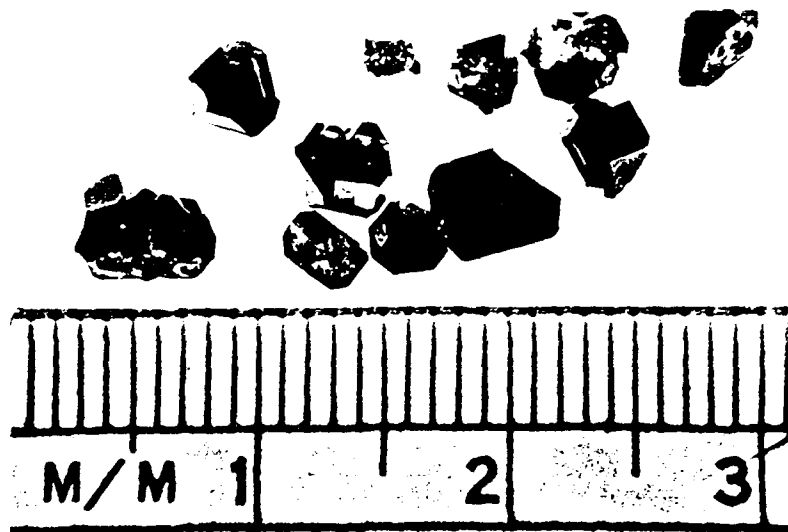


Figure 50. Nitr boracite crystals grown using a three-zone vapor transport technique.

AD-A092 566

PHILIPS LABS BRIARCLIFF MANOR NY  
OPTIMIZED PYROELECTRIC VIDICON THERMAL IMAGER. VOLUME II. IMPRO--ETC(U)  
SEP 80 W A SMITH, G LOIACONO, A SHAULOV

F/G 17/5

DAA653-76-C-0053

UNCLASSIFIED

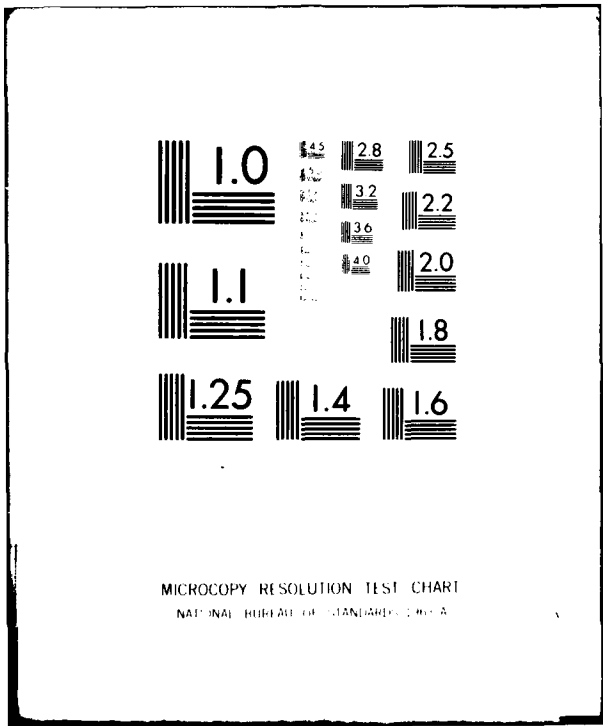
NL

2 of 2

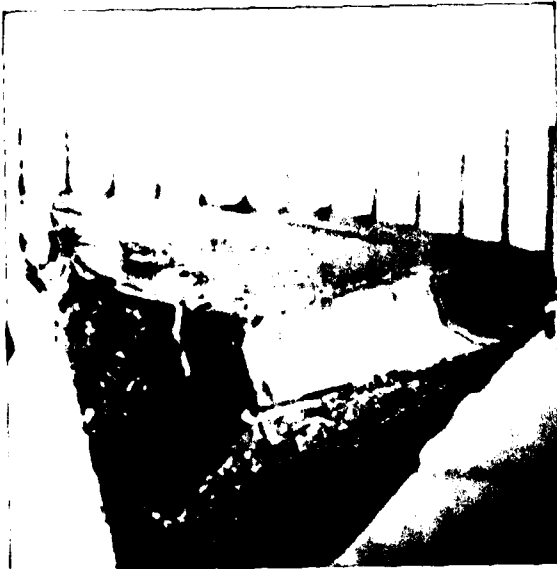
AD-A092 566



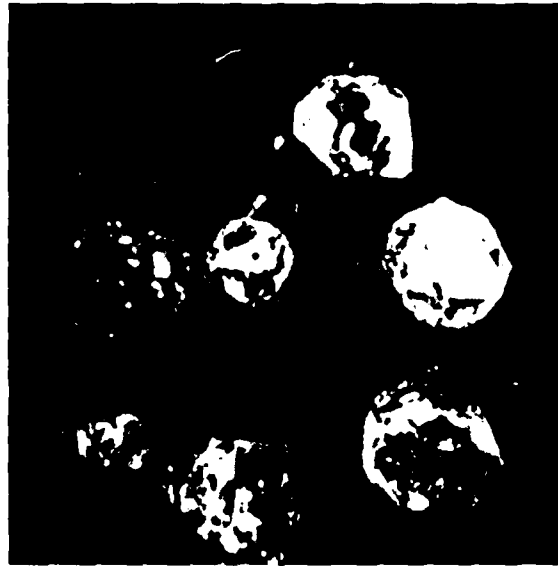
END  
DATE  
FILMED  
1981  
DTIC



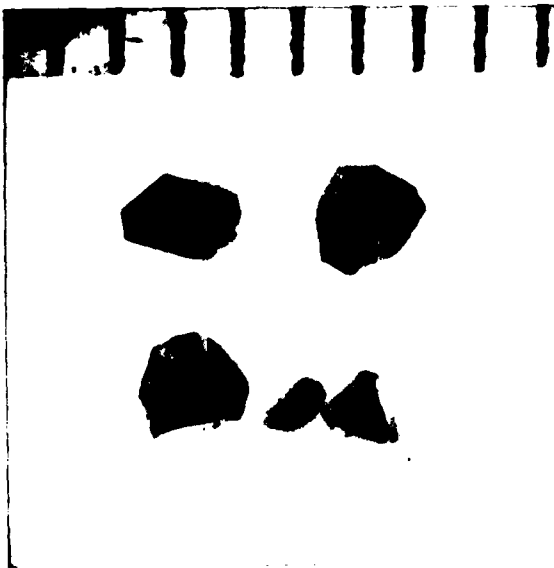
MICROCOPY RESOLUTION TEST CHART  
NATIONAL BUREAU OF STANDARDS-1963-A



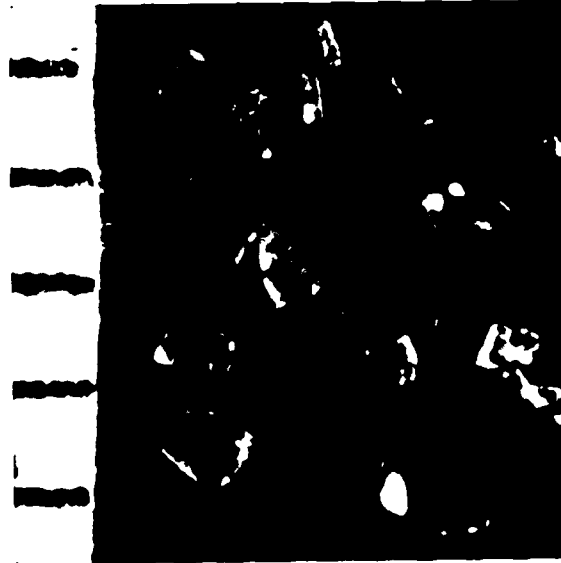
LP 02A (mm scale)  
 $\text{NiBr}_{.5}\text{Cl}_{.5}$



LP 03A  
MnFeI Boracite



LP 02 (mm scale)  
NiBr Boracite



LP 04 (mm scale)  
MnI Boracite

Figure 51. Other boracite crystals grown by vapor transport.

Table 10 summarizes the growth data for  $Mn_3B_7O_{13}I$  boracite. A series of eight runs were made to study the crystallization of this boracite in the three zone furnace. Since anhydrous  $MnI_2$  and  $MnO$  were not available initially, these zones were loaded with metallic  $Mn$ ,  $B_2O_3$ ,  $MnI_2 \cdot 4H_2O$  and  $I_2$ . These growth conditions produced the best results for this series of experiments. Single crystals were obtained in three morphologies: pale pink cubic, pale pink orthorhombic and pink cubic. X-ray precession photographs identified the lattice constant of the pale pink cubic crystals as  $12.313 \pm .06$  Å, which agreed with  $12.32 \pm 0.03$  Å reported by Schmid (Ref. 17). It is interesting to note that no  $Mn_3B_7O_{13}I$  crystals were obtained using the standard stoichiometry.

Mixed crystals of  $Ni_3B_7O_{13}Br_{0.5}Cl_{0.5}$  boracite were grown approximately 10 mm in size. However, these crystals had a number of penetration twins which were intergrown. Small crystals (2-3 mm) of  $Fe_{1.5}Mn_{1.5}B_7O_{13}I$  were grown. These crystals did not have penetration twins, but were rounded and coated with a brown surface film. The film was soluble in dilute HCl. The growth process of both of these materials were subject to violent explosions during the cool down cycle.

During the vapor growth of boracite a large amount of spontaneous nucleation occurs at the beginning of the process. The cause of this nucleation is a rapid, uncontrolled build up of supersaturation of the boracite vapor species. Because of this effect none of the seeded growth runs were successful. However, the nucleation of only a few growth centers (4 to 6) was achieved by the rapid establishment of the final growth thermal gradient. If this gradient is established in less than 10 minutes, the total amount of boracite nucleated is limited; this favors the growth of large crystals.

The conditions required for the growth of crystals of  $\text{Ni}_3\text{B}_7\text{O}_{13}\text{Br}$  boracite as described above, produced large crystals consistently; however, they were always cracked. Obviously this cracking problem must be eliminated in order to obtain large high quality crystals for pyroelectric measurements. There were two possible causes for this mechanical failure, viz., cooling of the furnace was excessive or the crystals were interacting with a thin film (formed in the growth process) which resulted in cracking.

The first mechanism was investigated by reducing the cooling rate of the furnace (after growth) from  $180^\circ\text{C/hr}$  down to  $4^\circ\text{C/hr}$ . The crystals produced still contained cracks. Thus, internal strains in the crystals, which might develop during rapid cooling, do not appear to be significant. The possibility that the cracking was caused by the ferroelectric phase transition was also eliminated because uncracked crystals do not develop cracks when thermally cycled through the transition at rates of about  $50^\circ\text{C/hr}$ . The last potential source of cracking was the thin film present in the growth zone after the growth cycle is completed. This film has been observed in all growth runs and is formed when the growth chamber is exposed to humidity in the atmosphere. The film which is initially transparent ( $\sim 0.1$  mm thick) turns into a white solid when exposed to water. X-ray diffraction studies coupled with X-ray fluorescence analysis clearly shows the major components to be  $\text{H}_3\text{BO}_3$ ,  $\text{HBO}_2$  and  $\text{H}_6\text{B}_2\text{O}_6$  (Table 11). There was no evidence that the film was composed of a borosilicate glass, since silicon was not detected in this material by X-ray fluorescence. Therefore, the products determined by X-ray analysis would imply the film (initially) is composed of  $(\text{HBO}_2)_n$ , where  $n = 1, 2$ , etc. The following reactions can be assumed,



Table 11. Analysis of Vapor Transport Phases in Growth of  $\text{Ni}_3\text{B}_7\text{O}_{13}\text{Br}$ .

<u>Compound</u>	<u>Film (Fast)</u>	<u>Film (Slow)</u>	<u>Green Powder</u>	<u>Crystals NiBr<sub>2</sub> Zone</u>
$\text{H}_3\text{BO}_3$	Maj	Maj	0	0
$\text{HBO}_2$	Maj	Maj	0	0
$\text{H}_6\text{B}_2\text{O}_6$	Maj	Maj	0	0
$\text{B}_2\text{O}_3$	?	Min	0	0
$\text{NiBr}_2$	Min	Min	0	0
$\text{Ni}_3\text{B}_2\text{O}_6$	Min	0	Maj	Maj
$\text{Ni}_3(\text{BO}_3)_2$	?	0	Maj	Maj
B	?	0	0	0
NiO	0	0	Trace	0
$\text{Ni}_2\text{SiO}_4$	0	0	0	Maj

Figure 52 illustrates the relationship between the quartz chamber wall, the film and the grown crystal. The cracks in the crystals are evident and originate at the crystal/film interface. Figure 53 is an enlargement of the central region of Figure 52. A large number of crystallites can be observed between the white film and the bulk crystal. These multiple nucleation sites coupled with the differential thermal expansion between the film-crystal-quartz can easily cause mechanical failure of the grown crystal. Furthermore, even very small cooling rates will not eliminate cracking with this complex material configuration.

A number of experiments were designed to determine when the film was formed and how to prevent (if possible) the formation. It is clearly seen in Figures 52 and 53 that the boracite initially crystallizes on top of the film. Thus, the film already exists before the supersaturation required for boracite formation is attained. We have previously determined that  $\text{HBO}_2$  is the major component in the formation and growth of boracite; thus elimination of this component is not feasible. However, technical discussions on boracite growth with the Plessey Company revealed the possibility of nucleating boracite on suitable substrates - in particular platinum foil (Ref. 27). Two growth runs were performed using platinum foil under conditions identical with those that yielded large boracite crystals. Figure 54 illustrates a section of the platinum foil upon which the crystals nucleated. The white irregular shaped areas are the points where boracite nucleated and subsequently grew. The grown crystals do not adhere to the foil. In addition, there is no evidence of the thin film formed during the standard growth runs. Figure 55 shows a typical  $\text{Ni}_3\text{B}_7\text{O}_{13}\text{Br}$  crystal cluster. The crystals are about 3-4 mm in diameter and are uncracked. In both experiments, all nucleation and growth occurred on the platinum foil with no boracite being nucleated on the wall of the quartz growth chamber.



Figure 52.  $\text{Ni}_3\text{B}_7\text{O}_{13}\text{Br}$   
crystal attached to wall  
of quartz chamber.



Figure 53. Multiple nucle-  
ation of  $\text{Ni}_3\text{B}_7\text{O}_{13}\text{Br}$  on film.

PRECEDING PAGE BLANK-NOT FILMED



Figure 54. Nucleation sites for boracite on platinum foil.



Figure 55. Typical cluster of boracite nucleated on platinum foil.

Table 11 also lists the results of X-ray analysis of two other crystalline phases usually observed in the vapor growth of  $\text{Ni}_3\text{B}_7\text{O}_{13}\text{Br}$ . The phases were identified as  $\text{Ni}_3(\text{BO}_3)_2$  and  $\text{Ni}_2\text{SiO}_4$ . The silicon required to form this latter compound probably comes from the quartz boat used to contain the  $\text{B}_2\text{O}_3$ ,  $\text{H}_3\text{BO}_3$  and  $\text{NiO}$ . This boat is severely attacked during the growth process.

## 5. PROPIONATE CRYSTAL GROWTH

A technique was developed, for the solution growth of large single crystal of dicalcium lead propionate (DLP)  $\text{Ca}_2\text{Pb}(\text{C}_2\text{H}_5\text{COO})_6$  and dicalcium strontium propionate (DSP)  $\text{Ca}_2\text{Sr}(\text{C}_2\text{H}_5\text{COO})_6$ .

Efforts to grow mixed DLP-DSP crystals by the same technique were impeded by a lack of information on the temperature dependence of the phase diagram for the mixed system.

Exploration of the molecular engineering possibilities in the propionate family was begun by the growth of materials with other organic acid radicals substituted for propionic acid radical. Several new material were obtained; acrylic acid doped DLP formed the best quality crystals.

Appendix B contains a summary of X-ray studies of propionates performed at Oxford University. These results provide direct confirmation of our working hypothesis that the ferroelectric properties of the propionates can be tuned by partial substitution of other organic acid radicals for the propionic acid radical.

### 5.1 Dicalcium Lead Propionate and Dicalcium Strontium Propionate

Large single crystals of dicalcium lead propionate (DLP),  $\text{Ca}_2\text{Pb}(\text{C}_2\text{H}_5\text{CO}_2)_6$ , and dicalcium strontium propionate (DSP)  $\text{Ca}_2\text{Sr}(\text{C}_2\text{H}_5\text{CO}_2)_6$  were grown using the solution crystal growth technique. The growth took place in modified Holden-type crystallizers (Fig. 56) consisting of two-liter Pyrex growth chambers, Lexan seed holders and rotator covers, 30-liter water baths with stirrers, and variable-speed, seed-holder rotation motors. Initially, the seed holders and rotator covers were constructed from Lucite. Once it was noticed that the propionate solutions attacked the Lucite parts, we replaced them with Lexan which was found to be stable under the present growth conditions. The bath temperatures, in all cases, were stable to  $\pm 0.005^\circ\text{C}$ .

Crystals of DLP and DSP were grown from saturated solutions by slow heating from  $40^\circ\text{C}$  to  $\sim 50^\circ\text{C}$ . The results of these runs are



Figure 56. Propionate crystals during growth.

found in Table 12. The raw material used for growing DLP and DSP was synthesized by mixing aqueous solutions of calcium propionate and lead (or strontium) propionate using a mole ratio of

Table 12. Propionate Growth Runs.

<u>Crystal</u>	<u>Growth Intervals</u> (°C)	$\frac{\Delta T}{}$ (°C)	<u>Avg.</u> $\frac{\Delta T}{\text{Day}}$ (°C)	<u>Avg. Growth</u> <u>Rate [001]/Day</u> (mm)
DSP	40 025° → 50 780°	10 755°	0.123	0.20
DSP	40 960° → 43 770°	2 810°	0.094	0.19
DSP	41 095° → 47 500°	6 405°	0.131	0.10
DLP	41 340° → 45 260°	3 920°	0.085	0.10
DLP	42 445° → 50 000°	7 555°	0.157	0.10
DLP	41 000° → 50 092°	9 090°	0.118	0.23

2:1, Ca:Pb (or :Sr). A water and propionic acid solvent system was used with a volume ratio of 95:5. Seeds of the material to be grown were glued onto Lexan seed holders at a radial distance of 4 cm. Each seed was ~ 5 x 5 x 5 mm in size and they were oriented along the tetragonal C axis whenever possible. The flow velocity of solution across the seeds was calculated to be ~ 20 cm/s. Typically, the growth runs lasted 40-60 days. During that period the average heating and growth rates were 0.1°C/day and 0.1 mm/day, respectively. After an initial capping period, the crystals grew clear to heights ranging from 10 to 20 mm each. Figure 57 shows two DLP crystals after removal from the seed holder. All runs contained varying amounts of spurious nucleation which formed on the walls of the glass container and the seed holder.

In general, it has been found that good quality crystals of DSP are more difficult to obtain than those of DLP. The main problem in the growth of DSP is the long period of time required to initiate growth. When growth begins, however, a large amount of spurious nucleation deposits in the growth chamber. The degree of supersaturation required for growth seems higher for DSP. Since the solubility curves of DLP and DSP are nearly

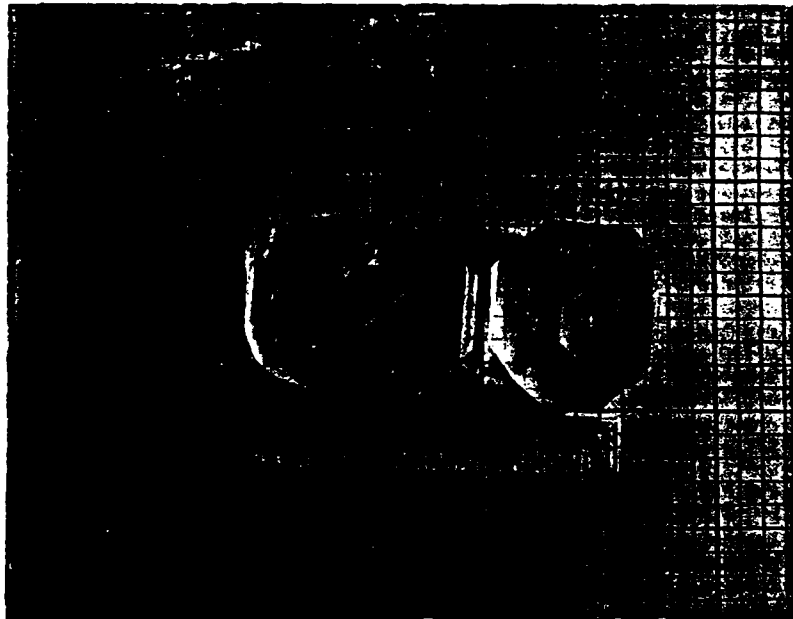


Figure 57. DLP crystals after removal from solution.

identical, there must be some other factor controlling the rate determining step in the growth mechanism of DSP. The available information indicates that the meta-stable region for DSP is very narrow. Therefore the rate of supersaturation is critical and is subject to stricter control than that of DLP.

#### 5.2 DLP-DSP Mixed Crystals

Two crystals were grown from a solution with a composition, 50% DLP - 50% DSP. However, a chemical analysis of these crystals yielded the following molar ratios:

$$\begin{array}{l} \text{Ca : Pb} \quad : \text{Sr} \\ 2 : 0.998 : 0.002 \end{array}$$

It is obvious that very little Sr was incorporated into the crystals. Further analyses conducted on the solid starting materials used to prepare the actual growth solution yielded results which indicated wide variations in the Pb:Sr stoichio-

metry. There is little information available in the literature on the phase diagram of the DLP-DSP system, (Ref. 28) and no information on the temperature dependence of the phase diagram.

Mixed crystals have been grown which were true DLP-DSP solid solutions (Ref. 28). An investigation of the phase diagram would be required to determine the proper growth conditions for these mixed crystals.

### 5.3 Molecular Engineering of Propionates

Experimentation to enhance the properties of the propionates by molecular engineering of the organic acid radical was begun.

#### 5.3.1 Modification of Propionates

Substantial potential exists for molecular engineering within the propionate family. This can be seen for several reasons. First, large upward shifts of the transition temperature are caused by hydrostatic pressure: + 19.8°C/kbar for DSP (Ref. 29) [c.f. 2.7°C/kbar for TGS]. Second, exceptionally large downward shifts in the transition temperature are caused by small amounts of acetic acid replacing the propionic acid: -6°C/1% acetic acid for DSP (Refs. 30,31) and -10°C/1% acetic acid for DLP (Ref. 31).

Insights into the origin of these major changes in properties comes from NMR studies (Refs. 31,32). These studies suggest that the phase transition in the propionates is related to the freezing out of a rotation within the propionic acid radical. The evidence offered by the NMR studies is reinforced by the hydrostatic and acetic acid dopant work. Under hydrostatic pressure the rotation within the propionate radical is impeded and the phase transition occurs at higher temperatures. With partial substitution of the smaller acetate radical for the propionate radical, the rotations within the propionate are less impeded and the phase transition occurs at lower temperatures.

### 5.3.2 Experimentation

To explore this possibility of tailoring major changes within the propionate family, a number of other organic acids similar to propionic acid were obtained. Figure 58 shows the molecular structure of some of these acids. Freezing out the molecular rotation about the carbon-carbon bond indicated on the propionic acid (Fig. 58a) is associated with the ferroelectric phase transitions in the propionates. Partial replacement of the propionic acid with acetic acid (Fig. 58b) has been shown to facilitate this rotation and require lower temperatures before the ferroelectric phase transition occurs. The pyruvic, L(+) lactic ethane-sulfonic and acrylic (Fig. 58c,d,e,f) acid radicals are:

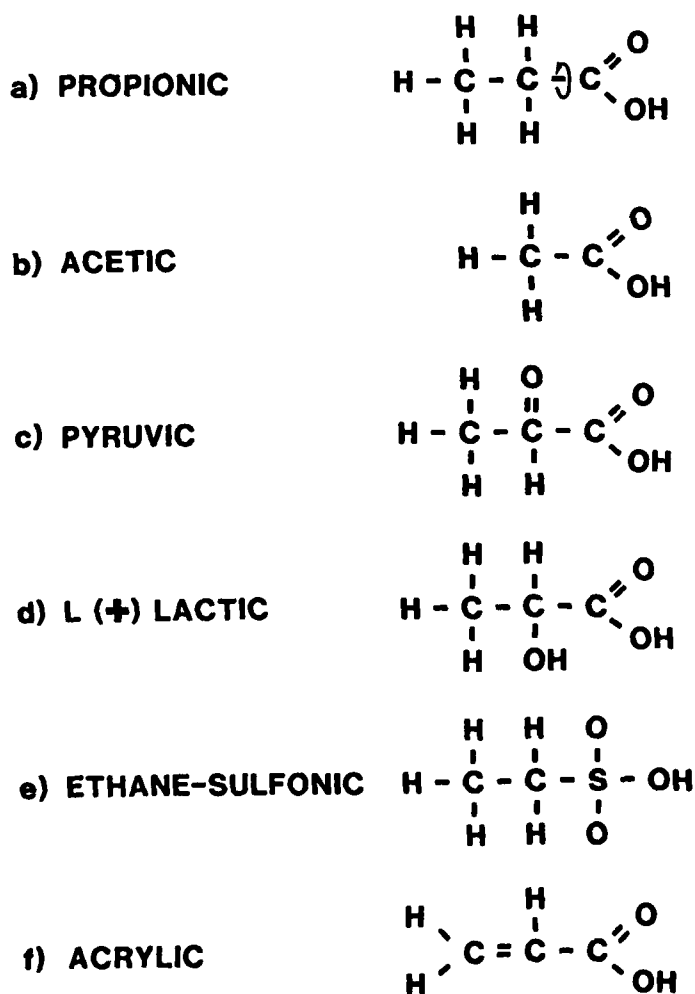


Figure 58. Molecular structure of acids.

clearly very similar to propionic acid; however, the differences all directly effect the rotational degree of freedom associated with the ferroelectric phase transition. Partial replacement of propionic acid by these acids should cause modifications in the properties of the propionate salts which show already excellent potential as pyroelectric transducer materials. Understanding the effect of such replacements should open up a substantial potential for engineering the pyroelectric properties to device requirements.

The results of partial substitution with various dopants are given in Table 13. Verification of doping levels was done using high resolution NMR spectroscopy (Ref. 30). From preliminary investigation of the quality of the crystals obtained by evaporation of solvent, it appeared that acrylic acid doped DLP yielded the largest, high quality crystals. Therefore, a large (2 liters of growth solution) scale experiment was initiated which produced two transparent crystals ~ 20 mm in height each of 10% acrylic acid doped DLP.

From these results it is concluded that there is an outstanding potential for substitution of various propionic acid-like species into the DLP or DSP network. Since the majority of this effort consisted only of preliminary investigations, it is clear that a larger scale program should yield a greater number of substitutional alternatives.

Table 13. Summary of Molecular Engineering.

<u>Substitution</u>	<u>Percent Dopant</u>	<u>Results</u>
Malonic Acid	20	Very small crystallites.
Pyruvic Acid	20	Polymer-like solid.
Ethane Sulfonic Acid	10	Very small yellowish crystals.
L(+) Lactic Acid	10	Very small crystals.
Acetic Acid	10	Good, well formed crystals.
Acrylic Acid	10	Very good, clear crystals.
Glycine	10	Poor crystals.
Oxalic Acid	10	Precipitation of calcium and strontium oxalate.
2-Chloropropionic Acid	100	Needles.
3-Chloropropionic Acid	100	Needle-like crystals.
3-Bromopropionic Acid	100	Conglomerate.
2-3 Dibromopropionic Acid	100	Conglomerate.
N-Butyric Acid	100	Conglomerate.
Glyceric Acid	100	Needles.
Perfluoropropionic Acid	100	Conglomerate.

6.        REFERENCES

1. H. Schmid, P. Chan, L.A. Petermann, F. Teufel and M. Maendly, *Ferroelectrics* 13, 351 (1976).
2. Philips Laboratories, "Optimized Pyroelectric Vidicon Thermal Imager, Vol. II: Improper Ferroelectric Materials", Final Report: Sept. 1976-Feb. 1978, W.A. Smith, NVEL/ USAECOM, Contract No. DAAG53-76-C-0053, Briarcliff Manor, NY, July 1978 (see Sec. 5.2).
3. G.M. Loiacono, M. Delfino, A. Shaulov, W.A. Smith and M.I. Bell, *Ferroelectrics*, In Press, (1980).
4. H. Schmid and H. Tippman, *Ferroelectrics* 20, 21 (1978).
5. H. Schmid and L.A. Petermann, *Phys. Stat. Sol(a)* 41, K147 (1977).
6. E. Ascher, H. Schmid and D. Tan, *Solid State Commun.* 2, 45 (1964).
7. R.W. Whatmore, C.J. Brierley and F.W. Ainger, *Ferroelectrics* 27, 67 (1980).
8. M. Takshige, H. Iwamura, S. Hirotsu and S. Sawada, *Ferroelectrics* 11, 431 (1976).
9. Philips Laboratories, "Optimized Pyroelectric Vidicon Thermal Imager, Vol. II: Improper Ferroelectric Materials", Final Report: Sept. 1976-Feb. 1978, W.A. Smith, NVEL/ USAECOM, Contract No. DAAG53-76-C-0053, Briarcliff Manor, NY, July 1978 (see Sec. 4.1).
10. N. Nakamura, H. Suga, H. Chihara and S. Seki, *Bull. Chem. Soc. Japan* 38, 1779 (1965).
11. Philips Laboratories, "Optimized Pyroelectric Vidicon Thermal Imager, Vol. II: Improper Ferroelectric Materials", Final Report: Sept. 1976-Feb. 1978, W.A. Smith, NVEL/ USAECOM, Contract No. DAAG53-76-C-0053, Briarcliff Manor, NY, July 1978. (see Pg. 128-129).
12. Philips Laboratories, "Optimized Pyroelectric Vidicon Thermal Imager, Vol. II: Improper Ferroelectric Materials", Final Report: Sept. 1976-Feb. 1978, W.A. Smith, NVEL/ USAECOM, Contract No. DAAG53-76-C-0053, Briarcliff Manor, NY, July 1978. (see Sec. 4.5).
13. K. Deguchi and E. Nakamura, *Phys. Rev. Lett.* 37, 1642 (1976).
14. E. Nakamura and M. Hosoya, *J. Phys. Soc. Japan* 23, 844 (1967).
15. B.T. Matthias and J.P. Remeika, *Phys. Rev.* 107, 1727 (1957).
16. A. Shaulov, M.I. Bell and W.A. Smith, *J. Appl. Phys.* 50, 4913 (1979).
17. H. Schmid, *J. Phys. Chem. Solids* 26, 973 (1965).
18. V.I. Bugakov, N.N. Sheftal and T.I. Timchenko, *Inorg. Mat.* 8, 1713 (1973).
19. T. Takahashi and O. Yamada, *J. Crystal Growth* 33, 361 (1976).

6. REFERENCES (Cont'd)

20. N. Nassan and J.W. Shiever, *J. Crystal Growth* 61, 59 (1972).
21. J.C. Joubert, J. Muller, M. Pernet and B. Ferrand, *Bull. Soc. Fr. Mineral Cristallogr.* 95, 68 (1972).
22. F.C. Kracek, G.W. Morey and H.E. Merwin, *Am. J. Sci.* 35A, 143 (1938).
23. G.C. Kennedy, *Am. J. Sci.* 248, 540 (1950).
24. V.I. Bugakov, N.N. Sheftal and T.I. Timchenko, *Isv. Ak. Nauk. SSSR, Neorgan. Material.* 8, 1947 (1972).
25. F.W. Ainger, R.W. Whatmore and C.J. Brierley-Plessey Research Company. (Private Communication).
26. D. Meschi, W. Chupka and J. Berkowitz, *J. Chem. Phys.* 33, 530 (1960).
27. R.W. Whatmore and F.W. Ainger (Private Communication).
28. Y. Nagae, Y. Ishibashi, Y. Takagi and H. Kameyama, *J. Phys. Soc. Japan* 41(4), 1300 (1976).
29. K. Gesi and K. Ozawa, *Japan J. Appl. Phys.* 12, 1287 (1978).
30. E. Nakamura, T. Nagai, S. Hashimoto and M. Hosoya, *J. Phys. Soc. Japan* 26, 979 (1969).
31. H. Shiraki, I. Tatsujaki and T. Yagi, *Phys. Stat. Sol. (a)* 7, 227 (1971).
32. E. Nakamura, K. Hikichi and J. Furuichi, *J. Phys. Soc. Japan* 23, 471 (1967).

APPENDIX A\*

DIELECTRIC ANOMALIES IN BORACITES

---

\* This appendix contains a discussion of the temperature dependence of the dielectric constant of FeI, CuCl and MnI boracite. These data are already contained in Section 2. What we present here is a unified discussion of the dielectric behavior as well as some theoretical insights gained from this unified perspective.

This manuscript is to be submitted for publication.

DIELECTRIC ANOMALIES IN BORACITES

Avner Shaulov and Wallace Arden Smith

Philips Laboratories  
Briarcliff Manor, N.Y. 10510

and

Hans Schmid

University of Geneva  
Geneva 4, Switzerland

ABSTRACT

Experimental results are reported on the dielectric behavior of  $\text{Fe}_3\text{B}_7\text{O}_{13}\text{I}$ ,  $\text{Ni}_3\text{B}_7\text{O}_{13}\text{Br}$ ,  $\text{Cu}_3\text{B}_7\text{O}_{13}\text{Cl}$ , and  $\text{Mn}_3\text{B}_7\text{O}_{13}\text{I}$ , near their cubic-orthorhombic phase transition.  $\text{Fe}_3\text{B}_7\text{O}_{13}\text{I}$  and  $\text{Ni}_3\text{B}_7\text{O}_{13}\text{Br}$  show the typical dielectric behavior of boracites, whereas  $\text{Cu}_3\text{B}_7\text{O}_{13}\text{Cl}$  and  $\text{Mn}_3\text{B}_7\text{O}_{13}\text{I}$  exhibit a different dielectric anomaly. Both types of behavior can be discussed on the basis of a Landau expansion of the thermodynamic potential.

## INTRODUCTION

Crystals of halogen boracites (general formula  $M_3B_7O_{13}X$ ,  $M$  = divalent metal,  $X$  = Cl, Br or I) possess peculiar dielectric behavior besides their unusual ferroelectric, magnetic, and structural properties.<sup>1</sup> Most boracites exhibit a first-order improper ferroelectric transition from a high temperature cubic phase  $T_d^5(F\bar{4}3c)$  to an orthorhombic phase  $C_{2v}^5(Pca2_1)$ . The special character of this phase transition becomes apparent through the unusual dielectric behavior around the transition. The temperature dependence of the dielectric constant,  $\epsilon$ , differs sharply from the usual Curie-Weiss dielectric anomaly in ordinary ferroelectric like  $BaTiO_3$  and TGS. Typically in boracites,  $\epsilon$ , increases slightly as the transition temperature is approached from above, and jumps abruptly downward at the transition to the ferroelectric phase. This behavior has been reported for all the boracites studied so far<sup>2-8</sup> with the exception of Cu-Cl boracite in which  $\epsilon$  jumps upward upon cooling through the transition from the paraelectric phase to ferroelectric phase.<sup>3</sup>

This paper reports the first measurements of the dielectric constant of a single domain Mn-I boracite. This material exhibits a similar behavior to that of Cu-Cl boracite, in that its dielectric constant jumps upwards on cooling

through the transition from the paraelectric to ferroelectric phase. As a supplement to the data reported in the literature, we also present experimental results on the dielectric behavior of Cu-Cl, Fe-I, and Ni-Br boracites. The two types of dielectric behavior, represented by Mn-I and Cu-Cl boracite on the one hand and Fe-I and Ni-Br boracite on the other hand, can be discussed on the basis of a Landau expansion of the thermodynamic potential.

#### EXPERIMENTAL TECHNIQUE

The samples were (100)<sub>cub</sub> cut single crystal wafers; the sources and other pertinent data on the samples are listed in Table I. Poling of the samples was undertaken by cooling the sample through the phase transition while applying a dc electric field of the appropriate magnitude as shown in Table I. In Cu-Cl and Mn-I boracite the poling and the measurements were performed under optical control of the domain state of the samples. These samples were electroded with transparent gold and mounted freely in a heating stage of a Leitz polarizing microscope. The single domain state of the Cu-Cl and Mn-I samples was controlled throughout the entire temperature range of the measurements, by continuous observation of the birefringence.

Pyroelectric measurements were used to assess the state of poling of the Fe-I and Ni-Br samples. The Fe-I sample reversed its polarization readily under the application

of a dc field of 10 kV/cm. Such behavior is indicative of a properly poled sample, however, it does not preclude the possibility that a multidomain structure exists which cannot be removed by application of an electric field as large as 10 kV/cm. Similar poling of the Ni-Br sample in the opposite direction resulted in a pyroelectric current whose magnitude differed from the initial measurement. This indicates a partial poling of this sample.

Two methods were used in the measurement of the dielectric constant. In the first method the electrical capacitance of the sample was measured directly, with accuracy better than 1%, using a Hewlett-Packard 4274 LCR meter. In the second method, we measured the ratio of the capacitance of the sample to that of a reference capacitor placed in series with it. A small ac signal was applied to the sample and reference and a lock-in amplifier (Ortholock-SC9505) was used to measure the in-phase voltage appearing across the reference capacitor. Both methods yielded similar results.

#### EXPERIMENTAL RESULTS

Figure 1 shows the temperature dependence of dielectric constant of Fe-I and Ni-Br boracite, as measured in a field of  $\sim 7$  V/cm at 8kHz using the reference capacitor technique.

Both materials exhibit the typical dielectric anomaly of boracites, i.e. the dielectric constant jumps upward in the transition to the paraelectric phase. Our data for Fe-I boracite are in good agreement with the previously reported measurement.<sup>7</sup> However, with Ni-Br boracite, our data give a distinctly different picture than is contained in the two previous reports in the literature.<sup>2,10</sup> We see a very large, sharp jump in  $\epsilon$  at the transition.

Essentially the same abrupt jump was seen in some preliminary measurements made on another sample of NiBr boracite supplied by Plessey. These measurements were made at 1 MHz using a Boonton 72B capacitance meter with a test field of 400 V/cm and an external bias of 20 kV/cm.\*

Measurement of  $\epsilon$  in Cu-Cl boracite was made in a field of 2.5 V/cm at 100 kHz using the HP LCR meter. The results are shown in Figure 2. Upon heating  $\epsilon$  increases from a value of 11.5 at room temperature to a peak value of 23 at the transition temperature. In the transition to the paraelectric phase,  $\epsilon$  jumps abruptly downward to a value of 14.5 and remains essentially constant up to 130°C. These results are in general agreement with the data at 10 kHz reported by Schmid and Pétermann.<sup>9</sup> However, their results show a slightly higher peak of  $\epsilon$  at the transition and a significant temperature dependence of  $\epsilon$  above the transition.

---

\* These preliminary measurements were performed by Dr. Joseph P. Dougherty.

These differences could be artifacts connected with the high dielectric loss (order of 10-100%) of the material at elevated temperatures. We made measurements at higher frequency to reduce the effect of the dielectric loss.

As was pointed out by Schmid and Pétermann<sup>9</sup> the dielectric behavior of Cu-Cl boracite is unusual. In most boracites (including Cu-Br<sup>8</sup>)  $\epsilon$  exhibits an abrupt jump upward at the transition to the paraelectric phase.<sup>2-8</sup>

A second example of the unusual behavior of Cu-Cl boracite is found in our measurements on Mn-I boracite (Figure 2). The dielectric constant of Mn-I boracite was measured in a field of 27 V/cm at 10 kHz using the HP LCR meter. Upon heating,  $\epsilon$  rises from a value of 11 at room temperature to a peak value of 27 at 134°C. In contrast to Fe-I and similarly to Cu-Cl boracite, the dielectric constant of Mn-I boracite jumps abruptly downward in the transition to the paraelectric phase. The dielectric loss was less than 1.2% over the entire temperature range of this measurement.

## DISCUSSION

The cubic-orthorhombic phase transition in boracites has been theoretically analyzed by several authors.<sup>11-13</sup> The present work discusses the experimental data on the

basis of a thermodynamic model proposed by Dvorak and Petzelt<sup>11</sup> and Gufan and Sakhnenko.<sup>12</sup> In their analysis, the cubic-orthorhombic phase transition in boracites is caused by a primary structural phase transition which doubles the volume of the unit cell, while the polarization arises as a secondary effect driven by this primary distortion. The known space groups of both the paraelectric and ferroelectric phases, uniquely determine the form of the thermodynamic potential required to describe this phase transition. Describing the magnitude of the primary structural distortion by the order parameter  $\eta$  and the polarization by  $P$ , a simplified form of this potential is

$$F = F(T)_0 + \frac{1}{2}\alpha(T-T_0)\eta^2 + \frac{1}{4}\beta\eta^4 + \frac{1}{6}\gamma\eta^6 + \frac{1}{2}\chi_0^{-1}P^2 + a_1\eta^2P + a_2\eta^2P^2 - EP, \quad (1)$$

where  $T$  and  $E$  are the temperature and electric field, and  $\alpha$ ,  $\beta$ ,  $\gamma$ ,  $\chi_0$ ,  $a_1$ , and  $a_2$  are assumed to be independent of temperature. It is significant to note that an interaction term in this thermodynamic potential must be included beyond the lowest order term allowed by symmetry. This term with the coefficient  $a_2$  is required to describe the dielectric behavior in boracites. <sup>11,12</sup>

To determine the temperature dependences  $P(T)$  and  $\eta(T)$ , we must find the minimum of the thermodynamic potential

with  $E=0$  as a function of temperature. The equilibrium conditions  $\partial F/\partial P = 0$ , and  $\partial F/\partial \eta = 0$ , yield for the spontaneous polarization  $P(T)$  and the inverse dielectric susceptibility  $\chi(T)^{-1}$  in the ferroelectric phase,

$$P = -a_1 \chi_0 \eta^2 / (1 + 2a_2 \chi_0 \eta^2) \quad (2)$$

$$\chi^{-1} = \chi_0^{-1} + 2a_2 \eta^2 - 2a_1^2 / [(\beta + 2\gamma \eta^2)(1 + 2a_2 \chi_0 \eta^2)^2] \quad (3)$$

where  $\eta(T)$  is determined by the equation:

$$\alpha(T - T_0) + \beta \eta^2 + \gamma \eta^4 - 2a_1^2 \chi_0 \eta^2 / (1 + 2a_2 \chi_0 \eta^2) + 2a_2 a_1^2 \chi_0^2 \eta^4 / (1 + 2a_2 \chi_0 \eta^2)^2 = 0 \quad (4)$$

In the paraelectric phase,  $P = 0$ ,  $\eta = 0$  and  $\chi = \chi_0$  is temperature independent. A general solution for  $\eta(T)$  requires detailed numerical computations, and a careful least squares fitting of the measurements to determine the six\* degrees of freedom in the thermodynamic potential. This work is still in progress. A good deal of insight, however, can be obtained from a preliminary discussion based on general considerations and reasonable approximations.

---

\* Since no experimental result depends on the absolute scale of  $\eta$ , we are free to fix this scale by fixing any one of the parameters arbitrarily (say  $\gamma = 1$ ). Conversely, no electrical measurements will suffice to determine the absolute scale of  $\eta$ .

From the stability condition  $\partial^2 F / \partial \eta^2 > 0$  it follows that  $(\beta + 2\gamma\eta^2) > 0$ , therefore, the last term on the right hand side of Eq. (3) can only account for a decrease of  $\chi$  in the transition to the paraelectric phase. However, when  $a_2 < 0$  the term  $2a_2\eta^2$  may lead to a reduction of this decrease or even to an increase of  $\chi$  in that transition. Hence, the magnitude and the sign of the jump of  $\chi$  at the transition is determined by the relative magnitudes of the two last terms in Eq. (3). As the transition is close to the second order type, the contribution of the third term on the right-hand side of Eq. (3) becomes more significant and the contribution of the second term becomes less significant. In this case a decrease of  $\chi$  in the transition to the paraelectric phase can be expected.

Various experiments show that the ferroelectric transition in Cu-Cl boracite is close to being of the second order type, whereas the analogous transition of most other boracites is strongly first order.<sup>14-16</sup> Our pyroelectric measurements indicate that the phase transition in Mn-I boracite is similar to that of Cu-Cl boracite. Thus the special character of the phase transition in Cu-Cl and Mn-I boracite can account for their unusual dielectric anomaly.

A quantitative discussion becomes simple for the case where the term  $2a_2\eta^2$  in Eq. (3) makes the principal contribution to the behavior of  $\chi^{-1}$ . This approximation was found

appropriate for MgCl boracite<sup>17</sup> and CoI boracite.<sup>18</sup> Assuming for  $\eta$  a temperature dependence which is typical for an order parameter in a first order transition:<sup>11</sup>

$$\eta^2 = \frac{2}{3}\Delta\eta^2 \left[ 1 + \left( \frac{T_1 - T}{T_1 - T_0} \right)^{\frac{1}{2}} \right], \quad (5)$$

the dielectric stiffness becomes

$$\chi^{-1} = \chi_0^{-1} + \frac{2}{3}\Delta\chi^{-1} \left[ 1 + \left( \frac{T_1 - T}{T_1 - T_0} \right)^{\frac{1}{2}} \right], \quad (6)$$

where  $\Delta\eta$  and  $\Delta\chi^{-1}$  are respectively the jumps of  $\eta$  and  $\chi^{-1}$  in the transition to the paraelectric phase, and  $T_1 = (4T_c - T_0)/3$ . This approximation seems to be very suitable for Ni-Br boracite where  $\epsilon$  exhibits a very noticeable jump upward in the transition to the paraelectric phase. A fitting of the experimental data on Ni-Br boracite to the theoretical prediction is shown in Figure 3. The crosses in Figure 3 represent the measured inverse dielectric susceptibility and the solid line is a fit to Eq. (6) using the parameters given in Table II. It is seen that a good agreement exists over a wide temperature range below the transition point. However, above the transition the theory predicts a constant value of  $\chi^{-1}$  while experimentally  $\chi^{-1}$  slightly increases with temperature.

In the approximation made in Eq. (6), the spontaneous polarization (Eq.(2)) can be related to the dielectric susceptibility:

$$P = (\Delta P / \Delta \chi) (\chi - \chi_0) , \quad (7)$$

where  $\Delta P$  and  $\Delta \chi$  are respectively the jumps of  $P$  and  $\chi$  in the transition to the paraelectric phase. Thus a knowledge of the temperature dependence of  $\chi$  enables one to characterize the behavior of the order parameter and spontaneous polarization. The calculated behavior of  $\eta^2$  and  $P$  in Ni-Br boracite is shown in Figure 4. The weak temperature dependence of the spontaneous polarization is typical of many boracites and it is experimentally observed as a mild increase of the pyroelectric coefficient as the transition point is approached.

The data on Fe-I boracite can be discussed in a fashion parallel to Ni-Br. It is apparent that the downward jumps observed in Cu-Cl and Mn-I boracite can be successfully encompassed within the more general case where the third term in Eq. (3) is not negligible. Such a discussion involves more degrees of freedom in the theory than can be determined from the dielectric data alone.

It is important to note that while the thermodynamic model of Dvorak and Petzelt and Gufan and Sakhnenko is capable of describing both types of dielectric anomalies observed in boracites, it does not explain the observed temperature dependence of the dielectric constant in the high temperature phase.

The model of Levanyuk and Sannikov is also able to subsume both upward and downward jumps in the dielectric constant.<sup>19</sup> This model does, in addition, predict a temperature dependence of the dielectric constant in the high temperature phase. Fits of our data to the expressions appropriate to the Levanyuk-Sannikov model suffer from the same problem of more degrees of freedom in the theory than can be determined by dielectric measurements alone.

It is interesting to reflect on how the difference in the dielectric behavior of Cu-Cl and Mn-I boracites might correlate with other properties of these materials and with the crystal chemistry of these compounds.

ACKNOWLEDGEMENT

The authors are grateful to T. Gier for samples of Fe-I boracite, and to F. W. Ainger and R. W. Whatmore for samples of Ni-Br boracite. We are also indebted to G. M. Loiacono for useful discussions, to J. P. Dougherty, who participated in the preliminary stages of this work at Philips Laboratories, and to J. Hannes for his help in measurements.

This work was supported by the Defense Advanced Research Projects Agency, and monitored by the U.S. Army Night Vision and Electro-Optics Laboratories, Fort Belvoir, Virginia.

## REFERENCES

1. R.J. Nelmes, J. Phys. C: Solid State Phys. 7, 3840 (1974).
2. E. Ascher, H. Schmid, and D. Tar, Solid State Commun. 2, 45 (1964).
3. F. Smutny and J. Fousek, Phys. Stat. Sol. 40, K13 (1970).
4. B.G. Bochkov, N.I. Bugakov, N.D. Gavrilova, V.A. Koptsik, and V.K. Novik, Sov. Phys. Crystallogr. 17, 1093 (1973).
5. B.G. Bochkov and S.N. Drozhdin, Sov. Phys. Crystallogr. 19, 811 (1975).
6. J. Albers, R.W. Sailer, and H.E. Müser, Phys. Stat. Sol.(a) 36, 189 (1976).
7. H. Schmid, P. Chan, L.A. Pétermann, F. Teufel, and M. Mändly, Ferroelectrics 13, 351 (1976).
8. P. Genequand, H. Schmid, G. Pouilly, and H. Tippmann, J. Physique 39, 287 (1978).
9. H. Schmid and L.A. Pétermann, Phys. Stat. Sol.(a) 41, K147 (1977).
10. R.W. Whatmore, C.J. Brierley, and F.W. Ainger, Ferroelectrics 27, 67 (1980).
11. V. Dvorák and J. Petzelt, Czech. J. Phys B21, 1141 (1971); V. Dvorák, Phys. Stat. Sol.(b), 55, K59 (1973); V. Dvorák, Ferroelectrics 7, 1 (1974).
12. Y.M. Gufan and V.P. Sakhnenko, Sov. Phys. Sol. State 14, 1660 (1973).
13. A.P. Levanyuk and D.G. Sannikov, Sov. Phys. Solid State 17, 327 (1975).

14. H. Schmid and H. Tippmann, *Ferroelectrics*, 20, 21 (1973).
15. D.J. Lockwood and R.W.G. Syme, *Ferroelectrics* 21, 557 (1978).
16. P. Felix, M. Lambert, R. Comes, and H. Schmid, *Ferroelectrics* 7, 131 (1974).
17. B.G. Bochkov, N.D. Gavrilova, V.K. Novik, and V.A. Koptsik, *Sov. Phys. Crystallogr.* 20, 404 (1975).
18. F. Smutny and C. Konák, *Phys. Stat. Sol.(a)* 31, 151 (1975).
19. D.G. Sannikov, *Pisma Zh. Eksp. Teor. Fiz.* 31, 342 (1980); *JETP Letters* 34, in press (1980).

#### FIGURE CAPTIONS

1. Dielectric constant of Fe-I and Ni-Br boracite measured in a field of 7 V/cm at 8 kHz.
2. Dielectric constant of Cu-Cl boracite (2.5 V/cm at 100 kHz) and Mn-I boracite (27 V/cm at 10 kHz) vs. temperature.
3. Temperature dependence of the inverse dielectric susceptibility of Ni-Br boracite. Crosses are experimental values; the solid line is a fit to Eq. (6) using the parameters given in Table II.
4. Calculated temperature dependence of the square of the order parameter and of the spontaneous polarization in Ni-Br boracite.

Table I. Data on the Samples Used in the Measurements.

	$\text{Fe}_3\text{B}_7\text{O}_{13}\text{I}$	$\text{Ni}_3\text{B}_7\text{O}_{13}\text{Br}$	$\text{Cu}_3\text{B}_7\text{O}_{13}\text{Cl}$	$\text{Mn}_3\text{B}_7\text{O}_{13}\text{I}$
Source	Dupont	Plessey	Schmid	Schmid
Area ( $\text{cm}^2$ )	0.016	0.017	0.04	0.022
Thickness ( $\mu\text{m}$ )	150	240	60	55
Electrodes	Evaporated Antimony	Silver Paint	Evaporated gold on chromium	Evaporated gold on chromium
Poling Field ( $\text{kV/cm}$ )	10	10	20	2-4
Domain State	Unknown likely single domain	Unknown likely polydomain	Single domain	Single domain

Table II. Parameters Used in Calculating the Inverse Dielectric Susceptibility of NiBr Boracite.

$T_c$ ( $^\circ\text{C}$ )	$T_1$ ( $^\circ\text{C}$ )	$T_0$ ( $^\circ\text{C}$ )	$\chi_0^{-1}$	$\Delta\chi^{-1}$
123.5	134.0	92.0	0.042	0.0496

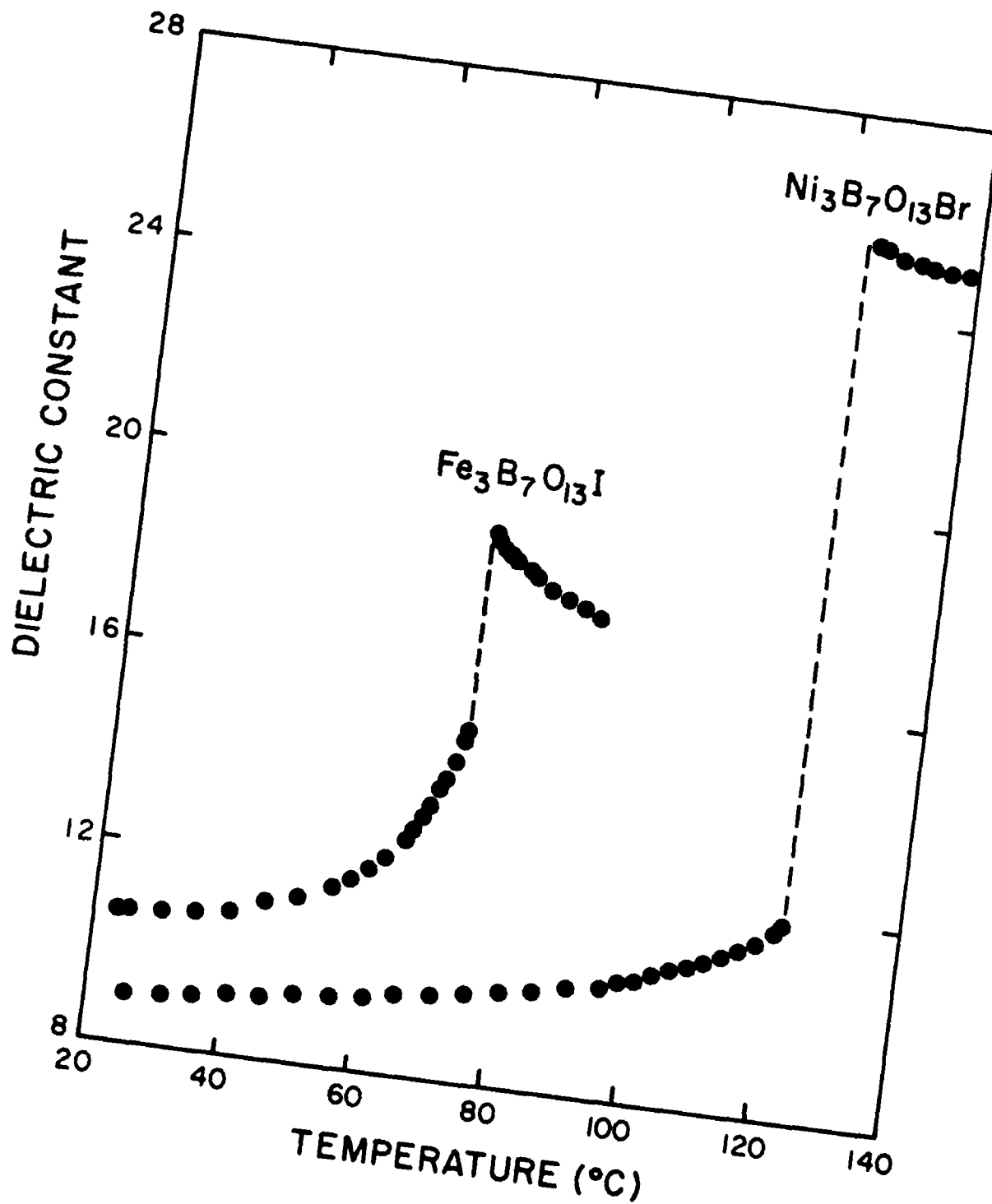


Figure 1

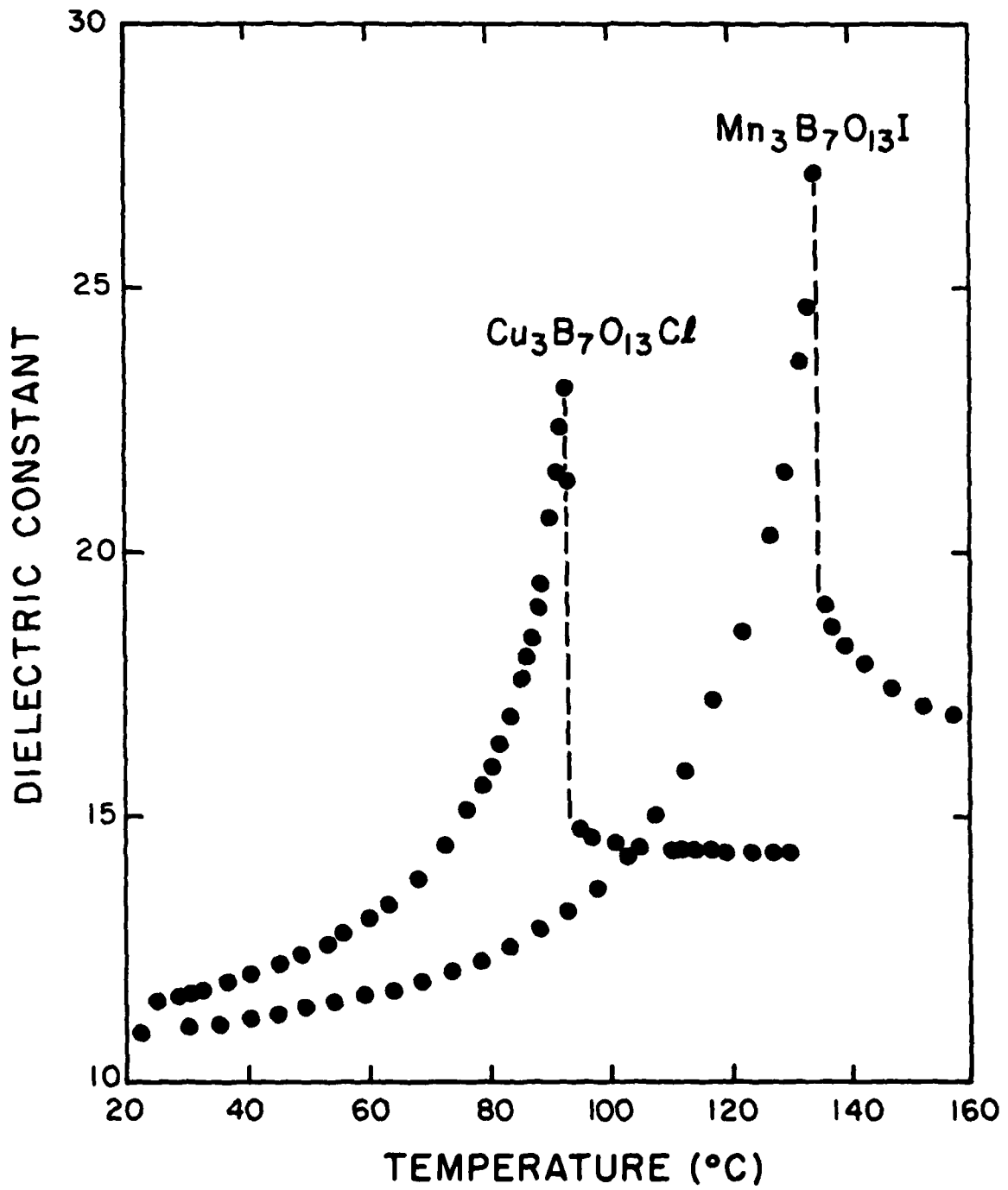


Figure 2

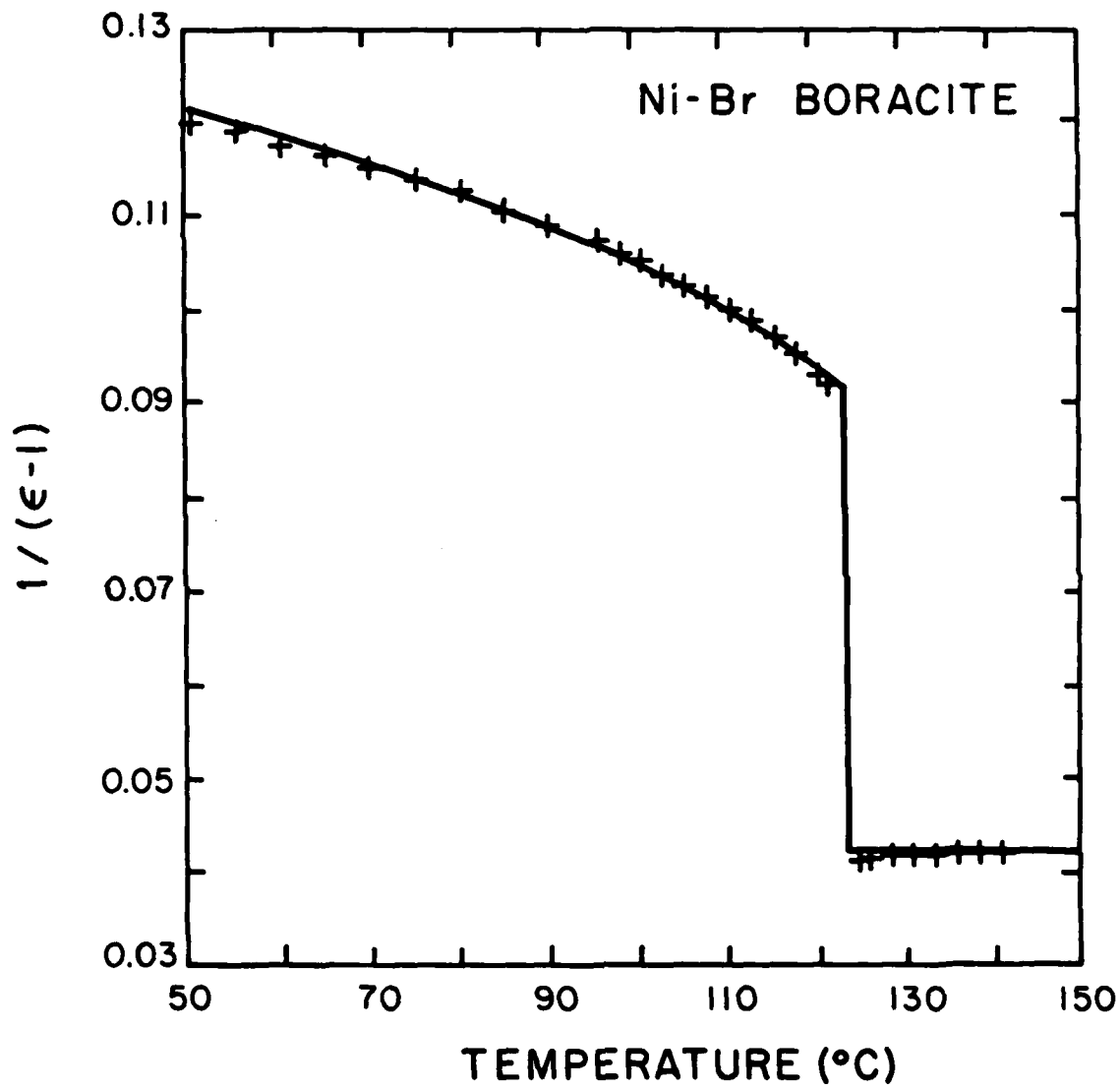


Figure 3

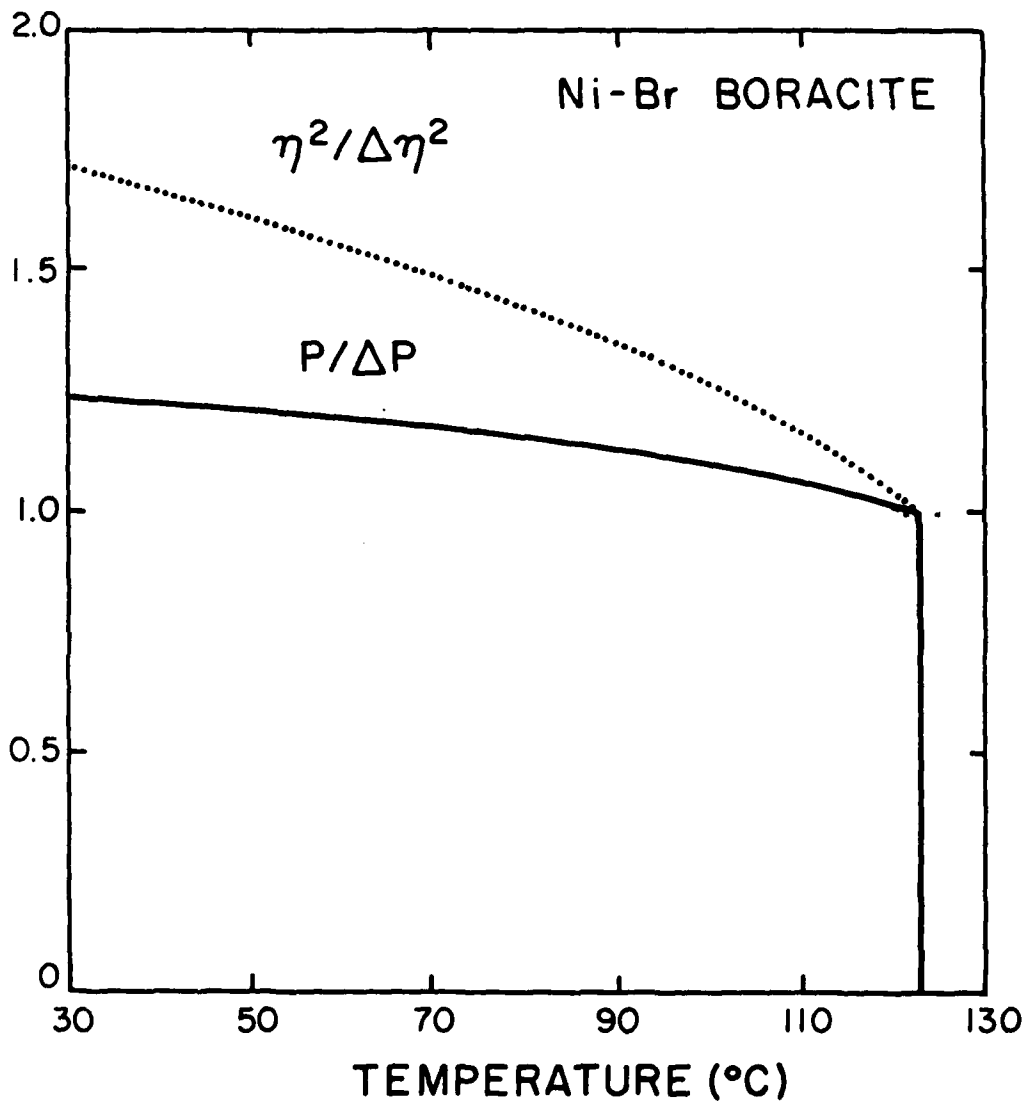


Figure 4

APPENDIX B

PROPIONATE X-RAY STRUCTURES

APPENDIX B

## Propionate X-Ray Structures

During the course of this research program it came to fore that Dr. A. M. Glazer at Oxford University had undertaken a study of the structural phase transistions in the propionates. Dr. Glazer had kindly given us the results of this research prior to publication. In addition, Dr. Glazer has participated in stimulating discussions of his X-ray structures and contributed useful insights on how the properties of the propionates can be tuned by various types of molecular modifications.

Dr. Glazer's study of the propionates began with his X-ray structure of dicalcium barium propionate (DBP). While this material is not ferroelectric at atmospheric pressure, it does provide many insights into the properties of its ferroelectric siblings - the lead (DLP) and strontium (DSP) salts that we have studied. The room-temperature, atmospheric pressure phase of DBP has the highest symmetry in the propionate family. As such, it is the appropriate place to begin a structural study since one could then describe the other phases as some distortion of the DBP structure.

The results of the DBP study are as follows:

THE CRYSTAL STRUCTURE AND DISORDER IN DICALCIUM  
BARIUM PROPIONATE

K. Stadnicka and A.M. Glazer

ABSTRACT

The room-temperature crystal structure of dicalcium barium propionate ( $\text{Ca}_2\text{Ba}(\text{C}_2\text{H}_5\text{COO})_6$ ) is described. It is cubic with  $a = 18.178(1) \text{ \AA}$  and space group  $\text{Fd}\bar{3}\text{m} (\text{O}_h)$ . The propionate molecules are found to be disordered between two sites. It is suggested that there are large-amplitude oscillations of the molecules about pseudo-2-fold axes with occasional flipping of the methyl carbons from one site to the other. Diffuse scattering studies indicate correlations along  $\langle 110 \rangle$  along  $\langle 001 \rangle$ . These are explained by an examination of the intermolecular contracts of the methyl carbon atoms, which shows that it is impossible to construct a fully three-dimensionally ordered structure.

The second step in Dr. Glazer's research was an X-ray study of DLP. This work is not as yet complete but preliminary results were communicated to us verbally.

In rough outline, the structure of the propionates consists of barium (lead or strontium) ions forming a diamond lattice with calcium ions sitting at the inversion points of the middle of the line joining adjacent barium (lead or strontium) ions. The carboxyl group (COO) from the propionate radical ( $\text{CH}_3\text{CH}_2\text{COO}$ ) forms O-C-O bridges between pairs of calcium ions. The resultant metal-oxygen framework has the spatially open structure of the diamond lattice. The long tails ( $\text{CH}_3\text{CH}_2$ ) of the propionate radical are joined to the carboxyl carbon (COO) and stick out into the empty space surrounding the metal-oxygen framework. There is only barely enough space to accommodate these organic radicals - indeed if they were oriented in the most symmetrical fashion they would bump into each other. This lack of space causes correlations to develop amongst the various adjacent organic radicals. In the high symmetry phase of the propionates, these correlations are either spatially or temporally disordered; on macroscopic time and space scales these correlations are averaged out. However, as the temperature is lowered or the pressure is increased, these correlations become stronger until finally they precipitate the formation of a new phase with greater spatial organization (i.e., the lower symmetry ferroelectric phase). This restructuring of the organic acid radicals is communicated to the metal-oxygen framework and also results in small displacements of those ions in the new low symmetry phase. By altering - via partial substitutions of other organic acid radicals - the interaction amongst the organic radical, one can then have a direct insight into the ferroelectric phase transition in these materials.

In addition to this understanding of the role of the organic radicals, Dr. Glazer's work shows that there is very strong segregation of the metallic ions, i.e., very few calcium ions appear on the barium (strontium or lead) sites and vice versa even though the metallic ions are chemically quite similar. This would suggest that an additional insight into the propionates can be obtained by substitution for the metal ions.

In conclusion, the picture drawn by these two X-ray studies provides direct confirmation of our working hypothesis that freezing out of disordered motions of the propionic acid radical is directly connected to the origin of ferroelectricity in the propionates. Moreover, these structural studies provide heuristic insights into specific directions to take in modifying the properties of the propionates by substitutions of the organic radicals and metal ions.

PRECEDING PAGE BLANK-NOT FILMED

APPENDIX C

CHEMICAL NOMENCLATURE

<u>Full Name</u>	<u>Chemical Formula</u>	<u>Acronym or Common Name</u>
<u>BORACITES</u>		
Nickel Bromine Boracite	$Ni_3B_7O_{13}Br$	NiBr boracite, NiBr
Iron Iodine Boracite	$Fe_3B_7O_{13}I$	FeI boracite, FeI
Copper Chlorine Boracite	$Cu_3B_7O_{13}Cl$	CuCl boracite, CuCl
Manganese Iodine Boracite	$Mn_3B_7O_{13}I$	MnI boracite, MnI
<u>(General Scheme):</u>		
Metal Halogen Boracite	$M_3B_7O_{13}X$	MX boracite, MX
<u>PROPIONATES</u>		
Dicalcium Lead Propionate	$Ca_2Pb(C_2H_5COO)_6$	DLP
Dicalcium Strontium Propionate	$Ca_2Sr(C_2H_5COO)_6$	DSP
Dicalcium Lead-Strontium Propionate	$Ca_2PbSr_{1-x}(C_2H_5COO)_6$	DLSP, Mixed Crystals
Dicalcium Barium Propionate	$Ca_2Ba(C_2H_5COO)_6$	DBP
<u>(Organic Acids Used):</u>		
Propionic	$C_2H_5COOH$	
Acetic	$CH_3COOH$	
Acrylic	$C_2H_3COOH$	
Ethane-Sulfone	$C_2H_5SO_2OH$	
Formic	$HCOOH$	
L(+) Lactic	$CH_3CHOHCOOH$	
Molonic	$CH_2(COOH)_2$	
Pyruvic	$CH_3COCOOH$	

Alphabetical Listing of Acronyms and Common Names

CuCl, CuCl boracite: Copper Chlorine Boracite,  $\text{Cu}_3\text{B}_7\text{O}_{13}\text{Cl}$

DBP: Dicalcium Barium Propionate,  $\text{Ca}_2\text{Ba}(\text{C}_2\text{H}_5\text{COO})_6$

DLP: Dicalcium Lead Propionate,  $\text{Ca}_2\text{Pb}(\text{C}_2\text{H}_5\text{COO})_6$

DLSP: Dicalcium Lead-Strontium Propionate,  $\text{Ca}_2\text{PbSr}_x(\text{C}_2\text{H}_5\text{COO})_6$ ,  $0 < x < 1$

DSP: Dicalcium Strontium Propionate,  $\text{Ca}_2\text{Sr}(\text{C}_2\text{H}_5\text{COO})_6$

FeI, FeI boracite: Iron Iodine Boracite,  $\text{Fe}_3\text{B}_7\text{O}_{13}\text{I}$

Mixed crystals: Dicalcium Lead-Strontium Propionate,  $\text{Ca}_2\text{PbSr}_{1-x}(\text{C}_2\text{H}_5\text{COO})_6$ ,  $0 < x < 1$

MnI, MnI boracite: Manganese Iodine Boracite,  $\text{Mn}_3\text{B}_7\text{O}_{13}\text{I}$

NiBr, NiBr boracite: Nickel Bromine Boracite,  $\text{Ni}_3\text{B}_7\text{O}_{13}\text{Br}$

DISTRIBUTION LIST

1. Texas Instruments  
13500 N. Central Expressway  
Dallas, Texas 75222
2. Honeywell, Inc.  
Corporate Research Center  
Hopkins, Minnesota 55343
3. Barnes Engineering  
30 Commerce Road  
Stamford, Conn. 06902  
ATTN: R. Astheimer
4. R.C.A.  
Government and Commercial  
Systems  
1901 N. Moore Street  
Arlington, VA 22209  
ATTN: D. Reid
5. Westinghouse Corporation  
Defense and Space Center  
P.O. Box 1521  
Baltimore, MD 21203
6. ITT  
Electron Tube Division  
3700 E. Pontiac Street  
Fort Wayne, Indiana 46803  
ATTN: E. Eberhart
7. General Electric Company  
777 Fourteenth Street, N.W.  
Washington, D.C. 20005  
ATTN: D. Hunter
8. Hughes Aircraft Company  
Industrial Products Division  
2020 Oceanside Blvd.  
Oceanside, CA 92054  
ATTN: J. Koda
9. Inrad Corporation  
406 Paulding Drive  
Northvale, New Jersey 07647  
ATTN: Dr. W. Roderman
10. Teltron Inc.  
Baltic Mews Industrial Park  
2 Riga Lane  
P.O. Box 416  
Douglassville, PA 19518  
ATTN: A. Mengel
11. Systems Research Laboratories  
Inc.  
2800 Indian Ripple Road  
Dayton, Ohio 45440  
ATTN: R. Holmes
12. Lockheed Missles & Space Inc.  
1111 Lockheed Way  
Sunnyvale, CA 94088
13. U.S. Naval Weapons Center  
China Lake, CA  
ATTN: W. Woodworth
14. Prof. Frank G. Ullman  
Dept. of Electrical Engineering  
University of Nebraska  
Lincoln, Nebraska 68588
15. Prof. Paul M. Raccah  
Univ. of Illinois at  
Chicago Circle  
P.O. Box 4348  
Chicago, Illinois 60680

END

DATE  
FILMED

1-5-81

DTIC